

Aus der  
Medizinischen Klinik und Poliklinik V  
Klinikum der Ludwig-Maximilians-Universität München  
und dem Comprehensive Pneumology Center Munich



## **Cellular immune regulation in skin wound healing**

Dissertation  
zum Erwerb des Doctor of Philosophy (Ph.D.)  
an der Medizinischen Fakultät der  
Ludwig-Maximilians-Universität München

vorgelegt von  
Ruoxuan Dai

aus  
Xinxiang, China

Jahr  
2023

---

Mit Genehmigung der Medizinischen Fakultät der  
Ludwig-Maximilians-Universität München

Erstes Gutachten: Prof. Dr. Jürgen Behr  
Zweites Gutachten: Dr. Yuval Rinkevich  
Drittes Gutachten: Prof. Dr. Markus Reinholz  
Viertes Gutachten: Prof. Dr. Rudolf A. Rupec

Dekan: Prof. Dr. med. Thomas Gudermann

Tag der mündlichen Prüfung: 07.12.2023

---

## Affidavit



**Dai, Ruoxuan**

\_\_\_\_\_  
Surname, first name

**Max-Lebsche-Platz 31**

\_\_\_\_\_  
Street

**81377, Munich, Germany**

\_\_\_\_\_  
Zip code, town, country

I hereby declare, that the submitted thesis entitled:

**Cellular immune regulation in skin wound healing**

.....

is my own work. I have only used the sources indicated and have not made unauthorised use of services of a third party. Where the work of others has been quoted or reproduced, the source is always given.

I further declare that the dissertation presented here has not been submitted in the same or similar form to any other institution for the purpose of obtaining an academic degree.

Munich, 15.04.2023

\_\_\_\_\_  
place, date

Ruoxuan Dai

\_\_\_\_\_  
Signature doctoral candidate

---

# Confirmation of congruency



**Confirmation of congruency between printed and electronic version of the doctoral thesis**

**Dai, Ruoxuan**

\_\_\_\_\_  
Surname, first name

**Max-Lebsche-Platz 31**

\_\_\_\_\_  
Street

**81377, Munich, Germany**

\_\_\_\_\_  
Zip code, town, country

I hereby declare, that the submitted thesis entitled:

**Cellular immune regulation in skin wound healing**

.....

is congruent with the printed version both in content and format.

Munich, 15.04.2023

\_\_\_\_\_  
place, date

Ruoxuan Dai

\_\_\_\_\_  
Signature doctoral candidate

---

## Table of content

<b>Affidavit .....</b>	<b>3</b>
<b>Confirmation of congruency .....</b>	<b>4</b>
<b>Table of content.....</b>	<b>5</b>
<b>List of abbreviations .....</b>	<b>6</b>
<b>List of publications .....</b>	<b>8</b>
<b>Publications .....</b>	<b>9</b>
1.1 Publication I.....	9
1.2 Publication II.....	10
<b>2. Introductory summary .....</b>	<b>11</b>
2.1 Physiological structure and function of the skin .....	11
2.2 The repair process of skin wound healing .....	11
2.2.1 Normal wound healing of the skin .....	11
2.2.2 Chronic wound healing of the skin .....	14
2.2.3 Excessive wound healing.....	15
2.3 Skin fibroblast subpopulations in mobilized skin fascial tissue promote wound healing.....	17
2.4 Migrating adipocytes cannot be converted to myofibroblasts in skin wound healing .....	19
<b>3. Paper I .....</b>	<b>21</b>
<b>4. Paper II .....</b>	<b>57</b>
<b>References .....</b>	<b>105</b>
<b>Acknowledgements.....</b>	<b>109</b>
<b>Curriculum vitae .....</b>	<b>110</b>

---

## List of abbreviations

ECM	Extracellular matrix
PDGF	Platelet derived growth factor
ROS	Reactive oxygen species
H <sub>2</sub> O <sub>2</sub>	Hydrogen peroxide
DAMPs	Damage associated molecular patterns
NETs	Neutrophil extracellular traps
IL	Interleukin
TNF	Tumor necrosis factor
VEGF	Vascular endothelial growth factor
EGF	Epidermal growth factor
IGF	Insulin-like growth factor
NGF	Nerve growth factor
FGF	Fibroblast growth factor
NO	Nitric oxide
SOD	Superoxide dismutase
TGF	Transforming growth factor
NLRP3	NLR family pyrin domain containing 3
MCP-1	Monocyte chemoattractant protein-1
PPAR- $\gamma$	Peroxisome proliferator activated receptor- $\gamma$
NETs	Neutrophils release extracellular traps
PAD4	Peptidyl deaminase 4
HTS	Hypertrophic scars
Treg cell	Regulatory T cell
MMP	Matrix metalloproteinases
MCS	Mesenchymal stem cell
En1	Engrailed-1
EPFs	En1-past fibroblasts
GFP	Green fluorescence protein
ENFs	En1-naïve fibroblasts
RFP	Red fluorescence protein
ePTFE	Polytetrafluoroethylene

---

PC	Panniculus carnosus
DT	Diphtheria toxin
YAP	Yes-associated protein
sh	Short hairpin
dWAT	Dermal white adipose tissue
sWAT	Subcutaneous white adipose tissue
Plin1	Perilipin-1

---

## List of publications

1. Rajendran V, Ramesh P, **Dai R**, Kalgudde Gopal S, Ye H, Machens HG, Adler H, Jiang D, Rinkevich Y. Therapeutic Silencing of p120 in Fascia Fibroblasts Ameliorates Tissue Repair. *J Invest Dermatol.* 2022 Nov 26:S0022-202X(22)02821-4. doi: 10.1016/j.jid.2022.10.018. Epub ahead of print. PMID: 36442618.
2. Shruthi Kalgudde Gopal\*, **Ruoxuan Dai\***, Ania Maria Stefanska, Meshal Ansari, Jiakuan Zhao, Pushkar Ramesh, Johannes W. Bagnoli, Donovan Correa-Gallegos, Yue Lin, Simon Christ, Ilias Angelidis, Valerio Lupperger, Carsten Marr, Lindsay C. Davies, Wolfgang Enard, Hans-Günther Machens, Herbert B. Schiller, Dongsheng Jiang, Yuval Rinkevich. Wound infiltrating adipocytes are not myofibroblasts. *Nature Communications*. **\*First author with equal contribution** (Accepted by editor)



---

## Publications

### 1.1 Publication I

Rajendran V, Ramesh P, **Dai R**, Kalgudde Gopal S, Ye H, Machens HG, Adler H, Jiang D, Rinkevich Y. Therapeutic Silencing of p120 in Fascia Fibroblasts Ameliorates Tissue Repair. *J Invest Dermatol.* 2022 Nov 26:S0022-202X(22)02821-4. doi: 10.1016/j.jid.2022.10.018. Epub ahead of print. PMID: 36442618.

Publisher's version is available online in: <https://pubmed.ncbi.nlm.nih.gov/36442618/>

In this work, my contributions include: a) Immunostaining of samples of viroous markers. b) Statistical analysis of different markers expression.

In particular:

- (1) Figure 2c, 2d: Immunostaining GFP<sup>+</sup> wound resident fibroblasts from 7dpw expressing myofibroblast marker( $\alpha$ SMA) and fibroblast markers (CD26; ERTR7)
- (2) Figure S1: Immunostaining of different cell type (epidermal marker CK14, endothelial marker CD31, immune cell marker CD45, pan fibroblast cell marker PDGFR, fascia fibroblast marker N-cadherin and Sca1) of AAV8-GFP transduced cells.
- (3) Figure S2: Immunostaining of p120 in *En1<sup>Cre</sup>;R26<sup>mTmG</sup>* mice and different cell markers (N-cadherin, CD45, Caspase-3) in AAV8 control shRNA and AAV8 p120 shRNA injected wounds.

---

## 1.2 Publication II

Shruthi Kalgudde Gopal\*, **Ruoxuan Dai\***, Ania Maria Stefanska, Meshal Ansari, Jiakuan Zhao, Pushkar Ramesh, Johannes W. Bagnoli, Donovan Correa-Gallegos, Yue Lin, Simon Christ, Ilias Angelidis, Valerio Lupperger, Carsten Marr, Lindsay C. Davies, Wolfgang Enard, Hans-Günther Machens, Herbert B. Schiller, Dongsheng Jiang, Yuval Rinkevich. Wound infiltrating adipocytes are not myofibroblasts. *Nature Communications*. **\*First author with equal contribution** (Accepted by editor)

**The above study is a result of my contribution as a “shared-first author” or “first-author-with equal contribution”.** My major contribution include a) Completed full-thickness excisional wounding experiments with *En1<sup>Cre</sup>;R26<sup>mTmG</sup>* mice and *Adipoq<sup>Cre</sup>;R26<sup>mTmG</sup>* mice at day 0, day 10 and day 21. b) Fascia tissue isolation and digestion for FACS sorting of adipocytes and fibroblasts with negative depletion strategy and live/dead staining, mRNA extraction, cDNA conversion and expansion and bead purification, quality control, sample delivery for bulk sequencing. c) Cryosections for the samples and various immunostainings of Perilipin,  $\alpha$ SMA, Vimentin, Cathelicidin of *En1<sup>Cre</sup>;R26<sup>mTmG</sup>* mice and *Adipoq<sup>Cre</sup>;R26<sup>mTmG</sup>* mice. d) Completed full-thickness excisional wounding experiments with *Procr<sup>CreER</sup>;Ai14* mice and *PDPN<sup>CreER</sup>;Ai14* mice at day 7. e) Immunostainings of Perilipin, PDGFR $\alpha$ , and ER-TR7 were performed with cryosections of healthy skin and day 7 wounds of *Procr<sup>CreER</sup>;Ai14* mice and *PDPN<sup>CreER</sup>;Ai14* mice. f) Modified and draw the flowchart. g) Revision of the manuscript and data statistical analysis.

In particular:

- (1) Figure 1a: Modified and draw the scheme.
- (2) Figure 5a, 5b, 5c, 5d, 5e, 5h: Implementation of in vivo experiment and immunostainings of adipocytes/fibroblasts markers to prove adipocytes are non fibrogenic in wounds.
- (3) Figure S5a, S5b, S5c: Heatmap analyze the core signature gene of FACS sorting GFP<sup>+</sup> cells and immunostainings of Ki67 in wounds.
- (4) Figure S6 (delete according to Reviewer 3): Implementation of in vivo experiment and immunostainings of adipocytes cell marker to proof adipocytes in adult wounds do not overlap with wound fibroblasts.

---

## **2. Introductory summary**

### **2.1 Physiological structure and function of the skin**

With a surface area of around 1.8 square meters, the human skin serves as the body's primary physical barrier and aids in defending the body against external diseases and environmental toxins [1]. The most outer epidermis layer, the inner dermis layer, and the deepest layer of subcutaneous or hypodermis tissue make up the three primary layers of normal human skin.

The epidermis, the skin's outermost layer, can be subdivided into five sublayers [2, 3]. Stratum corneum, stratum lucidum and stratum granulosum are the outermost layers of the epidermis of the skin, which is made up of dead cells that can shield the body from friction and moisture loss. Keratinocytes, which may create keratin and make up the fundamental structure of skin, are abundant in the stratum spinosum layer. The deepest layer of epidermis is stratum basale, it comprises constantly dividing basal cells that push older cells upwards. It also contains melanocytes, which control skin pigmentation.

The next inner dermis layer predominantly consists of extracellular matrix, blood vessels, lymphatics, nerves, sweat glands and pilosebaceous units. This layer is divided into two sublayers: the upper papillary and the lower reticular dermis layers. The papillary dermis layer has tiny collagen fibers that are tightly packed and is just 0.3 – 0.4 mm thick. The reticular dermis layer, in contrast, develops interwoven bundles of denser fibers [4].

The dermis and skeletal muscles are wedged between the subcutaneous or hypodermis tissue, the skin's deepest layer. Proteoglycans and glycosaminoglycans are particularly abundant in the hypodermis tissue, which draws fluid into the tissue and gives it mucous-like qualities [5]. Fibroblasts, adipose cells, and macrophages are the types of cells found in the hypodermis, and they play a specific function in adipocyte homeostasis in obesity, likely connected to tissue remodeling and could promote fat thermogenesis when exercising and being exposed to cold temperatures [6]. The hypodermis of pig and human skin was discovered that the structure was made up of a lattice network of fibrous tissue that was mostly vertically oriented and was structured into geometric forms. This loose connective tissue structure was later defined as fascia. Increasingly, its mechanisms and functions are being studied.

### **2.2 The repair process of skin wound healing**

Both the rate and the integrity of skin wound healing differ under various physiological circumstances. For instance, wounds can last a long period in diabetic and immunocompromised patients. After healing, the lesions in certain people with scarring sometimes develop into keloids. As a result, the following healing states will be used to explain how skin wounds heal.

#### **2.2.1 Normal wound healing of the skin**

Acute wounds are typically caused by tissue injuries that can usually heal completely within the expected timeframe of 8-12 weeks, with minimal scarring [7]. The normal acute wound healing sequence is: hemostasis, inflammation, proliferation and remodeling [8].

---

## 1. Hemostasis

The hemostatic process, the first line of defense against skin wounds, is triggered when the blood vessels of the skin are damaged. This results in the production of a quick hemagglutination response in the wound. This process involves vasoconstriction and platelet aggregation [9].

When an injury occurs, the body's response includes rapid vasoconstriction. This is achieved through a reflex contraction of the vascular smooth muscle, which is triggered by the release of vasoconstrictors like endothelin from injured endothelial cells. These vasoconstrictors cause the blood vessels to narrow, reducing blood flow to the injured area [10]. Additionally, platelets generate platelet-derived growth factor (PDGF), which has the ability to contract smooth muscle in the artery wall by activating it [11-13]. However, the first reflex contraction only stops bleeding for a brief period. Passive muscle relaxation is caused by increased acidity and hypoxia in the wound, which in turn promotes the recovery of bleeding. Following activation of the coagulation cascade requires long-term relief of bleeding issue as well as further regulation of vasoconstriction by mediators of bradykinin, fibrinopeptide, 5-hydroxytryptamine, and thromboxane A<sub>2</sub> [14, 15].

Primary hemostasis and secondary hemostasis occur simultaneously and are mechanistically interrelated [16]. Primary hemostasis involves platelet aggregation and the formation of platelet plug. Platelets bind to the matrix via G protein-coupled receptors on their surface and trigger an inside-out signaling cascade that activates integrins and enhances platelet adherence to the surrounding extracellular matrix (ECM) and other platelets to plug the injury [17]. When the coagulation cascade is activated, soluble fibrinogen is transformed into insoluble fibrin chains that form a fibrin network, reinforcing and solidifying the clot. This process is known as secondary hemostasis. Platelets serve a hemostatic role by adhering to the fibrin network to form a thrombus, and their release of complement and growth factors creates a temporary scaffold for invading cells that is essential for wound healing [18].

## 2. Inflammation

The inflammatory phase is characterized by a large number of immune cells infiltrating the wound, such as neutrophils, monocytes, and lymphocytes [19]. This phase of wound healing lasts 48 hours following injury [20]. Pro-inflammatory mediators are abundant at this stage, flooding the area around the wound and recruiting more immune cells from the blood vessels. During the inflammatory phase, phagocytes play a crucial role in removing necrotic material from the wound. The primary objective of this phase is to provide the host with sufficient time to protect itself from any infections that might penetrate the wound site.

Large numbers of chemokines, lipid mediators, hydrogen peroxide (H<sub>2</sub>O<sub>2</sub>), damage-associated molecular patterns (DAMPs) released by damaged cells, signaling the recruitment of inflammatory cells, particularly neutrophils. Neutrophils play a crucial role in fighting pathogens by deploying different mechanisms. Firstly, they release proteases from their intracellular granules to break down invading microbes. Additionally, neutrophils can generate neutrophil extracellular traps (NETs) through a process known as NETosis. During NETosis, neutrophils extrude chromatin filaments coated with proteases outside their cell membrane to ensnare and neutralize pathogens, effectively eliminating them from the host [21]. It was discovered that inhibiting the formation of NETs or removing NETs may improve wound healing [22]. Also, phagocytosis by neutrophils plays an important role in the early stages of wounding. Surface receptors and integrins on neutrophils help them recognize antigens. The antigen is then engulfed by a phagocytic cup formed

---

by the neutrophil granules, where proteases break it down [23]. Proteases are the main component of toxic particles. When active, proteases can digest surrounding tissue to let neutrophils exit the vasculature and reach the site of damage. Proteases are crucial for antibacterial action, for dissolving fibrillary ECM, and for breaking down basement membranes [24]. Clearing neutrophils in a timely manner is essential for resolving tissue inflammation. Neutrophils can either be phagocytosed by macrophages, or they can re-enter the vasculature in a distinct process and leave sites of tissue damage referred to as neutrophil reverse transendothelial migration.

Throughout the first 24 to 48 hours after a wound is formed, macrophages then gather at the site of the lesion [25]. The release of monocyte chemoattractant protein-1 (MCP-1) plays a crucial role in the recruitment of monocytes from the bone marrow to the site of inflammation, which promotes monocytes rapidly differentiate into macrophages and actively participate in the immune response. To combat wound infection, macrophages then produce copious amounts of pro-inflammatory cytokines including interleukin (IL)-6, tumor necrosis factor (TNF)- $\alpha$ , and IL-1 to activate fibroblasts [26]. Meanwhile, macrophages engulf pathogens and cellular debris through their phagocytosis. Phagocytosis of apoptotic neutrophils by macrophages signals the end of the inflammatory phase of wound healing [27].

### 3. Proliferation

During the proliferative phase of the wound (after approximately 3-10 days), the main goals of the wound healing process are to cover the wound surface, restore the vascular network, and form granulation tissue.

In the initial proliferation phase of wound healing, keratinocytes migrate upward from the injured dermis, which is defined as re-epithelialization. During this process, localized keratinocytes from the margins of the lesion and stem/progenitor cells from sweat glands or interfollicular epidermis progressing from the margins to the wound center [28-30]. The signaling pathways of epithelium and non-epithelial cells along the wound edge, which produce a wide range of cytokines and growth factors including epidermal growth factor (EGF), insulin-like growth factor (IGF)-1, and nerve growth factor (NGF), promote this process [31].

During the next proliferative phase, new blood vessels are formed, and capillaries sprout and link to fibroblasts and macrophages. Granulation tissue then works to remove the fibrin matrix, paving the way for the creation of a new matrix. This new matrix serves as a foundation on which keratinocytes can regenerate the damaged epidermis, restoring the skin's integrity [32]. Growth factors, including VEGF, PDGF, fibroblast growth factors (FGF), and serine protease thrombin, bind to receptors on existing vascular endothelial cells, thereby activating intracellular signaling cascades. Proteolytic enzymes are secreted by the activated endothelial cells, which lyse the basal lamina. Endothelial cells can proliferate and move into the wound as a result, then the freshly constructed endothelial sprouts create tiny tubular canals that join to one another to form a vessel loop [33].

The proliferative phase culminates in the formation of acute granulation tissue, which is characterized by a dense network of capillaries and loosely arranged collagen fibers. This process also involves the recruitment of numerous granulocytes, macrophages, and fibroblasts. Collagen and other ECM components (e.g., fibronectin, glycosaminoglycan, proteoglycan, and hyaluronic acid) can be produced by fibroblasts [4, 34]. The temporary wound matrix, on which the relevant cell migration and organization takes occur, is therefore created by fibroblasts. The number of mature fibroblasts is reduced by myofibroblast differentiation and terminated by subsequent apoptosis at the conclusion of this phase.

---

#### 4. Remodeling

Remodeling, which usually starts 2 to 3 weeks after damage and lasts for a year or longer, is the last stage of wound healing. All post-injury activation processes are gradually decreased and terminated during this period. The majority of endothelial, macrophage, and myofibroblast cells either suffer apoptosis (programmed cell death) or wither away from the wound, leaving a mass made of collagen and other extracellular matrix components and a few cells. In addition, the cell-free matrix undergoes an active remodeling process within 6–12 months, changing from a matrix with a largely type III collagen foundation to one with a predominantly type I collagen [35]. This form of collagen differs from the basket-like collagen present in healthy dermis as it is organized in short parallel bundles. And through their many collagen-attachments, myofibroblasts produce wound contraction and aid in reducing the surface of growing scars.

### 2.2.2 Chronic wound healing of the skin

Wounds that are challenging to cure and remain longer than 6 weeks or regularly reopen are known as chronic wounds [36]. The most prevalent chronic wound disease in the U.S. is diabetic ulcers [37]. With a mortality rate greater than most malignancies, more than half of patients who have limbs amputated due to ulcers will die within 5 years [38]. Peripheral neuropathy can cause patients to be unaware of small wounds, leading to undetected ulcer development and progression. Additionally, diabetes can damage the larger blood vessels in the legs, resulting in peripheral arterial disease and impaired circulation. This vascular issue can significantly impede ulcer healing. The long-lasting and recurring ulcers that result from diabetes place a substantial burden on the healthcare system [39].

#### 1. Platelets

A crucial element of hemostasis, platelets are in charge of some of the early reactions to damage. The thrombus can play a temporary scaffold role in facilitating the proliferation and migration of cells that are involved in the process of wound healing. However, for complete healing to occur, the thrombus must eventually be removed or broken down to allow for the regeneration of healthy tissue. It has been shown that under diabetes circumstances, platelets are less susceptible to the nitric oxide (NO) that the vascular endothelium releases, which ordinarily lessens vessel wall aggregation [40]. This is further worsened by poor insulin signaling, which causes the vascular endothelium to produce less NO and endothelial nitric oxide synthase and superoxide dismutase (SOD) to function less efficiently [41]. Consequently, as has been shown in diabetic patients, platelet dysfunction plays a role in the development of microvascular illness.

#### 2. Neutrophils

Neutrophils play a crucial role in the inflammatory stage of wound healing and are responsible for removing germs. Nevertheless, chronic, non-healing wounds are linked to ongoing neutrophil recruitment and activation. Increased neutrophil-derived protease levels (e.g. elastase and matrix metalloproteinases (MMP)-8 and -9) are hypothesized to have a role in chronic inflammation and delayed wound healing [42]. In addition to proteases, neutrophil release of extracellular traps (NETs) is increased in diabetes and affects the resolution of inflammation during wound healing [43]. It has been demonstrated that peptidyl deaminase 4 (PAD4), the protein that causes NETs, is higher in neutrophils from both diabetic mice and patients, making them more prone to NETosis and potentially causing persistent inflammation and tissue damage [22].

---

### 3. Monocyte/macrophages

Early in the inflammatory phase, monocytes are attracted to the wound site where they undergo differentiation into macrophages and dendritic cells. The establishment of the initial inflammatory phase and the promotion of the change from a pro-inflammatory to an anti-inflammatory environment depend critically on the infiltration of monocytes and macrophages [44, 45].

During the normal healing process, there is a shift from inflammatory to proliferative activities which is reflected by a change in the ratio of M1 to M2 macrophage phenotypes. To encourage pathogen-killing activity and early wound debridement, classically activated M1 macrophages release high quantities of pro-inflammatory cytokines (e.g. IL-1, IL-6, IL-12, TNF- $\alpha$ ) and oxidative metabolites (e.g. NO, superoxide) [46, 47]. Inflammation is induced and aids in its resolution when M2 macrophages are activated, especially through IL-4 and IL-13 signaling. IL-10, VEGF, transforming growth factor (TGF)- $\beta$ 1, and PDGF, which encourage the formation of granulation tissue, angiogenesis, and cell proliferation, are among the cytokines and growth factors secreted by classical M2 macrophages that are upregulated to indicate the phenotypic switch.

In diabetic wounds, macrophages remain in a persistent M1 inflammatory state, wherein macrophages promote the destruction of surrounding tissues directly or indirectly by recruiting other pro-inflammatory immune cells. Matrix metalloproteinase 1 (MMP1) and the pro-inflammatory cytokine TNF- $\alpha$  are both downregulated by M1 macrophages, which inhibits keratinocyte migration and slow wound healing [48]. Through the NLR Family Pyrin Domain Containing 3 (NLRP3) inflammasome and Peroxisome proliferator-activated receptor- $\gamma$  (PPAR- $\gamma$ ) signaling, excess glucose and adipose tissue increase the expression of inflammatory markers (e.g. TNF- $\alpha$ , IL-1, IL-6) and this also increases the expression of pro-inflammatory genes, which further activates M1 macrophage polarization [49-51]. This vicious cycle results in chronic inflammation and wounds that are unable to heal. Moreover, hyperglycemia causes an increase in histone acetylation and methylation, which supports the M1 macrophage phenotype.

### 4. Fibroblasts

Fibroblast function changes also lead to defective epithelialization and delayed wound healing in diabetics. These mainly involve decreased proliferation, increased apoptosis, and impaired migration to the wound site [52, 53]. In patients with diabetic foot ulcers (DFUs), specific populations of fibroblasts were found to be overexpressing *MMP1*, *MMP3*, *MMP11*, *HIF1A*, *CHI3L1*, and *TNFAIP6*, which helped in promoting the polarization of M1 macrophages. Furthermore, through spatial transcriptomic analysis of patients, it was found that fibroblasts associated with wound healing showed a preference towards the wound bed rather than the wound edge or healthy skin [38]. Hyperglycemia can impair cytokine signaling pathways that affect fibroblast differentiation (e.g. TGF- $\beta$  pathway), alter fibroblast apoptosis, dysregulate dermal lipolysis, and increase hypoxic injury. As a result, myofibroblast formation is impaired, the extracellular matrix is improperly regulated, and wound contractility is decreased [54].

## 2.2.3 Excessive wound healing

Excessive healing is characterized by the overproduction of extracellular matrix, increased local vascularity, and excessive cell proliferation. These changes may lead to the formation of hypertrophic scars or keloids, which can be unsightly and uncomfortable. This hypertrophic scarring may be due to a severe injury (e.g., burn) or may manifest after an acute injury in a keloid with a

---

genetic basis. Large disfiguring scars can physically deform surface structures (e.g., nose, eyelids) [55].

### 1. Macrophages

In keloid tissues, macrophages are primarily of the M2-phenotype, which are strongly linked to tissue healing and remodeling [56]. Keloid-derived macrophages exhibit a hyperactivated state with greater M2 polarization and increased overall expression of M1 and M2 activators as compared to normal skin macrophages. By secreting PDGF-CC and TGF- $\beta$ , which both favor collagen deposition and scar formation, these M2 macrophages can promote the conversion of fibroblasts into myofibroblasts, indicating a potential role for M2 macrophages in fibrosis [57, 58]. In patients with hypertrophic scars (HTS), CD163-positive M2 macrophages may be seen 4-6 weeks after injury, but only after 2 weeks in patients with normal scar formation [59]. Moreover, as HTS formation advances, IL-10 and IL-1RN concentrations continue to fall and return to normal levels after 6 months [60]. 24 months after injury, the expression of Arg-1 and CD206 declines, and the quantity of M2 macrophages (CD68<sup>+</sup> and CMAF<sup>+</sup>) reaches the pre-injury level.

Researchers have created a nude mouse model of human hypertrophic scar (HTS) by transplanting scar tissue from HTS patients into the mice. This model exhibits increased thickness, higher collagen levels, and infiltration of myofibroblasts. M2 macrophages occurred in considerable numbers late 3–4 weeks after transplantation, which was concurrent with the development of fibrosis in human skin tissue. In allografted skin, M1 macrophages were observed primarily 1-2 weeks after grafting [61].

### 2. T Lymphocytes

Due in part to the variety of T cell subsets, T cells contribute to the development of scars through multifaceted functions. In addition to the distinction between CD8<sup>+</sup> cytotoxic T cells and CD4<sup>+</sup> helper T cells, Th1, Th2, Th17, Tfh, and regulatory T (Treg) subpopulations of CD4<sup>+</sup> T cells can be distinguished based on transcriptome and effector cytokines. By secreting IFN- $\gamma$  and MMPs, which prevents fibroblast proliferation and suppresses the expression of type I and III collagen, Th1 cells can decrease tissue fibrosis [62]. In contrast, Th2 cells' released IL-4, IL-5, IL-13 and TIMPs can stimulate the production and metabolism of collagen in a fibrosis model, resulting in the accumulation of reticular fibrin protein [63]. The growth of IL-10-producing Treg cells may also be assisted by TGF-1 $\beta$ -producing Treg cells [64]. In fibroblasts, IL-10 directly reduces the production of collagen [65]. In addition to regulating fibroblasts directly, Treg cells also work with other T helper cells to influence the deposition of collagen and subsequent scar formation [66].

### 3. Fibroblasts

Myofibroblasts, the primary contractile and scar-depositing cell type in charge of ECM buildup, can be produced from resting resident skin fibroblasts either by trans-differentiation or from multilineage-differentiating, self-renewing fibroblast progenitors. In keloids, certain fibroblasts may be seen embedded in the collagen matrix (e.g., types I, III, V, and VI collagen), frequently displaying myofibroblastic characteristics and prominently expressing marker proteins, including  $\alpha$ -SMA and vimentin. In keloid scars, fibroblasts have a variety of characteristics compared to normal wound healing.

Studies show that a reduction in apoptosis leads to a cumulative rise in the number of keloid fibroblasts [67-69]. By the elevation of anti-apoptotic capability, telomere dysfunction, and senes-



---

cence abnormalities, apoptosis is also decreased in keloid fibroblasts. The activation of telomerase and subsequent telomere lengthening seen in keloid fibroblasts supports the life-extending impact of telomere dysfunction for this skin disease [70]. In 3D invasion experiments, keloid fibroblasts also exhibit greater migratory and invasion potential [71].

According to the heterogeneity of keloid fibroblasts, they can be divided into 4 subpopulations: secretory-papillary, secretory-reticular, mesenchymal, and pro-inflammatory [55]. As compared to normal scars, keloid scars have a much higher number of fibroblast subpopulations, which are essential for the exuberant collagen deposition seen in keloids. It's interesting to note that various scar forms may have varying levels of cellular heterogeneity. For instance, keloid fibroblasts' propensity to develop into adipocytes in response to BMP4 or when co-cultured with human scalp hair follicle cells [72]. According to studies, keloid fibroblasts have a great ability for self-renewal and are resistant to drugs, which allows them to sustain themselves through asymmetric cell division [73]. The typical tumor-like keloid development is thus set in motion by the ongoing production of new aberrant fibroblast cells, which also helps to explain their high post-treatment recurrence rates. The pathological keloid microenvironment may also be the primary cause of keloid cell production, with overexpression of growth factors within its microenvironment in turn leading to an enhanced and persistent inflammatory response.

### **2.3 Skin fibroblast subpopulations in mobilized skin fascial tissue promote wound healing**

Deep skin wounds may be assisted by muscle contraction, fibroblast differentiation, and extracellular matrix deposition, according to earlier studies. Our research revealed that during deep wound healing, the fascial layer of the skin, a loose layer of connective tissue containing a large number of fibroblasts, ECM, blood vessels, and nerves, migrate toward the center of the wound and contracts, thus promoting wound healing [74].

The fascia is a viscoelastic tissue that is filled with fluid, and it serves to create a smooth and slidable interface between organs and tissues throughout the body [75]. The cutaneous ligaments provide a three-dimensional network between the fat lobules by connecting the deep fascia and superficial fascia to the epidermis [76]. In humans, the fascial layer is composed of sensory neurons, fibroblasts, lymphatic arteries, adipose tissue, and a neurovascular network [77]. Skin fibroblasts are one of them, making up a diverse cell population with a variety of as-yet-undefined traits. We found that the main cause of numerous types of pathological scars was attributed to En1-past fibroblasts (EPFs), which were characterized by transient expression of the engrailed-1 (En1) transcription factor during the embryonic stage. On the contrary, En1-lineage-naïve fibroblasts (ENFs) were not involved in the formation of scars. Both EPFs and ENFs co-inhabit similar skin dermal compartments. To monitor EPFs, we crossed *En1<sup>Cre</sup>* mice with *R26<sup>mTmG</sup>* mice which express green fluorescence protein (GFP) in vivo, and ENFs, which retain the original red fluorescence protein (RFP) [78]. We found that ENFs were responsible for dermal development and regeneration once injured at early fetal stages of development [79]. Whereas EPFs gradually increased in population and outnumbered ENFs at newborn stages. EPFs primary role was during adult wound healing, and their ablation reduced connective tissue buildup and scarring around the wound.

---

To curb fascial tissue from moving toward the wound bed, we grafted polytetrafluoroethylene (ePTFE) membranes between fascial tissue and the panniculus carnosus (PC) muscle in a full thickness skin wound healing mouse model [74]. We discovered that the wounds in the ePTFE group of mice remained completely open, whereas the wounds in the control group healed completely within 21 days. Two months later, the EPFs pulled out from the borders of the incision and from the fascia underneath the membrane without leaving scars. As a result, when fascial mobility was absent, the dermal EPFs or other resident dermal fibroblasts were incapable of effectively healing wounds. These findings serve a clear indication that scar tissue is predominantly of fascial origin. The fascia of *En1<sup>cre</sup>;R26<sup>DTR</sup>* animals and the dermis of wild-type mice were then combined to form chimeric grafts. Diphtheria toxin (DT) was used to genetically deplete facial EPFs from the chimeric tissues, and the matrix was fluorescently tagged before grafting. The study's results showed that the tagged matrix persisted in the fascial layer underneath the incision, but when the fascial EPFs were ablated, it prevented the matrix from entering the wound. Thus, the resident EPFs that originate from the fascia play an active role in guiding the fascial matrix to close the open wound.

*Shamik Mascharak et al.* identified a subset of dermal ENFs that create EPFs by inducing the expression of *En1* during adult wound healing using cell transplantation and transgenic mice models [80]. They discovered that reticular dermal ENFs activate through the normal *En1* mechano-transduction signal by observing how ENFs react to matrix mechanics. According to mouse wound models, suppressing Yes-associated protein (YAP) reduces *En1* activation, increases wound regeneration of ENFs, and restores skin appendages, ultrastructure, and mechanical strength through limiting mechano-transduction signaling.

Hence, research into EPFs may open new therapy options for diseases that cause skin scarring. The p120 catenin protein was initially discovered through a screening for substrates of the Src tyrosine kinase. It is a 120kDa protein, and its phosphorylation on tyrosine residues has been found to correlate with cellular transformation [81]. It has been demonstrated that p120 catenin controls intercellular adhesion through its interaction with the cytoplasmic association membrane domain of cadherins.

We discovered that AAV8 had the highest transactivation efficacy in fascial fibroblasts *in vivo* after screening for AAV pseudotypes in **Publication I**. Using AAV8 as a gene expression modification tool, we next examined the efficiency of AAV8 transfection of fascia *in vivo* and found that most of it transfected into fibroblasts of the fascial layer (Pdgfra<sup>+</sup>). Moreover, we discovered that p120 expression dramatically increased at day 5 after injury and co-localized with EPFs in the fascia, before declining at day 21 after injury. p120 knockdown lowered N-cadherin and  $\alpha$ -SMA expression in wounds and decreased collagen in ECM, allowing scarless wound healing outcomes to resurface. This was accomplished via AAV8-mediated silencing of p120 by short hairpin (sh) RNA.

Previous research had shown that fascial resident EPFs fibroblasts mobilized an influx of ECM from the fascial layer into the wound [74, 82, 83]. By fluorescently labeling the skin fascia's ECM with NHS ester dye, we tested the hypothesis that inhibiting p120 in EPFs would stop fascial ECM from moving *in vivo*. As compared to the AAV8 control shRNA group, the matrix from the wound bed in the fascial layer was dramatically reduced in AAV8 p120 shRNA group.

In conclusion, our studies demonstrated that therapeutic manipulation of p120 in fascial fibroblasts improved wound healing. AAV8 p120 shRNA administered subcutaneously efficiently in-

---

hibited fascial fibroblasts from migrating in a group, promoting wound healing, and greatly reducing scarring. The ability of the AAV8 vector to target fascial mobilization and the translational application of this technology in altering the endogenous healing response could be used to restore the function of injured tissue without scarring.

## 2.4 Migrating adipocytes cannot be converted to myofibroblasts in skin wound healing

Adipocytes are being recognized as key participants in maintaining tissue homeostasis and modulating organ regeneration in various organ systems beyond adipose tissue. They can be found in two types of white adipose tissue in the skin: dermal white adipose tissue (dWAT) and subcutaneous white adipose tissue (sWAT). Recent studies in mice have revealed that dWAT differs from sWAT in terms of its development, morphology, and function. Specifically, dWAT plays a critical role in regulating body temperature, regulating hair growth, and facilitating wound healing [84].

Myofibroblasts, on the other hand, have traditionally been thought of being terminally differentiated cells. A recent study has demonstrated that myofibroblasts, which are considered to be non-adipogenic cells, may be converted to adipocytes during wound healing, demonstrating the trans-differentiating capability of these cells [72]. Fatty acids and hormones that control inflammation and glucose metabolism can be produced by adipocytes [85, 86]. The role of adipocytes has led to the hypothesis that they may play a crucial role in wound healing through growth factor secretion, angiogenesis, and the deposition of type VI collagen.

*Shook et al.* investigated the impact of dermal adipocytes on in vivo wound healing [87]. Tamoxifen-induced dermal adipocyte ablation was achieved by using *Adipoq<sup>CreER</sup>;iDTR* transgenic mice, although other adipose depots were mostly unaffected. Skin wound healing was significantly delayed as a result of the loss of dermal adipocytes, and the recruitment of inflammatory macrophages was also compromised. Dermal adipocytes completed a dedifferentiation process to express *Pdgfra/Pdgrβ* resembling fibroblasts. *Adipoq<sup>CreER</sup>;R26<sup>mT/mG</sup>* mice lineage-tracing strategies had revealed that adipocytes located near the edge of a wound undergo a series of transformations. These cells broke down their lipid droplets, which led to the downregulation of adipocyte-specific genes such as *PPAR-γ* and *Perilipin-1 (Plin1)*. As a result, the adipocytes acquired a fibroblast-like appearance before migrating into the wounded tissue.

It is widely believed that communication between fibroblasts and adipocytes involves the exchange of cell markers. For instance, fibroblasts may express the adipocyte marker *Plin1*, while adipocytes may express the fibroblast marker  $\alpha$ SMA. However, these markers alone are insufficient to determine cell identity. In addition to marker expression, cellular plasticity is also dependent on morphological changes. For instance, adipocytes can transition from a rounded shape to a flattened, bipolar shape characteristic of fibroblasts. Nonetheless, relying solely on phenotype can be misleading, as mature adipocytes can lose their lipids under certain metabolic conditions, making them harder to distinguish from fibroblasts. Therefore, a more comprehensive study of the molecular and cytoarchitectural changes involved in the injury response is necessary to fully understand the cellular plasticity between fibroblasts and adipocytes.

In **Publication II**, we investigated the stepwise transcriptional and functional responses of mature adipocytes and fibroblasts following skin injury using a combination of genetic lineage tracking

---

strategies, single-cell transcriptomes, live cell imaging and computational tracking, transplantation assays, and in vivo injury models. Morphological regulation of wounded adipocytes in injured tissues was observed, but there was no evidence of an adipogenic origin of fibrotic cells during injury, nor was there evidence of transformation or cell fusion from adipocytes to fibroblasts by assessing transcriptomic, behavioral, or functional criteria.

We analyzed the gene expression of GFP<sup>+</sup> cells in the skin of *En1<sup>Cre</sup>;R26<sup>mTmG</sup>* mice and *Adipoq<sup>Cre</sup>;R26<sup>mTmG</sup>* mice by ex vivo culturing at different days with single-cell RNA sequencing, and found no overlap and no confluence in these 12 clusters of single-cell sequencing data, which remained independent. By performing live imaging of the in vitro experiments, we found that from day 0 to day 2 the adipocytes had a gradual reduction in round cells and an increase in the oval, spindle, and elongated morphology. Between day 3 and 5, this phenotype reversed and returned to a strictly round morphology. In vivo wound experiments had shown that adipocyte lineage cells undergo a transition in morphology following injury. By day 7, these cells acquired a fibroblast-like appearance and migrate from their original location in the dWAT to the wound bed. By day 21, elongated adipocyte lineage cells could be observed clustering near the scar area, while nearby adipocytes in non-wounded skin retained their characteristic rounded morphology. These findings suggest that adipocytes are capable of undergoing a transitional change in morphology and actively migrating while maintaining their identity as adipocytes.

*En1<sup>Cre</sup>;R26<sup>mTmG</sup>* mice and *Adipoq<sup>Cre</sup>;R26<sup>mTmG</sup>* mice were used to perform full-thickness excisional wounds on the dorsal back skin, and on day 10 and 21, FACS was used to sort GFP<sup>+</sup> cells (adipocytes from Adipoq-lineage mice, and fibroblasts from En1-lineage mice) for bulk sequencing. Wound fibroblasts were shown to be enriched for matrix deposition and matrix regulation, and cell-matrix adhesion by using gene ontology enrichment analysis. Adipocytes from wounds on day 10 were, in contrast, more highly enriched in sensory perception, immunological regulation, and antimicrobial responses. Migrating adipocyte-lineage cells, which were distinct from fibrogenic cells, lacked the fibroblast markers  $\alpha$ SMA and vimentin as well as the proliferation marker Ki67.

In summary, we demonstrate an irreversible cell fate of mature adipocytes during skin injury, despite their significant morphological changes and migratory behavior. Wounded adipocytes remain linearly restricted in their response to tissue injury and do not differentiate and do not fuse with or convert to myofibroblasts. Adipocytes respond to traumatic stimuli with a shift in motility and function and play an active but distinct role in the endogenous tissue healing response.

---

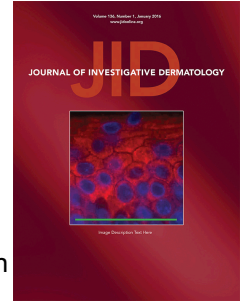
### **3. Paper I**

#### **Therapeutic silencing of p120 in fascia fibroblasts ameliorate tissue repair**

Vijayanand Rajendran, Pushkar Ramesh, Ruoxuan Dai, Shruthi Kalgudde Gopal,

Haifeng Ye, Hans-Günther Machens, Heiko Adler, Dongsheng Jiang, Yuval Rinkevich

# Journal Pre-proof



Therapeutic silencing of p120 in fascia fibroblasts ameliorate tissue repair

Vijayanand Rajendran, Pushkar Ramesh, Ruoxuan Dai, Shruthi Kalgudde Gopal, Haifeng Ye, Hans-Günther Machens, Heiko Adler, Dongsheng Jiang, Yuval Rinkevich

PII: S0022-202X(22)02821-4

DOI: <https://doi.org/10.1016/j.jid.2022.10.018>

Reference: JID 3625

To appear in: *The Journal of Investigative Dermatology*

Received Date: 20 June 2022

Revised Date: 22 October 2022

Accepted Date: 31 October 2022

Please cite this article as: Rajendran V, Ramesh P, Dai R, Kalgudde Gopal S, Ye H, Machens H-G, Adler H, Jiang D, Rinkevich Y, Therapeutic silencing of p120 in fascia fibroblasts ameliorate tissue repair, *The Journal of Investigative Dermatology* (2022), doi: <https://doi.org/10.1016/j.jid.2022.10.018>.

This is a PDF file of an article that has undergone enhancements after acceptance, such as the addition of a cover page and metadata, and formatting for readability, but it is not yet the definitive version of record. This version will undergo additional copyediting, typesetting and review before it is published in its final form, but we are providing this version to give early visibility of the article. Please note that, during the production process, errors may be discovered which could affect the content, and all legal disclaimers that apply to the journal pertain.

© 2022 The Authors. Published by Elsevier, Inc. on behalf of the Society for Investigative Dermatology.

## Therapeutic silencing of p120 in fascia fibroblasts ameliorate tissue repair

Vijayanand Rajendran<sup>1</sup>, Pushkar Ramesh<sup>1</sup>, Ruoxuan Dai<sup>1</sup>, Shruthi Kalgudde Gopal<sup>1</sup>, Haifeng Ye<sup>1</sup>, Hans-Günther Machens<sup>2</sup>, Heiko Adler<sup>3</sup>, Dongsheng Jiang<sup>1</sup>, Yuval Rinkevich<sup>1,\*</sup>

<sup>1</sup>Institute of Regenerative Biology and Medicine, Helmholtz Zentrum München, Munich, Germany

<sup>2</sup>Department of Plastic and Hand Surgery, Klinikum rechts der Isar, School of Medicine, Technical University of Munich, Munich, Germany

<sup>3</sup>Institute of Asthma and Allergy Prevention, Helmholtz Zentrum Muenchen, Munich, Germany, and German Center for Lung Research (DZL), Giessen, Germany

### \*Correspondence:

Dr. Yuval Rinkevich

Address: Max-Lebsche-Platz 31, 81377 Munich, Germany

Telephone: +49 (89) 3187 4685

Fax: +49 (89) 3187 4661

Email: [yuval.rinkevich@helmholtz-muenchen.de](mailto:yuval.rinkevich@helmholtz-muenchen.de)

### Keywords:

p120; AAV; Skin; Fascia; Fibroblasts; Wound; Scar

### ORCID:

Vijayanand Rajendran	0000-0002-6583-4044
Pushkar Ramesh	0000-0002-6815-4626
Ruoxuan Dai	0000-0003-4669-1022
Shruthi Kalgudde Gopal	0000-0001-7053-919X

Haifeng Ye	0000-0001-6762-7260
Hans-Günther Machens	0000-0002-3852-6433
Heiko Adler	0000-0002-6481-6709
Dongsheng Jiang	0000-0003-0961-2671
Yuval Rinkevich	0000-0003-3658-0257

Journal Pre-proof



**ABSTRACT**

Deep skin wounds rapidly heal by mobilizing extracellular matrix and cells from the fascia, deep beneath the dermal layer of the skin, to form scars. Despite wounds being an extensively studied area and an unmet clinical need, the biochemistry driving this patch-like repair remains obscure. Lacking also are efficacious therapeutic means to modulate scar formation *in vivo*. Here, we identify a central role for p120 in mediating fascia mobilization and wound repair. Injury triggers p120 expression, largely within engrailed-1 lineage positive fibroblasts (EPFs) of the fascia that exhibit a supra-cellular organization. Using adeno-associated virus (AAV) mediated gene silencing, we show that p120 establishes the supracellular organization of fascia EPFs, without which fascia mobilization is impaired. Gene silencing of p120 in fascia fibroblasts disentangles their supracellular organization, reducing the transfer of fascial cells and extracellular matrix into wounds, and augments wound healing. Our findings place p120 as essential for fascia mobilization, opening a new therapeutic avenue for targeted intervention in the treatment of a variety of skin scar conditions.

## INTRODUCTION

Tissue scarring is a pivotal step in mammalian wound repair following injury. Scars replace the healthy reticular connective tissue foundation with irregular dense meshwork of connective tissue matrix that severely restrict the tissue's biomechanical, physiological and functional performance. Scarring is ubiquitous after surgery or acute trauma, and excessive scarring is a crucial stage of many chronic diseases that leads to organ dysfunction, failure, and death (Sen, 2019). Up to 45 percent of all deaths in the world are attributed to the progression of scar disorders (Eming et al., 2014, Gurtner et al., 2008, Marshall et al., 2018). Several key limitations hinder anti-scar therapies from becoming widespread and utilized across diverse clinical indications.

The first limitation arises from our current incomplete knowledge of how scars are formed in animals and the precise pathomechanism underpinning this process for effective, targeted treatments to be developed. Scar formation has traditionally been viewed as a pathology of *de novo* matrix synthesis and deposition by fibroblasts on site (Eming et al., 2014; Gurtner et al., 2008; Sen, 2019). This has provided the foundation for most anti-scar and anti-fibrotic approaches under clinical development, focusing on reducing fibroblast activation and collagen synthesis (such as transforming growth factor-beta [TGF- $\beta$ ] signalling). Success in translating such drug candidates into effective treatments in clinical trials is slow and hampered by the fact that this mechanism is difficult to precisely target, resulting in many adverse effects systemically.

In sharp contrast to the view of scarring as a pathology of excessive and *de novo* matrix deposition, we recently demonstrated that scars in skin originate from pre-existing extracellular matrix (ECM) positioned underneath the dermis. In response to injury, a viscoelastic membranous sheet of loose connective tissue termed superficial fascia, which creates a thin gelatinous and frictionless interface between the skin and the body's interior rigid structures,

is dragged upwards and mobilized into wounds, resulting in scar formation (Correa-Gallegos et al., 2019). These findings highlighted fascia mobilization as an untapped avenue to identify anti-scarring treatment mechanisms independent of *de novo* collagen synthesis (Jiang & Rinkevich, 2021). Our follow-up studies have demonstrated that fascia mobilization during wound repair is driven by a swarming-like collective migration of fascia fibroblasts from the wound periphery towards the wound center (Jiang et al., 2020). This directional collective migration of fascia fibroblasts forms a myofibroblast cell aggregate at sites of wounds that requires elevated intercellular communication and adhesion via N-cadherin-based adherens junctions and Connexin 43-based gap junctions (Jiang et al., 2020; Wan et al., 2021). The upstream signal that instructs upregulation of N-cadherin and Connexin 43 in fascia fibroblasts upon injury has not been identified.

The second limitation is the lack of a delivery vehicle that can effectively target dermal and fascia fibroblasts. The most attractive vectors of choice are Adeno-Associated Viruses (AAVs). These are small (26 nm in diameter) non-enveloped parvoviruses (Wang et al., 2019) that provide persistent high-level transgene expression and minimal post-infection immunogenicity and pathogenicity. AAV vectors have been evaluated in 149 clinical trials worldwide (Kuzmin et al., 2021), providing evidential support for the safety and feasibility of AAV-mediated gene delivery in therapeutic development. In preclinical models, AAV-mediated gene transfer has demonstrated *in vivo* efficacy with proven tropism to epidermal muscle cells, hepatocytes, pancreatic cells, and heart muscle (Galeano et al., 2003; Jazwa et al., 2010; Keswani et al., 2012). AAV pseudotypes that show efficient transduction to stromal cells *in vivo* have been not optimal (Kumar et al., 2004, McMahon et al., 2006, Stender et al., 2007). Thus, identifying gene transfer applications that can target and transduce dermal and fascia cells at high efficiency *in vivo* would theoretically enable their widespread applicability in treating wounds across diverse medical conditions.

Here, we undertake a screen of AAV pseudotypes and determine AAV8 as having the highest transduction efficacy in fascia fibroblasts *in vivo*. Using AAV8 as a gene-expression modification tool, we explore the potential role of p120-catenin (p120) in fascia mobilization, wound healing, and scar formation. p120 catenin has been demonstrated to regulate cell-cell adhesion through its interaction with the cytoplasmic juxta-membrane domain of cadherins (Yanagisawa and Anastasiadis, 2006), and it is essential for intercellular adhesion (Pettitt et al., 2003; Myster et al., 2003). In this study, we demonstrate in animals that AAV8 mediated short hairpin (sh) RNA silencing of p120, predominantly in fascia fibroblasts, reduces ECM mobilization and enables re-emergence of scarless wound repair outcomes. Our findings demonstrate the potential for targeting mechanisms of fascia mobilization with AAV8 vectors and the translational applications of this technology in modulating endogenous repair responses to restore the function of injured tissues in a scarless fashion.

## RESULTS

### AAV Capsid Screening for efficient transduction of fascial fibroblasts.

Our initial experiments were designed to evaluate the transduction capability of different AAV capsids and to identify the most suitable serotype for transducing fibroblasts in an established murine whole skin-fascia explants (Jiang et al., 2020). Several AAV capsids (AAV2, AAV6, AAV7, AAV8, AAV9 and AAV-DJ) were used for packaging the AAV reporter genome expressing green fluorescent protein (GFP) under the control of the human cytomegalovirus (CMV) promoter. All AAVs were incubated with murine skin-fascia explants and GFP expression in transduced cells was assessed by immunohistochemical staining using an anti-GFP antibody on cryosections of transduced explants with epidermis facing upwards and fascia bellow, three days post-infection (**Figure 1a**). AAV8 displayed a significantly higher percentage of transduced GFP-expressing cells among the serotypes tested (**Figure 1a and b**). Further, to test AAV8's ability to target the fascia fibroblasts *in vivo*, AAV8-GFP was injected

subcutaneously into C57BL/6 mice at postnatal day 3 (P3), and GFP expression was assessed three days post-injection. CMV-driven GFP was detected in the fascia layer and within fibrogenic lineage cells that express fibroblast specific protein 1 (Fsp1), demonstrating that subcutaneous delivery routes of AAV8 effectively transduce fascia fibroblasts (**Figure 1c**). Furthermore, we subcutaneously injected AAV8-GFP surrounding the wounds on the back of P3 mice, and examined the cell types that were transduced in wounded region by immunostaining for various cell type specific markers. Within total transduced GFP-positive cells, 4.6% were CK14<sup>+</sup> epidermal cells (Supplementary Figure 1a and g), 6.5% were CD31<sup>+</sup> endothelial cells (Supplementary Figure 1b and g), 10.1% were CD45<sup>+</sup> immune cells (Supplementary Figure 1c and g), and the majority of transduced cells in wounds were PDGFR $\alpha$ <sup>+</sup> fibroblasts (Supplementary Figure 1d and g). Within the fibroblast population, 58.3% and 79.3% of GFP<sup>+</sup>PDGFR $\alpha$ <sup>+</sup> fibroblasts expressed the fascia fibroblast markers N-cadherin (Supplementary Figure 1e and g) and Sca1 (Supplementary Figure 1f and g), respectively. This data indicates that fascia fibroblasts are the most prominent cell population transduced by AAV8 in wounds.

### **AAV8 transduced fascia fibroblasts efficiently establish a wound scar**

We have previously shown that fascia fibroblasts respond to skin injury by steering the fascia's ECM and cells into open wounds, thereby establishing a provisional wound scar. We reasoned that subcutaneous injection of AAV viral particles into the fascia surrounding the wound could yield an efficiently transduced population of wound myofibroblasts. To evaluate whether AAV8 transduced fascia fibroblasts are steered into wounds in vivo, we injected the AAV8-GFP virus into the fascia surrounding wounds on the dorsal back skin. At 7 days post-wounding (dpw), 71.1% of wound resident fibroblasts were GFP positive, in which majority of them were derived from the transduced fascia (**Figure 2a and b**). The transduced GFP-positive fibroblasts

in wound bed expressed myofibroblast markers alpha Smooth Muscle Actin ( $\alpha$ SMA), Dipeptidyl peptidase-4 (also known as Cluster of Differentiation 26; CD26) and ER-TR7 (**Figure 2c and d**). Taken together, our findings indicate that subcutaneous delivery of AAV8 particles represents a valuable method for targeted manipulation of fascia-sourced wound myofibroblasts.

We next examined the efficacy of AAV8 to transfect the fascia in vivo in an independent genetic system. AAV8 capsids were used for packaging a Cre plasmid before subcutaneous injection into the fascia of R26<sup>mT/mG</sup> reporter mice. These reporter mice harbor a loxP-flanked STOP cassette that prevents transcription of the downstream GFP in the absence of Cre recombinase (**Figure 2e**). Healthy non-injured skin tissue at sites of AAV8 injection were excised at day 7 post-injection, and placed with the fascia-side facing up for imaging. Robust GFP signals at sites of AAV8-Cre injection were observed, indicating achievement of transduction and recombination in fascia cells (**Figure 2f**). Subsequently, AAV8-Cre was injected subcutaneously followed by generating full thickness wounds. Transverse cross-section of wounds at day 7 post-wounding showed accumulation of transduced GFP positive fascia cells in wound bed that expressed the myofibroblast marker  $\alpha$ SMA (**Figure 2g**).

### **p120 is upregulated in fascia EPFs upon injury**

Having established a translational system for modulating gene expression of fascia fibroblast in vivo (as our predominant target), we examined the gene modulatory prowess of p120-catenin (p120) to steer wounds into scarless repair. Excisional wounds generated on the dorsal backs of wild-type (WT) mice showed upregulation of p120 in wound fibroblasts in vivo compared to negligible expression levels in unwounded skin (**Figure 3a and b**). p120 protein was specifically upregulated in the pro-fibrotic lineage En1-lineage positive fibroblasts (EPFs) when full-thickness excisional wounds were generated on the back-skin of En1<sup>Cre</sup>;R26<sup>mTmG</sup>

double transgenic mice. At 5 days post-wounding, p120 was robustly expressed and colocalized with fascia EPFs within the wound bed (**Figure 3c**), and P120 expression returned to lower level at 21 days post-wounding (Supplementary Figure 2a and b). These results collectively demonstrated that p120 is highly expressed in the scar-forming fibroblast lineage throughout the wound repair process. p120 has been reported to bind directly to N-cadherin thereby stabilizing intercellular adherent junctions (Yanagisawa and Anastasiadis, 2006), and our previous study showed a crucial role of N-cadherin in fibroblast collective migration (Jiang et al., 2020). We, therefore, went on to target p120 in fascia fibroblasts in order to investigate whether p120 plays functional role in collective migration, fascia mobilization and scar severity. To effectively knock down the p120 expression in vivo, we generated an AAV8 virus expressing either a p120 shRNA or a non-targeted shRNA (control shRNA) coupled to GFP under the human cytomegalovirus (CMV) promoter. To demonstrate the effectiveness of the p120 shRNA system, primary fascia fibroblasts were transduced with an AAV8 p120 shRNA and AAV8 Control shRNA virus (**Figure 3d**). Western blot results showed that transduction with AAV-P120 ShRNA significantly reduced p120 protein expression (**Figure 3e**). In addition, qRT-PCR of RNA extracts from primary fibroblasts was performed to verify the knockdown specificity. AAV8-p120 shRNA transduction significantly reduced p120 mRNA relative to AAV Control shRNA (**Figure 3f**), validating our AAV8 p120 ShRNA construct system to reduce p120 expression in the fascia effectively.

### **p120 promotes fascia mobilization into wounds**

To directly examine the relevance of injury-induced upregulation of p120 to fascia mobilization, scar formation and wound repair in vivo, we turned to our AAV8 system in order to ablate the expression of p120 in fascia fibroblasts in the context of full thickness wounds on the backs of mice. Quantitative immunofluorescence measurements of wounds revealed a

significant reduction in p120 and  $\alpha$ SMA intensity in wounds from mice injected with AAV8 p120 shRNA compared to control shRNA (**Figure 4a-d**). Knocking down p120 significantly reduced N-cadherin expression levels in wounds (Supplementary Figure 2c and d). Whereas immune cell infiltration and cell viability in wounds were not affected by the treatment of AAV8 p120 shRNA, as demonstrated by immunostaining of CD45 (Supplementary Figure 2e and f) and active Caspase 3 (Supplementary Figure 2g and h), respectively. At day 7 post-injection, we observed significantly lower collagen expression within the wound area in our AAV8 p120 shRNA injected group (**Figure 4e and f**). In addition, scar size from AAV8 p120 shRNA transduction experiments was significantly smaller than those from controls (**Figure 4g and h**).

To further study how p120 silencing reduces wound myofibroblasts, we established an *ex vivo* live imaging setup. Following skin injury, WT mice received a subcutaneous injection of AAV8 p120 shRNA or AAV8 control shRNA. Wounds were excised on day 5 post-injection, and kept in culture media in a 37°C chamber with 5% CO<sub>2</sub>. Live imaging was then performed with fascia-side face-up for 24 h in order to directly visualize the transduced GFP<sup>+</sup> cells inside the wound bed. Transduced fascia cells in AAV8 control shRNA treated wounds exhibited polarized morphologies with extensive cellular protrusions and a collective migration phenotype reminiscent of wounds in untransfected mice. Conversely, p120-silenced fascia cells were poorly polarized with a significant reduction in fibroblast protrusion length compared to control fibroblasts (**Figure 5a and b**). Moreover, transduced fascia cells in control wounds clustered together and formed multicellular clusters. By contrast, in AAV8 p120 shRNA treated wounds, intercellular junctions were completely lost (**Figure 5c**), and fibroblasts showed significant reduction of cell membrane branches (**Figure 5d**). To directly analyze changes in fibroblast dynamics in response to p120 silencing, we performed particle image velocimetry (PIV) analysis on live image videos tracking single fascia fibroblasts. Transduced



fascia cells in control wounds exhibit directed (peripheral-to-central) movement with collective migration towards the wound region, whereas p120 silenced fascia cells had substantially reduced migration distances and lacked collective migration behaviors (**Figure 5e and f**). These results indicate a crucial role for p120 in stabilizing the supracellular organization of fascia fibroblasts needed for effective mobilization of the fascia tissue into wounds.

Recently we showed that fascia resident EPF fibroblasts physically mobilize the fascia ECM into the wound (Correa-Gallegos et al., 2019; Jiang et al., 2020; Wan et al., 2021). To further investigate whether p120 depletion in fibroblasts blocks mobilization of fascial ECM in vivo, we fluorescently ‘tagged’ the fascia ECM with NHS ester dye by directly injecting NHS-fluorescein into the subcutaneous space of the back skin prior to creating full-thickness excisional wounds (**Figure 5g**). After the injury, AAV8 control shRNA or AAV8 p120 shRNA was subcutaneously injected into the fascia surrounding the wound edge. Wounds receiving AAV8 control shRNA showed accumulation of ECM within wounds with 64.8% of the wound bed matrix labelled with NHS ester and therefore mobilized from fascia adjacent to the wound. In contrast, wounds receiving AAV8 p120 shRNA had drastically reduced ECM, with only 28.9% of wound bed matrix originating from the fascia (**Figure 5h and i**).

Collectively, our experiments demonstrate enhanced wound repair by therapeutic modulation of p120 in fascia fibroblasts. Functionally, we show that subcutaneous delivery of AAV8 p120 shRNA effectively blocks fascia fibroblast collective migration needed for fascia mobilization into wounds, thereby producing wound healing with significantly reduced scars.

## DISCUSSION

Clinical practice of dermal scars relies primarily on scar tissue management rather than its therapeutic amelioration. For example, topical management options normally include invasive procedures such as surgical scar corrections, intralesional application of corticosteroids,

physical laser- or radiotherapy, and radiotherapy directly after surgical scar correction, either separately or in combination. Additional non-invasive treatment options exist, including the physical application of pressure forces, often in combination with applied silicone sheets and gels, static/dynamic splints, massage therapy or the use of dermatologic ointments, oils, lotions, creams (Monstrey et al., 2014), all of which show limited clinical efficacy in reducing scars during wound management.

To date, there has been no efficient demonstration of therapeutic improvement of wound repair by targeted delivery methods into the fascia. This is primarily due to a lack of mechanistic understanding of the central role of the fascia in wound repair but also due to a lack of efficacious approaches for targeted modulation of fascia tissue *in vivo*. Here, we overcome these milestone gaps by (a) identifying p120 as a targetable molecule for scar prevention that is highly expressed in fascia EPFs in response to injury and (b) discovering the fundamental role of p120 in steering fascia cells and ECM into wounds, and (c) demonstrating translational efficacy of AAV8 p120 shRNA in improving wound repair outcomes in animals.

p120 is an adhesion junction protein known to function as a link between intercellular adhesion and signal transduction in various cells. p120 in glioma cells has been shown to play a critical role in cancer cell invasion, migration, and axonal growth (Gritsenko et al., 2020) as well as in motility of cultured stromal cells (Grosheva et al., 2001). Our previous studies identified N-cadherin as an essential intercellular adhesion molecule needed for fascia fibroblast collective cell migration into wounds (Jiang et al., 2020). p120 is essential for the formation of N-cadherin-based junctional complexes and cell polarity (Ozaki et al., 2010, *Cell Struct Funct*), and both N-cadherin and p120 are essential for directional collective migration of fibroblasts. N-cadherin has been shown to promote tumor cell invasion (Thoreson et al., 2000), and we speculate that p120 is involved in cellular invasion by either 1) upregulating and stabilizing N-cadherin through direct binding, or 2) directly remodeling the cytoskeleton via modulating

Rho-GTPase activity (Yanagisawa and Anastasiadis, 2006; Anastasiadis et al., 2000). Under the conceptual frame that tumors are wounds that do not heal (Dvorak, 1986; Dvora, 2015), we speculate that p120 may have similar physiological functions during wound repair.

Our study confirms that p120 is an essential regulator of the supracellular organization needed to mobilize fascia cells and matrix into wounds. Silencing of p120 modulates the extent of connective tissue matrix and cells being steered into wounds, thereby reducing wound scar severity in animals. Multiple doses of AAV8-mediated p120 knockdown are required for a longer period of p120 silencing. The development of p120 genetically modified animal models or p120-specific chemical inhibitors may also enable therapeutic modulation of wound repair. Our findings open a wide range of possibilities for exploring the therapeutic efficacy of gene delivery into the dermis and fascia with broad clinical implications and pharmaceutical value.

## MATERIALS AND METHODS

Detailed materials and methods are described in Supplementary Materials and Methods.

### Animals

For in vivo studies, C57BL/6J, and En1<sup>Cre</sup> mice were purchased from Jackson Laboratories and ROSA26<sup>mTmG</sup> (R26<sup>mTmG</sup>) reporter mice were obtained from Stanford University. The mouse lines were kept at the Helmholtz animal facility in compliance with the German Law for Welfare of Laboratory Animals. All experiments were approved by the Government of Upper Bavaria.

### Antibodies

The following antibodies were used: anti-goat FSP1 (1:200, ab58597), anti-mouse p120 catenin (1:250, BD610133), anti-rabbit  $\alpha$ SMA (1:250, ab5694), anti-rabbit Collagen type I (1:250, Rockland 600-401-103-0.1), anti-rabbit Collagen type III (1:200, ab7778), anti-goat CD26 (1:200, SAB2500328), anti-rabbit collagen type VI (1:200, ab6588, 1:150), anti-rat ERTR7 (1:500, ab51824), anti-rabbit GFP (1:250, ab290). Tissue sections were overlaid with relevant secondary antibodies (1:500) for 1 hour at Room Temperature (RT).

### Excisional wound model and AAV injection

Two-week wildtype mice were anaesthetized with MMF (Medetomidine at 0.5 mg.kg<sup>-1</sup>, midazolam at 5 mg.kg<sup>-1</sup>, and fentanyl at 0.05 mg.kg<sup>-1</sup>). Under analgesia, two 2mm full-thickness deep wounds (i.e., epidermis, dermis, and fascia) were generated on the back skin. The mouse received an injection of 10  $\mu$ l of AAV8-GFP, AAV8 p120 ShRNA, and AAV8 Control ShRNA virus at a titre of  $2 \times 10^{12}$  GC/ml in the area between the two wounds. After 7 days post-injury, the scar tissue was cryo-sectioned for histological and immunofluorescent analysis. Similarly, two 2-mm full-thickness excisional wounds were created on the back of

R26mTmG mice, and 20  $\mu$ l of AAV8-Cre virus at a viral titer of  $1 \times 10^{12}$  GC/ml was injected at the area between the wounds. The control mice received the injection of PBS. Scar tissues were harvested on day 7 post-wounding. Subsequently, the scar tissue was processed for cryo-sections for histology and immunofluorescence.

### ***Ex vivo live imaging***

Live imaging of transduced wound tissues was performed as described previously (Ramesh et.al, 2022). AAV8 p120 ShRNA or AAV8 Control ShRNA virus injected wound tissue were embedded in 4% agarose in a 35 mm-dish (Corning) and submerged in imaging medium phenol-red free DMEM/F-12 (Thermo Fisher Scientific) containing 10% KnockOut Serum Replacement, 1x GlutaMAX, 1x Penicillin/streptomycin, and 1x MEM non-essential amino acids. Time-lapse imaging was performed under a Leica SP8 MP (Leica, Germany), equipped with a modified incubation system with heating and gas control (ibidi) was used during imaging (37 °C, 5% CO<sub>2</sub>). 250 z-stacks and 65 time-frames were recorded for each imaged sample in approximately 24 h, which gives z-plane resolution of 2.4 – 2.6  $\mu$ m, and time interval of 22 – 29 min for each frame. Images were visualized and analyzed with the Imaris software package (v9.3.0, Bitplane, UK).

### **Particle Image Velocimetry (PIV) analysis of images**

Particle image velocimetry (PIV) has been used to describe collective cell migration. It compares the localization of signals in 2 images from 12-hour videos and computes the pixel flow trajectories between them. PIV analysis was performed using Fiji Plugin Iterative PIV from the 12 hrs live imaging video stacks of AAV8 p120 ShRNA, AAV8 Control ShRNA virus injected wound tissue. Stable pictures from the timelapse devoid of tissue drifts from early and final time points were converted into a 2-picture stack to derive these trajectories. Images were converted to an 8-bit stack, and the "iterative PIV" function was applied. Default values with

"Vector spacing" of 128, 64 and 32 pixels sub windows were applied. Calculated magnitude vectors were then used to measure direction and velocity.

### **Cell tracking and displacement analysis**

Drift correction was performed on live imaging dataset using ImageJ "Correct 3D drift" in reference to the non-cellular tissue autofluorescence. The Initial and final time point z stacks of drift corrected dataset were extracted and converted to 2D stacks using maximum intensity projection. The resulting x, y, t stacks were converted to binary images and further processed using the analysis pipeline of ImageJ plugin "Trackmate" (Jiang et al., 2018). Cell tracks and (x, y) spot coordinates were exported as .xml to excel and spot displacement values were computed using formula  $d = \sqrt{(x_2 - x_1)^2 + (y_2 - y_1)^2}$ .

### **Matrix labelling and AAV injection into the wound**

2-week-old C57BL6/J mice were injected with 5 $\mu$ l of NHS-fluorescein dye at 10mg/ml in PBS with 0.1 M sodium bicarbonate pH 9 (46,409, Life technologies) one day before wounding. 2 mm full-thickness excisional wounds were created in the labeled area and 10 $\mu$ l of AAV8 p120 ShRNA or AAV8 Control ShRNA virus at a  $2 \times 10^{12}$  GC/ml titre range was injected around the wounds. Wounds were harvested on day 7 post-wounding and fixed in 2% PFA at 4 °C overnight. After washing with PBS, tissue was embedded in OCT and cryo-sectioned.

### **Quantification and statistical analysis**

All statistical analyses were performed with GraphPad Prism 9.2 software. Data are presented as the means  $\pm$  standard error of the mean (SEM) or mean  $\pm$  standard deviation (SD). A two-tailed t-test (Student's t-test) was carried out for the statistical analysis to compare the two groups.  $P < 0.05$  was considered statistically significant. \* $P < 0.05$ ; \*\* $P < 0.01$ ; \*\*\* $P < 0.001$ ; and \*\*\*\* $P < 0.0001$ .

## **DATA AVAILABILITY STATEMENT**

All the data are available with the corresponding authors upon reasonable request. No large datasets were generated in the current study.

## **CONFLICT OF INTEREST**

The authors have declared that no conflict of interest exists

## **ACKNOWLEDGMENTS**

Y.R. was supported by the Human Frontier Science Program Career Development Award (CDA00017/2016), the German Research Foundation (RI 2787/1-1 AOBJ: 628819), the Fritz-Thyssen Stiftung (2016-01277), and the European Research Council Consolidator Grant (ERC-CoG 819933), Else-Kröner-Fresenius-Stiftung (2016\_A21), and the LEO Foundation (LF-OC-21-000835). We thank Dr Steffen Dietzel and the Core Facility Bioimaging at the Biomedical Centre of the Ludwig-Maximilians-Universität München for access and support with the multi-photon system.

## **AUTHOR CONTRIBUTIONS**

Conceptualization: YR, DJ; Data curation: VR, PR, RD, SKG, HY, HA, H-GM, DJ; Writing: VR, DJ, YR.

## REFERENCES

- Anastasiadis PZ, Moon SY, Thoreson MA, Mariner DJ, Crawford HC, Zheng Y, et al. Inhibition of RhoA by p120 catenin. *Nat Cell Biol.* 2000;2:637-644.
- Correa-Gallegos D, Jiang D, Christ S, Ramesh P, Ye H, Wannemacher J, et al. Patch repair of deep wounds by mobilized fascia. *Nature.* 2019;576(7786):287-292.
- Dvorak HF. Tumors: wounds that do not heal. *N Engl J Med.* 1986;315(26):1650-1659.
- Dvorak HF. Tumors: wounds that do not heal-redux. *Cancer Immunol Res.* 2015;3(1):1-11.
- Eming SA, Martin P, Tomic-Canic M. Wound repair and regeneration: mechanisms, signaling, and translation. *Sci Transl Med.* 2014;6(265):265sr6.
- Galeano, M., Deodato, B., Altavilla, D., Cucinotta, D., Arsic, N., Marini, H., et al. Adeno-associated viral vector-mediated human vascular endothelial growth factor gene transfer stimulates angiogenesis and wound healing in the genetically diabetic mouse. *Diabetologia.* 2003;46(4):546-555.
- Gritsenko, P. G., Atlasy, N., Dieteren, C. E. J., Navis, A. C., Venhuizen, J.-H, et al. p120-catenin-dependent collective brain infiltration by glioma cell networks. *Nat Cell Biol.* 2020;22(1):97-107.
- Grosheva I, Shtutman M, Elbaum M, Bershadsky AD. p120 catenin affects cell motility via modulation of activity of Rho-family GTPases: a link between cell-cell contact formation and regulation of cell locomotion. *J Cell Sci.* 2001;114(Pt 4):695-707.
- Gurtner GC, Werner S, Barrandon Y, Longaker MT. Wound repair and regeneration. *Nature.* 2008;453(7193):314-321.
- Jazwa A, Kucharzewska P, Leja J, Zagorska A, Sierpniowska A, Stepniowski J, et al. Combined vascular endothelial growth factor-A and fibroblast growth factor 4 gene transfer improves wound healing in diabetic mice. *Genet Vaccines Ther.* 2010;8:6.
- Jiang D, Christ S, Correa-Gallegos D, Ramesh P, Wannemacher J, et al. Injury triggers fascia fibroblast collective cell migration to drive scar formation through N-cadherin. *Nat Commun.* 2020;11(1):5653.



Jiang D, Correa-Gallegos D, Christ S, Stefanska A, Liu J, Ramesh P, et al.  
Two succeeding fibroblastic lineages drive dermal development and the transition from regeneration to scarring.  
*Nat Cell Biol.* 2018;20(4):422-431.

Jiang D, Rinkevich Y.  
Furnishing wound repair by the subcutaneous fascia.  
*Int J Mol Sci.* 2021;22 (16):9006.

Keswani, S. G., Balaji, S., Le, L., Leung, A., Lim, F. Y., Habli, M., et al.  
Pseudotyped adeno-associated viral vector tropism and transduction efficiencies in murine wound healing.  
*Wound Repair Regen.* 2012;20(4):592-600.

Kumar S, Mahendra G, Nagy TR, Ponnazhagan S.  
Osteogenic differentiation of recombinant adeno-associated virus 2-transduced murine mesenchymal stem cells and development of an immunocompetent mouse model for ex vivo osteoporosis gene therapy.  
*Hum Gene Ther.* 2004;15(12):1197-1206.

Kuzmin, D. A., Shutova, M. v., Johnston, N. R., Smith, O. P., Kukushkin, Y. S., et al.  
The clinical landscape for AAV gene therapies.  
*Nat Rev Drug Discov.* 2021;20(3):173-174.

Marshall CD, Hu MS, Leavitt T, Barnes LA, Lorenz HP, Longaker MT.  
Cutaneous Scarring: Basic Science, Current Treatments, and Future Directions.  
*Adv Wound Care (New Rochelle).* 2018;7(2):29-45.

Mcmahon, J. M., Conroy, S., Lyons, M., Greiser, U., O'Shea, C., Strappe, P., et al.  
Gene transfer into rat mesenchymal stem cells: a comparative study of viral and nonviral vectors.  
*Stem Cells Dev.* 2006;15(1):87-96.

Monstrey, S., Middelkoop, E., Vranckx, J. J., Bassetto, F., Ziegler, U. E., Meaume, S., et al.  
Updated scar management practical guidelines: non-invasive and invasive measures.  
*J Plast Reconstr Aesthet Surg.* 2014;67(8):1017-1025.

Myster SH, Cavallo R, Anderson CT, Fox DT, Peifer M.  
Drosophila p120catenin plays a supporting role in cell adhesion but is not an essential adherens junction component.  
*J Cell Biol.* 2003;160(3):433-449.

Ozaki C, Yoshioka M, Tominaga S, Osaka Y, Obata S, Suzuki ST.  
p120-Catenin is essential for N-cadherin-mediated formation of proper junctional structure, thereby establishing cell polarity in epithelial cells.  
*Cell Struct Funct.* 2010;35(2):81-94.

Pettitt J, Cox EA, Broadbent ID, Flett A, Hardin J.  
The *Caenorhabditis elegans* p120 catenin homologue, JAC-1, modulates cadherin-catenin function during epidermal morphogenesis.

J Cell Biol. 2003;162(1):15-22.

Ramesh P, Ye H, Dasgupta B, Machens H-G, Rinkevich Y.  
Visualizing Scar Development Using SCAD Assay - An Ex-situ Skin Scarring Assay.  
J. Vis. Exp. 2022;182:e63808.

Sen CK. Human Wounds and Its Burden: An Updated Compendium of Estimates.  
Adv Wound Care (New Rochelle). 2019;8(2):39-48.

Stender, S., Murphy, M., O'Brien, T., Stengaard, C., Ulrich-Vinther, M., Søballe, K., et al.  
Adeno-associated viral vector transduction of human mesenchymal stem cells.  
Eur Cell Mater. 2007;13:93-99.

Thoreson, M. A., Anastasiadis, P. Z., Daniel, J. M., Ireton, R. C., Wheelock, M. J., Johnson, K. R., Hummingbird, D. K., Reynolds, A. B.  
Selective uncoupling of p120(ctn) from E-cadherin disrupts strong adhesion.  
J Cell Biol. 2000;148:189-202.

Wan, L., Jiang, D., Correa-Gallegos, D., Ramesh, P., Zhao, J., Ye, H., et al.  
Connexin43 gap junction drives fascia mobilization and repair of deep skin wounds.  
Matrix Biol. 2021;97:58-71.

Wang D, Tai PWL, Gao G.  
Adeno-associated virus vector as a platform for gene therapy delivery.  
Nat Rev Drug Discov. 2019;18(5):358-378.

Yanagisawa M, Anastasiadis PZ.  
p120 catenin is essential for mesenchymal cadherin-mediated regulation of cell motility and invasiveness.  
J Cell Biol. 2006;174(7):1087-1096.

## FIGURE LEGENDS

**Figure 1. AAV8 transduces fascia fibroblasts.** (a) Representative confocal images show the comparison of several AAV serotypes with GFP transgene expression in skin fascia explants of C57BL/6 mice. Green: GFP Blue: DAPI. Scale bar, 100  $\mu$ m. (b) Quantification of the percentage of GFP<sup>+</sup> cells as a fraction of total cells in each group corresponding to a. Data is shown as mean  $\pm$  SD. The unpaired two-tailed t-tests were performed between AAV8 and other AAV serotypes, p-value \*\*p < 0.01, \*\*\*p < 0.001, n = 3. (c) C57BL/6J mice were transduced with the AAV8-GFP virus into the fascia. Mice were sacrificed at 3 days post-viral injection. Immunofluorescence images of GFP-positive cells expressing mesenchymal/fibroblast marker (Fsp1). pc, panniculus carnosus. The lower panel shows the high magnification images of the white boxes in the upper panel. Scale bars, 100  $\mu$ m.

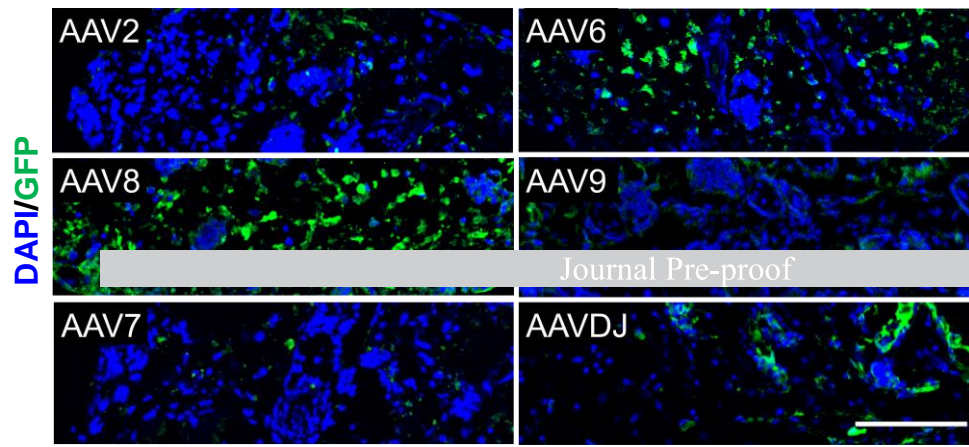
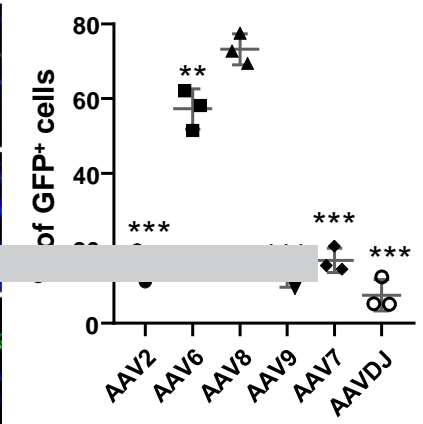
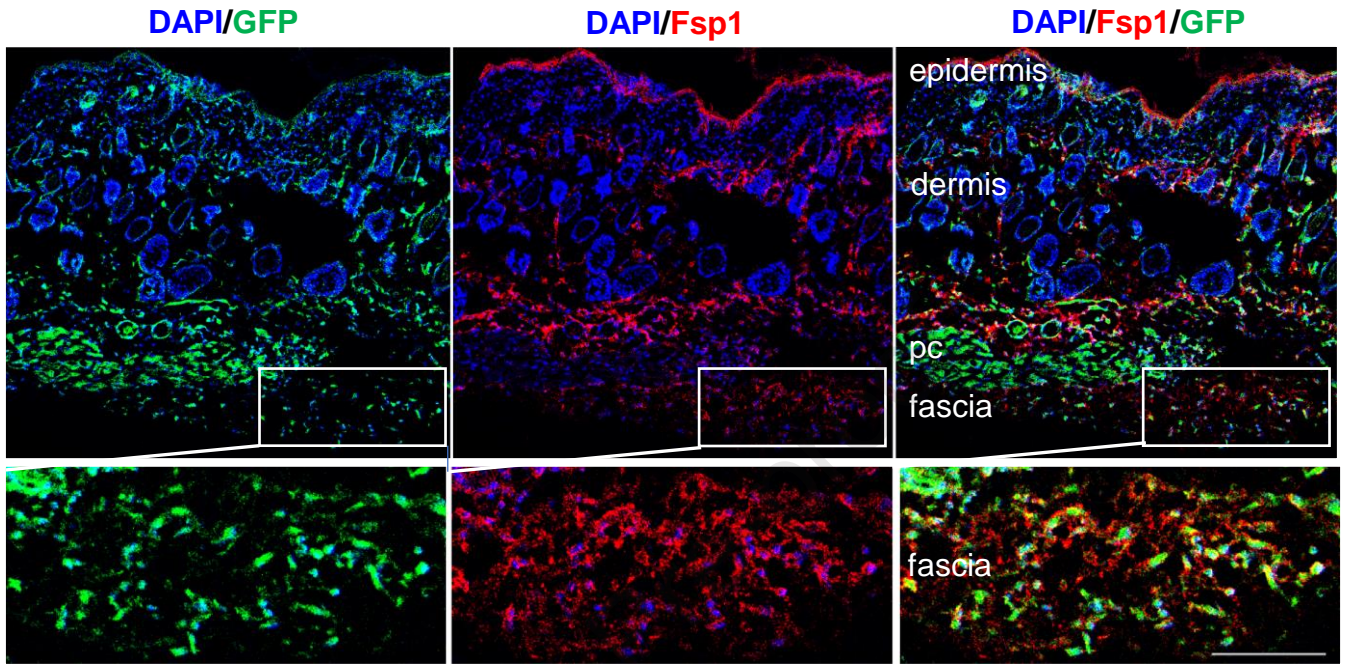
**Figure 2. AAV8 gene delivery into the fascia effectively targets the wound myofibroblasts.** (a) Histology shows GFP-expressing cells in uninjured skin (left) and 7dpw (right) and (b) percentage of GFP-expressing cells per high magnification field. Data are mean  $\pm$  SD, n = 6 images analysed from 3 biological replicates. Arrow heads indicate the border of wounds. wb, wound bed. (c) Immunolabelling of GFP-positive wound resident fibroblasts from 7dpw expressing myofibroblast marker ( $\alpha$ SMA) and fibroblast markers (CD26; ERTR7). (d) Percentage of GFP cells corresponding to c. Data are mean  $\pm$  SD, n = 5. (e) Experimental scheme and schematic depicting the AAV8 vector mediated Cre/Loxp recombination in the R26<sup>mT/mG</sup> mice allele, and the ex vivo imaging setup showing the imaging plane of wound bed and fascia. (f) Representative images of skin tissue from mT/mG mice treated with saline and AAV8-Cre virus. (g) Representative images of cross-section of wounds at 7dpw showing AAV8-Cre transduced cells in wound bed express myofibroblast marker  $\alpha$ SMA. wb, wound bed; pc, panniculus carnosus. Scale bars, 100  $\mu$ m.

**Figure 3. p120 expression is elevated in physiological wounds.** (a) Representative confocal images of p120 expression in the uninjured fascia, 3dpw and 7dpw of C57BL/6J mice. Arrow heads indicate the border of wounds. The lower panel shows the high magnification images of the white boxes in the upper panel. (b) Quantification of p120 fluorescence intensity corresponding to a. Data is mean  $\pm$  SEM. The student's t-test calculates the p-Value. \*\*\*\*p < 0.0001. n=5. (c) Immunolabelling of p120 expression at 7dpw from En1Cre;R26mTmG mice. pc, panniculus carnosus; wb, wound bed. Arrow heads indicate the border of wounds. The right panel shows the high magnification of the white box. (d) Experimental scheme of in vitro transduction and schematic representation of AAV Control ShRNA and AAV p120 ShRNA constructs. (e) Western blot image for validation of p120 knockdown after AAV8 mediated p120 ShRNA transduction in primary fibroblasts of fascia. (f) qRT-PCR analysis of p120 expression in primary fibroblasts with AAV8 expressing control ShRNA or p120 ShRNA. Data is mean  $\pm$  SD; n = 3 independent experiments. The student's t-test calculates the p-Value. \*\*p < 0.01.

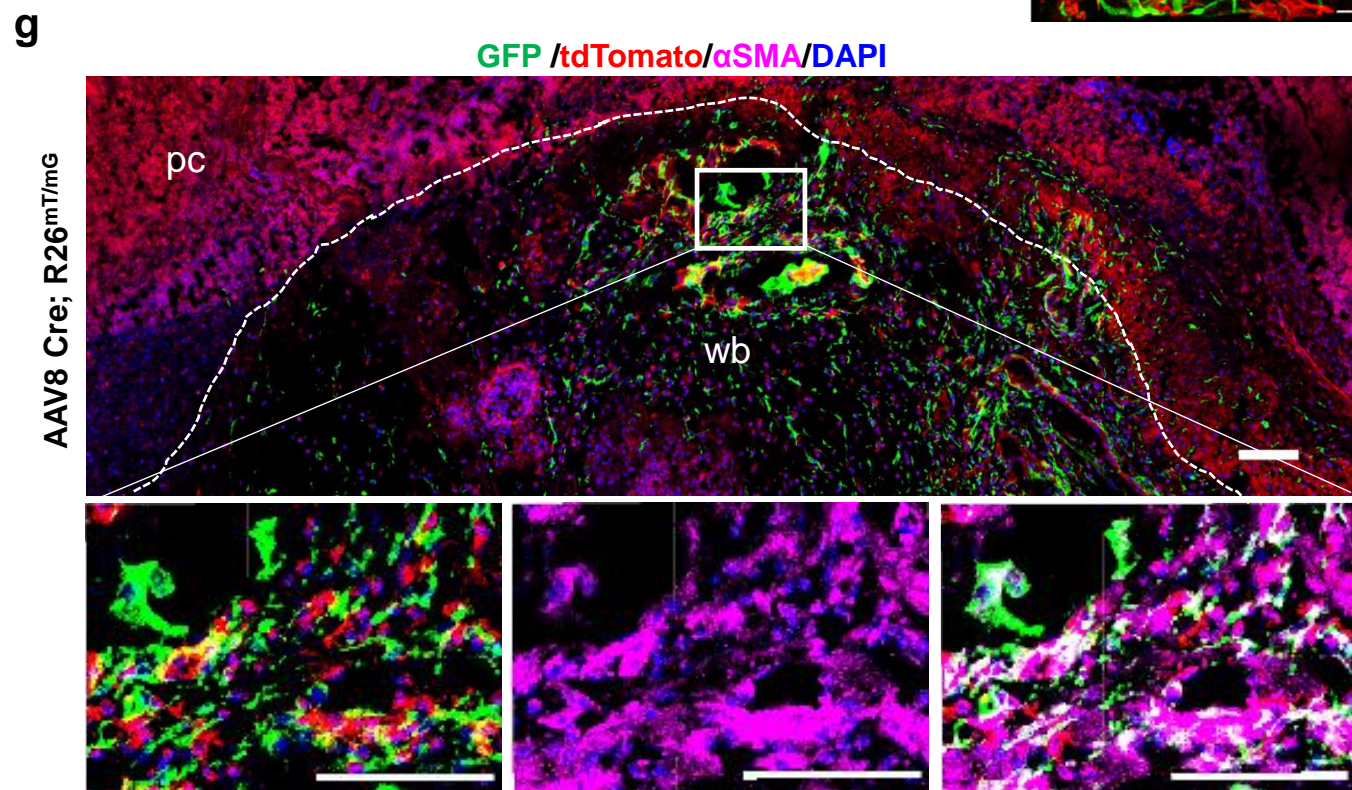
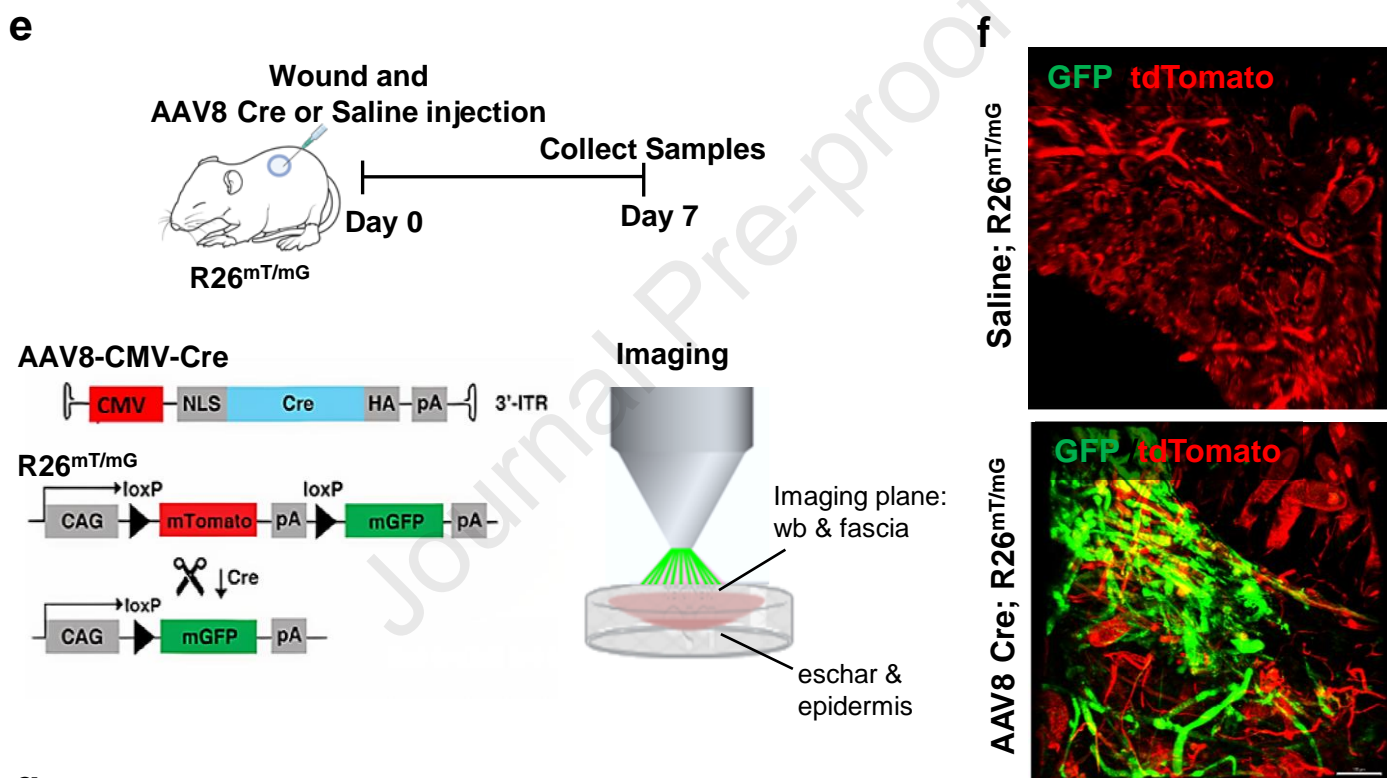
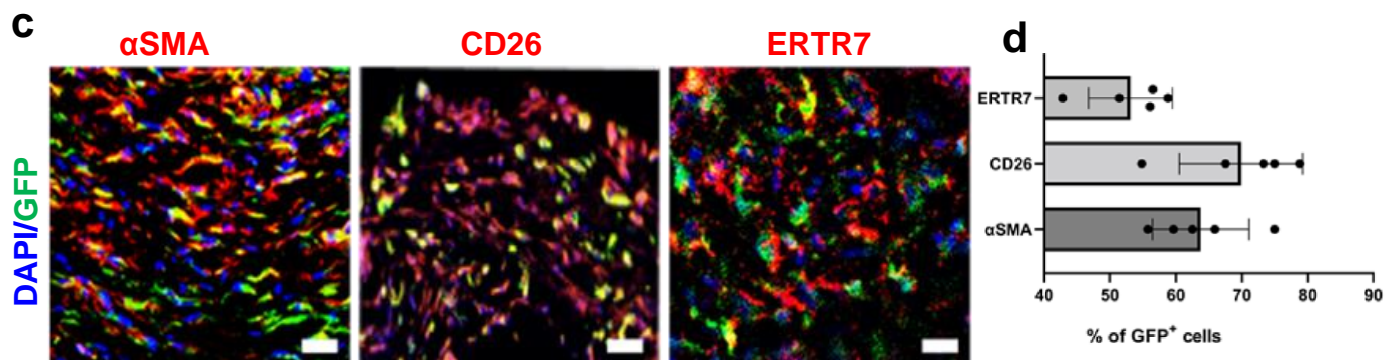
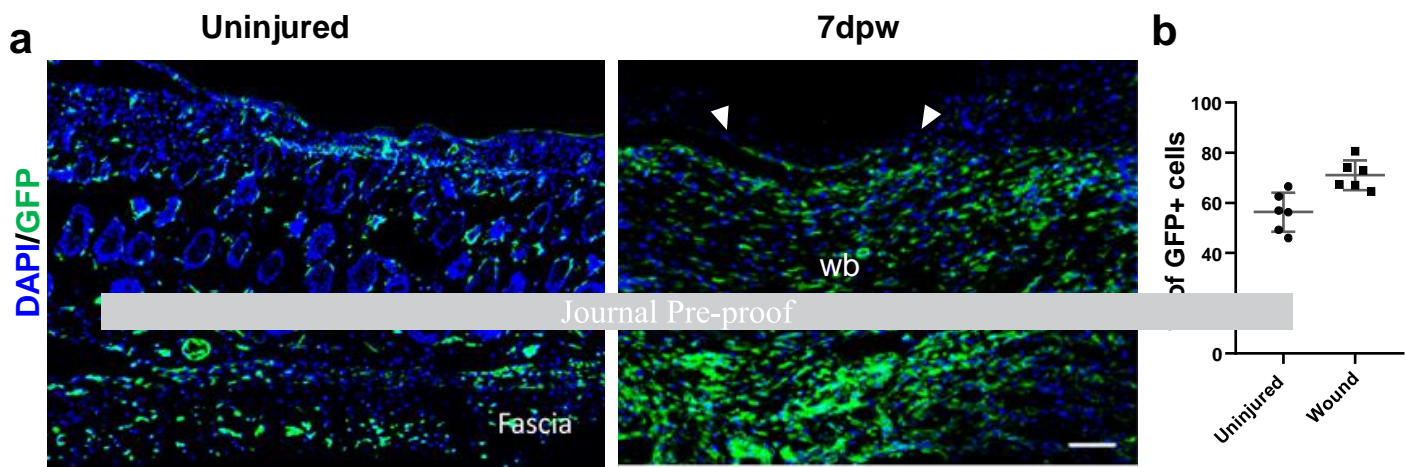
**Figure 4. AAV8-mediated shRNA silencing of p120 reduces the scarring.** (a) Representative confocal images of p120 expression in 7dpw from AAV8 Control ShRNA or AAV8 p120 ShRNA injected C57BL/6 mice. Arrow heads indicate the border of wounds. The right panel shows the high magnification of the white boxes. (b) Quantification of p120 intensity corresponding to a. Data is mean  $\pm$  SEM. The student's t-test calculates the p-Value. \*\*\*\*p < 0.0001. n = 5. (c) Representative images of myofibroblast marker  $\alpha$ SMA staining in the 7dpw of AAV8 Control ShRNA or AAV8 p120 shRNA injected C57BL/6J mice. The right panel shows the high magnification of the white boxes. (d) Quantification of  $\alpha$ SMA intensity corresponding to c. Data is mean  $\pm$  SEM. The student's t-test calculates the p-Value. \*\*\*p < 0.001. n = 5. (e) Representative images of collagen I+III+IV staining in the 7dpw of

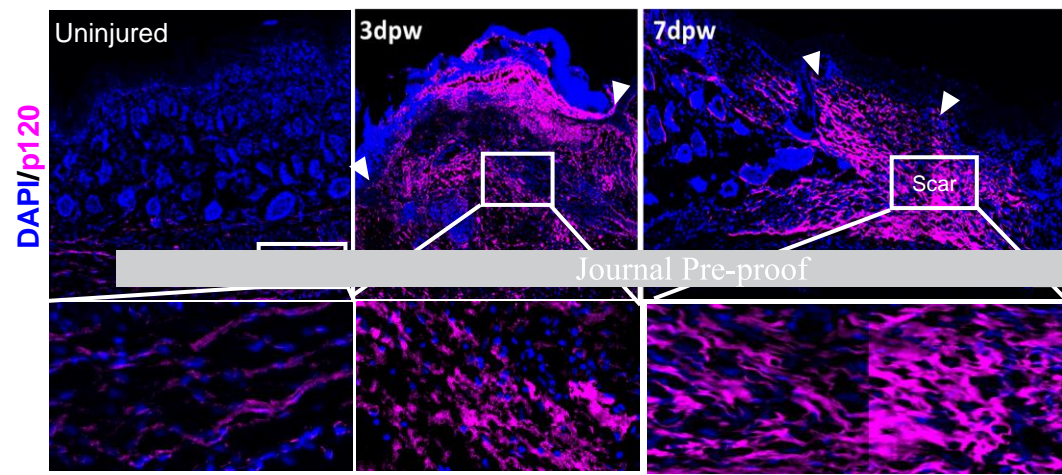
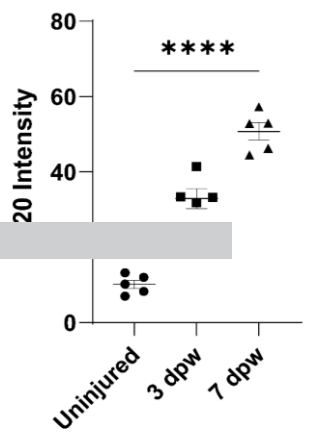
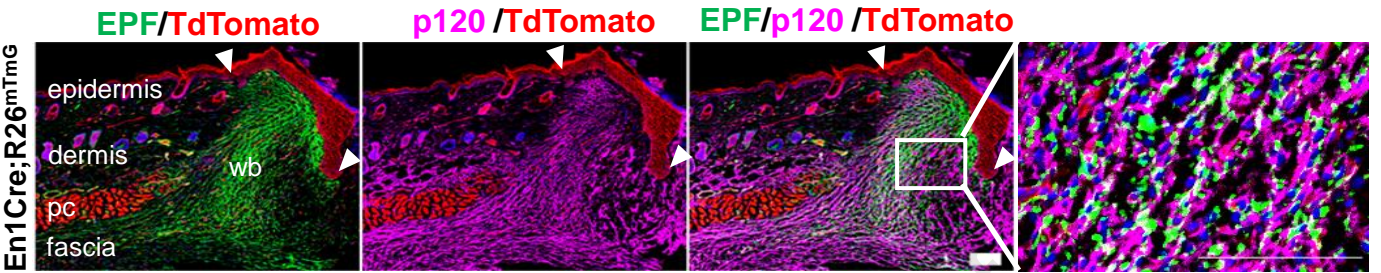
AAV8 Control ShRNA or AAV8 P120 ShRNA injected C57BL/6J mice. The right panel shows the high magnification of the white boxes. (f) Quantification of collagen I +III+VI intensity corresponding to e. Data is mean  $\pm$  SEM. The student's t-test calculates the p-Value. \*\*\*\*p < 0.0001. n = 5. (g) Masson's trichrome stained 7dpw of AAV8 Control ShRNA or AAV8 p120 ShRNA injected C57BL/6J mice. dotted lines indicate the scar area. (h) Quantification analysis of scar area in g. Data is mean  $\pm$  SEM. The student's t-test calculates the p-Value. \*\*\*p < 0.001. n = 5.

**Figure 5. AAV mediated silencing of p120 prevents ECM mobilization.** (a) live imaging representing the morphology of wound resident fibroblasts in response to AAV8 control shRNA, and AAV8 p120 shRNA transduction are visualized with GFP. (b) Quantification of protrusion length of the transduced cells. Error bars show the SEM. (c) Schematic representation of transduced cell clusters. (d) Quantification of the number of the secondary branches of intercellular junctions. (e) Particle image velocimetry (PIV) analysis of the movement pattern of transduced cells of the last imaging frame. The colored scale bar indicates migratory speeds from slow (blue) to fast (red). Scale bar unit: pixel. (f) Quantification of the displacement of all transduced cells in the last frame compared to the first frame of the live imaging videos. (g) Experimental scheme of matrix labelling with AAV Control ShRNA or AAV p120 ShRNA injection after injury in C57BL/6 mice. (h) Images show NHS ester labelled matrix in 7dpw. Labeled fascia matrix in green and autofluorescence in red. The lower panel shows the high magnification images of the white boxes in the upper panel. (i) Percentage of labelled fascia matrix coverage in g. Data is Mean  $\pm$  SEM, n = 6 sections from 3 independent experiments. unpaired two-tail Student's t-test, \*\*\*\*p < 0.001.

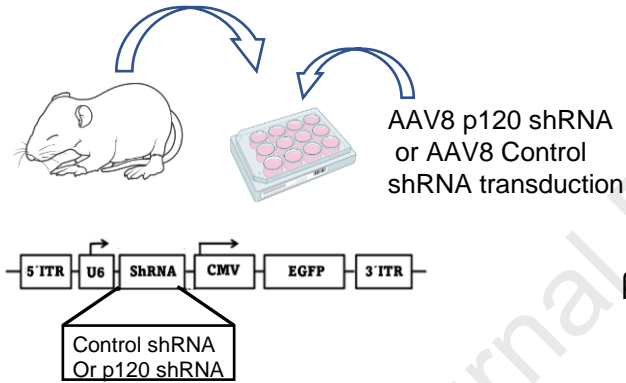
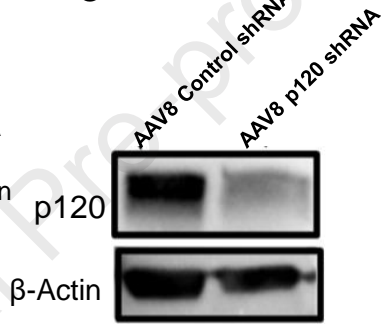
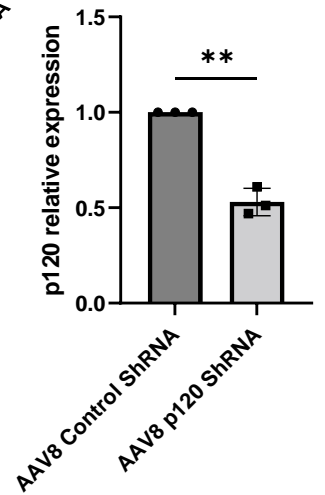
**a****b****c**

Journal Pre-proof

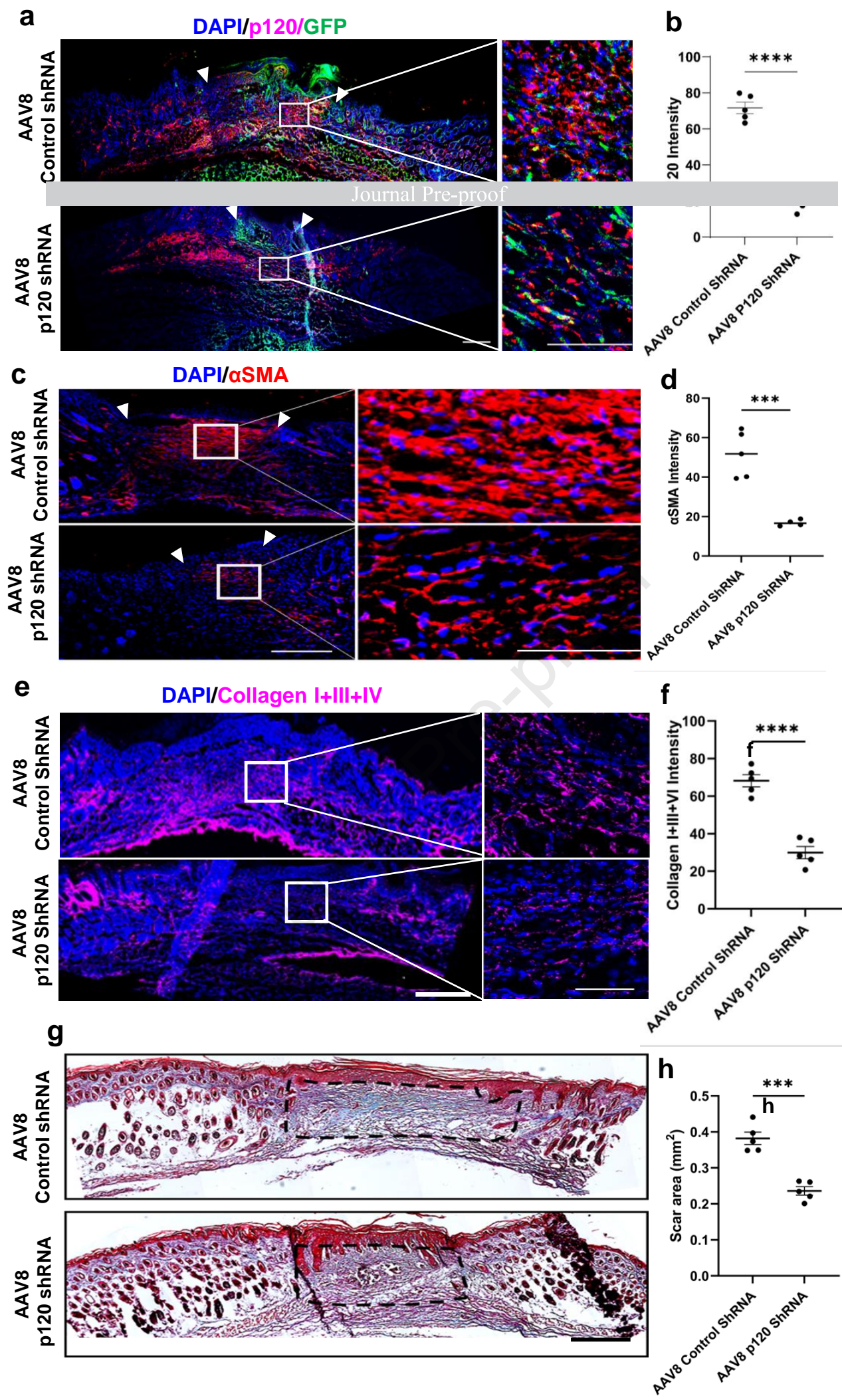


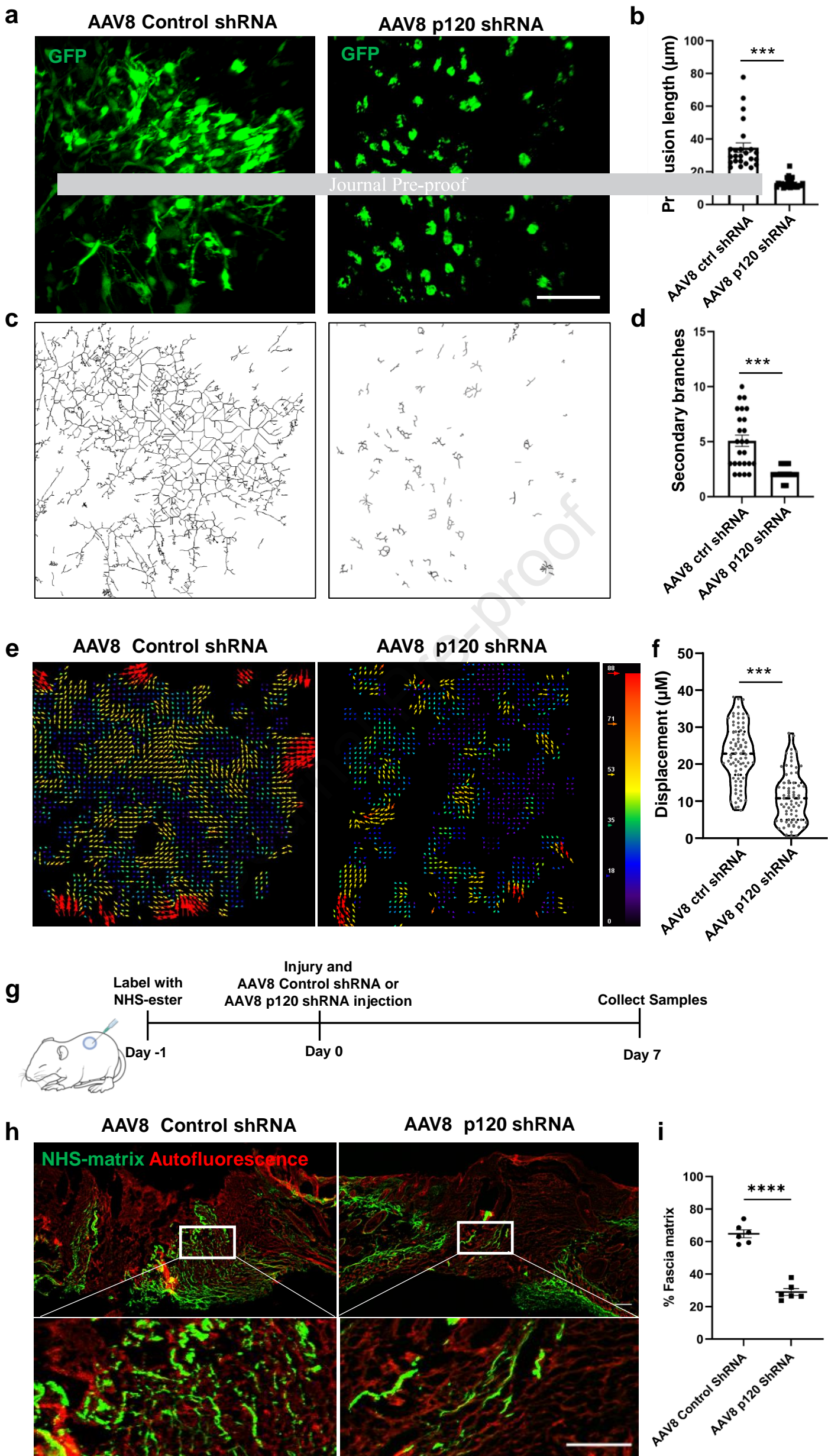
**a****b****c****d**

Primary fascia fibroblasts isolation

**e****f**







**SUPPLEMENTARY****Supplementary Figure Legends**

**Supplementary Figure 1. Cell type of AAV8 transduced cells.** Cryo-sections from AAV8-GFP transduced wounds 7 days post-wounding were immunostained with epidermal marker CK14 (a), endothelial marker CD31 (b), immune cell marker CD45 (c), pan fibroblast cell marker PDGFR $\alpha$  (d), and fascia fibroblast marker N-cadherin (e) and Sca1 (f), respectively. In the left panel, the dotted lines indicate the border of wounds, and white boxes indicate the regions showed in higher magnification in the right panel. Scale bars: left panel = 200  $\mu$ m; right panel = 50  $\mu$ m. (g) Quantification the percentage of each cell type that was transduced by AAV8-GFP in total transduced cells in wound bed and wound margin.

**Supplementary Figure 2. Expression of p120 and effects of p120 knockdown in wounds.**

(a) immunofluorescence staining of p120 in wounds of 7 dpw and 21 dpw from En1<sup>Cre</sup>;R26<sup>mTmG</sup> mice. (b) quantification of p120 expression in 7 dpw and 21 dpw as fluorescence intensity unit. (c) immunofluorescence staining of N-cadherin in AAV8 control shRNA and AAV8 p120 shRNA injected wounds. (d) quantification of N-cadherin expression as fluorescence intensity unit. (e) immunofluorescence staining of CD45 in AAV8 control shRNA and AAV8 p120 shRNA injected wounds. (f) quantification of percentage of wound infiltrating CD45<sup>+</sup> cells in total cells. (g) immunofluorescence staining of active Caspase 3 in AAV8 control shRNA and AAV8 p120 shRNA injected wounds. (f) quantification of percentage of Caspase 3<sup>+</sup> cells in total cells in wounds. Arrow heads indicate the border of wounds. dpw, days post-wounding; FIU, fluorescence intensity unit. Data are mean  $\pm$  SD. \*\*\* p<0.001, with unpaired two-tailed t-test. Scale bar = 200  $\mu$ m.

## **Supplementary Materials and Methods**

### **Tissue fixation and cryosections**

The skin and wound tissue was fixed overnight with 2% paraformaldehyde (PFA) at 4 °C. Following the removal of PFA, samples were rinsed in PBS three times for a total of 5 minutes each, and immersed in 30% sucrose overnight. The fixed wound tissue was cut into two halves in the middle, and embedded in Tissue-Tek® O.C.T medium for snap frozen on dry ice. The cryosections at the thickness of 10 µm were generated from the middle of the wounds. Each 10 µm cut was followed 30 µm trim. Five continuous sections were collected, and the average was calculated.

### **Immunofluorescence staining**

Cryosections were fixed with ice-cold acetone for 5 minutes and gently washed the slides 3X in PBS. Overlay the tissue section with a blocking solution. Incubate the slides in a humidified chamber at RT for 1 hr. After that, slices were overlaid with a primary antibody with recommended dilution in blocking solution overnight at 4°C. The next day, gently wash the slides 3X in PBS (5 min/wash). Overlay the tissue sections with secondary antibody diluted in blocking solution. Incubate the slides in a humidified chamber for 1 hr. at room temperature. Gently wash the slides 3X in PBS (5 min/wash) and stain with DAPI solution (1:5000 dilution in PBS) for 5 min. Gently blot the slide with absorbent paper to remove excess liquid. FluoromountG™ Mounting Medium (Invitrogen) was used for Mounting the slides. The mounted slides were imaged using a confocal laser scanning microscope (Zeiss LSM710).

### **Masson's trichrome staining**

Fix the slides by immersion in precooled cold acetone (-20°C) for 5 min. Incubate the tissue slides with Bouin's solution (Sigma-Aldrich HT10132) at RT overnight. After washing the slides for 2 minutes with cold tap water, they are stained for 10 minutes with iron Hematoxylin solution (Sigma-Aldrich HT1079). Discard the Hematoxylin solution. Wash the slides with

running tap water for 10 minutes. Following that, rinse the slides with distilled water for 2 minutes. Incubate the Slides for 5 minutes with Biebrich Scarlet-Acid solution. Wash the slides with 3X distilled water (1min/wash). Incubate the slides with Phosphotungstic /Phosphomolybdic Acid Solution for 10 minutes in the glass chamber and directly incubate the slides with Aniline Blue solution for 10 minutes. Wash the slides with 3X distilled water for 1 minute each. Further, incubate the slides with Glacial acetic acid (1%) for 2 minutes and wash the slides with 2X distilled water for 1 minute each. Post staining, the tissue slides were dehydrated with 70% ethanol for 3 minutes - 90% ethanol for 3 minutes and 100% ethanol for 3 minutes. Finally, keep the slides in Xylol for 5 minutes. After dehydration, the slides were mounted with 2-3 drops of ROTI®Mount media. Images were acquired using the Zeiss Axio imager with 20X magnification. The stained structure in the slides represents the following, Nuclei- Black, Cytoplasm-Red and Collagen in Blue.

### **ShRNA design and plasmid construction**

AAV U6-p120-ShRNA and AAV U6-Control ShRNA plasmids were constructed and purchased from Vector Biolabs (Malvern, PA). To knock down the p120 expression, a distinct ShRNA sequence targeting mouse (5'CGAGGCTATGAACTCTTATTTCTCGAGAAAT AAGAGTTCATAGCCTCG3') and a scrambled ShRNA sequence (5'CCTAAGGTTAAGTC GCCCTCGCTCGAGCGAGGGCGACTTAACCTTAGG3') was designed using Vector Biolabs (Malvern, PA). U6 promoter was used to drive p120 ShRNA or scrambled ShRNA expression followed by green fluorescent protein (GFP) separately driven by a CMV promoter.

### **Adeno-associated virus (AAV) production**

Replication-incompetent AAV was packaged via triple transfections of the AAV transgene plasmid (AAV p120 ShRNA-GFP, AAV Control ShRNA-GFP, AAV Cre, AAV-GFP), pRC8

encoding Rep and cap proteins and helper plasmids into AAVpro 293 T cell line (Takara Bio, cat. no. 632273). The cells should reach the confluence of 75%-80% on the day of transfection. Prepare a 1:1:1 molar ratio of triple plasmids (pRC6, helper plasmids and AAV transgene plasmids). The total DNA is calculated based on 0.5 $\mu$ g of DNA/cm<sup>2</sup> of cell culture surface area. The volume of Polyethyleneimine (PEI) was used based on 4:1 ratio of PEI (ug): total DNA (ug). Four-day post-transfection, AAV viruses were extracted according to the AAVpro® Purification Kit (Takara. Cat. #6232) procedures. AAVpro® Titration Kit was utilized to measure the genomic titer of AAV stock.

### ***Ex vivo skin tissue culture***

Back-skin was collected from newborn (postnatal day 0-1) C57BL/6J and washed twice with cold DMEM/F-12 (Thermo Fisher Scientific 11320074) medium to remove contaminating blood, and then washed once with Hank's Balanced Salt Solution (HBSS, Thermo Fisher Scientific 14175095). After careful removal of ventral non-skin tissue with a surgical scalpel, round skin pieces were cut out with a disposable  $\varnothing$  2 mm biopsy punch (Stiefel 270130) down to below the panniculus carnosus muscle and cultured in 200  $\mu$ l of DMEM/F-12 medium containing 10% FBS, 1x GlutaMAX (Thermo 338 Fisher Scientific 35050038), 1x Penicillin/streptomycin (Thermo Fisher Scientific 339 15140122), and 1x MEM non-essential amino acids (Thermo Fisher Scientific 11140035) in 96-well plates, in a humidified 37°C, 5% CO<sub>2</sub> incubator. (Note: the 2 mm skin pieces were cultured submerged in medium with fascia side face up). After 2 hrs of culture, the skin explants were exposed to  $5 \times 10^{10}$  GC AAV for 24 h, and a fresh medium was supplied every other day. The skin tissues were harvested after 72 hrs. The tissue samples were fixed in 2% PFA overnight at 4°C. After washing in PBS, the tissues were embedded and frozen in an optimal cutting temperature compound, and 6  $\mu$ m cryo-sections were prepared with a cryostat.

***In vitro* transduction assay for p120 knockdown**

Primary fibroblasts from fascia were obtained from neonatal (P0-P4) back skin tissue. Fascia layers were minced with scalpels in a 10cm dish. The tissue fragments were transferred into a centrifuge tube containing collagenase (1000U/mL) final concentration. Incubate the tube at 37°C for 30 minutes and swirl the tubes every 5 minutes centrifuge at 200 x g for 10 min. Remove the supernatant and resuspend the pellet with 2 ml of HBSS medium. Centrifuge the cell suspension again at 200 × g for 5 minutes and 0.5ml of 0.05 % trypsin, swirl the tube vigorously and place the tube for 30 min at 37°C. Then centrifuge the cell suspension at 200 × g for 5 minutes and discard the resuspend. Resuspend the cell pellet with 2 ml of fibroblast culture medium. The cell suspension was filtered with a 70µm cell strainer. Transfer the cells to a 10 cm cell culture dish and 10 ml of culture medium. Incubate the cells at 37°C, CO<sub>2</sub> at 5%, and 95 % relative humidity in an incubator. Approximately 1 × 10<sup>5</sup> primary fibroblasts were used for transductions with AAV8 Control ShRNA or AAV8 p120 ShRNA virus in 12-well plates and harvested after 4 days for the western blot and qPCR analysis.

**Western blot analysis**

Cells were directly lysed using RIPA buffer (Sigma-Aldrich, UK) supplemented with a phosphatase inhibitor cocktail (Protease Inhibitor Cocktail Set III, EDTA-Free, Calbiochem, UK (1:200 dilution)). With the BSA protein assay kit, the protein concentration was determined. All assays were performed using a total of 30µg of protein. Proteins were separated on Invitrogen™ NuPAGE™ 4 to 2% Mini gels using an electrophoresis technique described by the manufacturer (running conditions 200V and 135 mA). Proteins were blotted onto polyvinylidene difluoride membranes (PVDF) from polyacrylamide gels. The membranes were

kept with a specific anti-p120 antibody (and developed using an ECL™ detection kit. p120 protein bands were visualized using a chemiluminescent imaging system such as a ChemiDoc in a dark room.  $\beta$ -actin was used as a loading control.

### **Quantitative RT-PCR (qPCR) analysis**

Qiagen RNeasy Mini-Kit to extract the RNA from AAV transduced primary fibroblasts and Verso Reverse Transcriptase (Invitrogen) was utilised for cDNA synthesis. Quantitative RT-PCR procedures were carried out using a LightCycler® 480 II platform (Roche Diagnostics). Relative mRNA expression was then calculated using comparative methods ( $2^{-\Delta\Delta C_T}$ ) using RPL-13A as a reference gene. Following p120 primer sequences were used, forward primer (5'CTGTGATGGTGTTCCTGCTCTG3') and reverse primer (5'TGGGATGAGAGATTC CA CAGGG 3')



---

## 4. Paper II

### **Wound infiltrating adipocytes are not myofibroblasts**

Shruthi Kalgudde Gopal<sup>1,2,#</sup>, Ruoxuan Dai<sup>1,#</sup>, Ania Maria Stefanska<sup>1</sup>, Meshal Ansari<sup>2,3</sup>, Jiakuan Zhao<sup>1</sup>, Pushkar Ramesh<sup>1</sup>, Johannes W. Bagnoli<sup>4</sup>, Donovan Correa-Gallegos<sup>1</sup>, Yue Lin<sup>1</sup>, Simon Christ<sup>1</sup>, Ilias Angelidis<sup>2</sup>, Valerio Lupperger<sup>3</sup>, Carsten Marr<sup>3</sup>, Lindsay C. Davies<sup>5</sup>, Wolfgang Enard<sup>4</sup>, Hans-Günther Machens<sup>6</sup>, Herbert B. Schiller<sup>2,\*</sup>, Dongsheng Jiang<sup>1,\*</sup>, and Yuval Rinkevich<sup>1,\*</sup>

1 **Wound infiltrating adipocytes are not myofibroblasts**

2 Shruthi Kalgudde Gopal<sup>1,2,#</sup>, Ruoxuan Dai<sup>1,#</sup>, Ania Maria Stefanska<sup>1</sup>, Meshal Ansari<sup>2,3</sup>,  
3 Jiakuan Zhao<sup>1</sup>, Pushkar Ramesh<sup>1</sup>, Johannes W. Bagnoli<sup>4</sup>, Donovan Correa-Gallegos<sup>1</sup>, Yue  
4 Lin<sup>1</sup>, Simon Christ<sup>1</sup>, Ilias Angelidis<sup>2</sup>, Valerio Lupperger<sup>3</sup>, Carsten Marr<sup>3</sup>, Lindsay C. Davies<sup>5</sup>,  
5 Wolfgang Enard<sup>4</sup>, Hans-Günther Machens<sup>6</sup>, Herbert B. Schiller<sup>2,\*</sup>, Dongsheng Jiang<sup>1,\*</sup>, and  
6 Yuval Rinkevich<sup>1,\*</sup>

7

8 <sup>1</sup> Institute of Regenerative Biology and Medicine, Helmholtz Center Munich, Munich, Germany

9 <sup>2</sup> Institute of Lung Health and Immunity, Helmholtz Center Munich, Munich, Germany

10 <sup>3</sup> Institute of AI for Health, Helmholtz Center Munich, Munich, Germany

11 <sup>4</sup> Anthropology and Human Genomics, Faculty of Biology, Ludwig-Maximilian University  
12 Munich, Germany.

13 <sup>5</sup> **Department of Microbiology, Tumour and Cell Biology (MTC)**, Karolinska Institute,  
14 Stockholm, Sweden

15 <sup>6</sup> Department of Plastic and Hand Surgery, Klinikum rechts der Isar, School of Medicine,  
16 Technical University of Munich, Munich, Germany

17

18 # These authors contributed equally

19

20 \* Correspondence to: [herbert.schiller@helmholtz-munich.de](mailto:herbert.schiller@helmholtz-munich.de) (H.B.S.),  
21 [dongsheng.jiang@helmholtz-munich.de](mailto:dongsheng.jiang@helmholtz-munich.de) (D.J.) & [yuval.rinkevich@helmholtz-munich.de](mailto:yuval.rinkevich@helmholtz-munich.de)  
22 (Y.R.)

23

24

25 **Abstract**

26 The origins of wound myofibroblasts and scar tissue remains unclear, but it is assumed to  
27 involve conversion of adipocytes into myofibroblasts. Here, we directly explore the potential  
28 plasticity of adipocytes and fibroblasts after skin injury. Using genetic lineage tracing and live  
29 imaging in explants and in wounded animals, we observe that injury induces a transient  
30 migratory state in adipocytes with vastly distinct cell migration patterns and behaviours from  
31 fibroblasts. Furthermore, migratory adipocytes, do not contribute to scar formation and remain  
32 non-fibrogenic *in vitro*, *in vivo* and upon transplantation into wounds in animals. Using single-  
33 cell and bulk transcriptomics we confirm that wound adipocytes do not convert into fibrogenic  
34 myofibroblasts. In summary, the injury-induced migratory adipocytes remain lineage-restricted  
35 and do not converge or reprogram into a fibrosing phenotype. These findings broadly impact  
36 basic and translational strategies in the regenerative medicine field, including clinical  
37 interventions for wound repair, diabetes, and fibrotic pathologies.

38

39

40 **Introduction**

41 Cells undergo a gradual stepwise restrictive specification during embryonic development,  
42 acquiring lineage-specific differentiation fates to become specialized adult cell types. This  
43 gradual segregation of cellular potential during development is thought to be restrictive and  
44 maintained into, and throughout, adulthood<sup>1</sup>. However, many studies have challenged this  
45 notion, and called lineage-restriction into question, by proposing that fully committed cells can  
46 respond to tissue challenges, such as injury, disease or aging, by acquiring new fates. This  
47 phenotypic adaptability is termed plasticity.

48 The prototypical example of plasticity is the terminally differentiated stromal mesenchymal  
49 cell<sup>2</sup>. Mesenchyme includes mature adipocytes and fibroblasts, which have been proposed to  
50 cross-convert between lineages in response to tissue challenges, in skin and in internal organs  
51 of both mice and humans<sup>3-11</sup>. The impact of lineage interplay between adipocytes and  
52 fibroblasts is evident clinically in numerous disorders including diabetes, where complications  
53 associated with the disease include chronic wound healing and fibrotic pathologies such as renal  
54 disease and diabetic retinopathy<sup>12</sup>.

55 Lineage interplay between adipocytes and fibroblasts is also evident in fibrotic induction,  
56 irrespective of organ. Loss of dermal adipose tissue and adipogenicity in favour of expanding  
57 stromal fibroblasts responsible for ECM deposition are consistent features of fibrosis in both  
58 mice and men. This is exemplified in skin biopsies from patients with systemic sclerosis<sup>13</sup>.  
59 Similar imbalances in the adipocyte : fibroblast stromal environment are seen in obese or  
60 diabetic patients undergoing fibro-inflammation in their adipose tissue, where adipocyte  
61 numbers decrease in favour of fibroblasts, a transition that is associated with fibrosis and scar  
62 formation within the connective tissues<sup>14, 15</sup>.

63 The relevance of changing cellular ratios and phenotypes of fibroblasts and adipocytes within  
64 organ systems extends far beyond diabetes and fibrotic disease however. Increased frailty and  
65 deterioration in organ function have been directly linked to changes in adipose and fibroblast

66 communities with age<sup>16, 17</sup>. There is a clear need for further delineation of each cell lineage's  
67 role in tissue homeostasis and repair.

68 Three main hypotheses have been proposed as to how cells may transition between lineages:  
69 de-differentiation (and re-differentiation), (direct) trans-differentiation and heterotypic cell  
70 fusion<sup>18</sup>. (i) De-differentiation is where a cell loses its lineage-specific differentiation state and  
71 reverses into a more immature cellular state, sometimes associated with a multi-lineage  
72 differentiation potential, as seen in adult stem/progenitor cells. (ii) Trans-differentiation is the  
73 transition from one lineage to another either directly or indirectly i.e. de-differentiation  
74 followed by subsequent re-differentiation. (iii) The third conversion mechanism, heterotypic  
75 cell fusion, involves merging of two terminally differentiated and functionally distinct cell  
76 types. This form of fusion results in the formation of a hybrid cell with the combined functions  
77 of both precursor cells, and has been shown to occur in low frequency during injury<sup>19</sup>.

78 Most reported observations of interchangeability between fibroblasts and adipocytes have been  
79 based on one cell type acquiring markers associated with the other, e.g. fibroblasts expressing  
80 Perilipin-1 (*Plin1*), or adipocytes expressing alpha smooth muscle actin (*Acta2*). However,  
81 these markers are insufficient to establish the identity categorically<sup>20, 21</sup>. Designating plasticity  
82 has equally relied on morphological changes, for example between round and lipidated  
83 adipocytes to flat bipolar fibroblasts. However, phenotype can also be deceptive, as mature  
84 adult adipocytes can shed their lipid content under certain metabolic conditions making them  
85 even harder to distinguish from fibroblasts. Such fluidity in the homeostatic properties of  
86 adipocytes means that a more in-depth characterization of the molecular and cytostructural  
87 changes involved in response to injury is needed to definitively demonstrate cellular plasticity.  
88 Cellular identity is not just a construct of markers and morphology. Formal proof of  
89 physiological plasticity requires the observation of a defined mature cell losing its cellular  
90 identity and functions, and metamorphosing into a distinctly different cellular identity with new  
91 functions. Such changes are, in the main, inherently achieved through transcriptional regulation,

92 characterized by the loss of mature differentiation markers (as for de-differentiation), the  
93 expression of immature cell markers and acquisition of a new transcriptional landscape (as for  
94 trans-differentiation), supporting the attainment of these new functional properties<sup>22</sup>.

95 Here, we directly explore the plasticity of fibroblasts and white adipocytes in skin by closely  
96 analysing various transcriptomic, phenotypic, and functional criteria across these two cellular  
97 lineages. Using a combination of genetic lineage-tracing strategies, single-cell transcriptomics,  
98 live-cell imaging and tracking, transplantation assays and *in vivo* injury models, we study  
99 stepwise transcriptional and functional responses in mature adipocytes and fibroblasts after skin  
100 injury. We conclude that adipocytes remain lineage-restricted in response to tissue injury, and  
101 do not dedifferentiate, fuse with, or convert to myofibroblasts. Adipocytes respond to wounding  
102 stimuli, experience shifts in their motility and functionality, and play active but distinct roles  
103 from fibroblasts in the endogenous tissue healing response.

104

105

## 106 **Results**

107

### 108 **Adipocytes retain their cell lineage identities in a skin explant model**

109 To address a potential phenotypic convergence of adipocyte and fibroblast lineages we  
110 performed single-cell RNA-seq (scRNA-seq) experiments. To track fibroblasts in the back-  
111 skin, we employed an *En1*<sup>Cre</sup> reporter that labels dermal fibroblasts, and to a small extent  
112 adipocytes. The vast majority of *En1*-lineage cells termed Engrailed-lineage positive fibroblasts  
113 (EPFs) have been demonstrated to be the fibrogenic cell lineage responsible for scar formation  
114 in the back-skin<sup>23-25</sup>. Mature adipocytes were selectively tracked using an adiponectin lineage-  
115 specific reporter (*Adipoq*<sup>Cre</sup>), a hormone involved in regulating glucose levels and fatty acid  
116 breakdown, and a key biomolecule for anti-diabetic clinical interventions<sup>26</sup>. The two lineage-  
117 specific transgenic lines were individually crossed to a double-colour fluorescent reporter  
118 (*R26*<sup>mTmG</sup>), thereby marking mature adipocytes and fibrogenic cells with membrane-bound  
119 green fluorescent protein (GFP) in two separate transgenic reporter mice (Supplementary Fig.

120 1a). Skin explants were harvested from both adipocyte ( $\text{Adipoq}^{\text{Cre}};\text{R26}^{\text{mTmG}}$ ) and fibroblast  
121 ( $\text{En1}^{\text{Cre}};\text{R26}^{\text{mTmG}}$ ) double-transgenic reporter mice, cultured for up to 5 days, followed by  
122 purification of adipocytes and fibroblasts for scRNA-seq (Fig. 1a)<sup>27-29</sup>.

123 In two-dimensional uniform manifold approximation and projection (UMAP) embeddings of  
124 the single-cell transcriptomes, the two lineages largely separated but with partial overlap (Fig.  
125 1b). The overlap was mostly observed on day 4 after culture (Fig. 1c). To characterize the  
126 heterogeneity of cell states within the two lineage-labelled populations of single cells we used  
127 Louvain clustering analysis. Engrailed marks a very early embryonic population of cells in the  
128 dermomyotome, primarily of fibroblasts but also a subset of adipocyte progenitors (APs).  
129 Indeed, two clusters of APs (cluster 1 and 9) were identified in the  $\text{En1}$ -lineage population  
130 (Supplementary Fig. 1b, c) in neonatal skin of the explant model. They were excluded in the  
131 analyses to enable mature adipocytes alone to be studied for potential cellular conversion into  
132 fibroblasts. We observed six distinct sub-clusters of cells in each of the  $\text{Adipoq}^{\text{Cre}}$  and the  $\text{En1}^{\text{Cre}}$   
133 lineages (Fig. 1, Supplementary Fig. 1d, e). All twelve cluster identities have highly distinct  
134 marker genes and distinct enriched gene categories (Supplementary Fig. 1h, Supplementary  
135 Table 1). Next, we used Pearson's correlation co-efficiency and measured the magnitude of  
136 relationships between the twelve clusters (Fig. 1d). This analysis indicated that the twelve  
137 clusters did not overlap, or converge, and remained separate. Despite signature variability  
138 within lineages, the two lineages stayed distinct and clustered apart under all experimental  
139 conditions.

140 These data indicated that adipocyte and fibroblast lineage signatures are not lost in the explants  
141 that mimic wounding and scarring. We identified a core set of 88 definitive adipocyte genes  
142 and 198 definitive fibroblast genes that remained specific to both lineages in the explants (Fig.  
143 1e, Supplementary Fig. 1i, Supplementary Table 2). Gene ontology (GO) gene set enrichment  
144 analysis confirmed that the core set of adipocyte genes was significantly enriched for terms

145 such as “fat cell differentiation” and “lipid metabolism” (Fig. 1f), while the fibroblast core gene  
146 set was significantly enriched for extracellular matrix genes (Fig. 1g). To further address this  
147 lineage restriction at the pathway level, we scored transcriptomic signatures of both adipocytes  
148 and fibroblasts against a selected set of pathway gene lists taken from the RT<sup>2</sup> profiler PCR  
149 array (n=84). We found that fibroblast signatures were enriched for fibrogenically active  
150 pathways like ECM and adhesion molecules, fibrosis, wound healing, focal adhesions, etc.  
151 Whereas, adipocytes were enriched for adipogenic pathways such as fatty acid metabolism,  
152 Lipoprotein signalling and cholesterol metabolism (*Lscm*), Peroxisome proliferator-activated  
153 receptor gamma (*Pparγ*) targets etc.

154 The adipocyte core signature contained genes such as Pyruvate dehydrogenase lipoamide  
155 kinase isozyme 4 (*Pdk4*), a gene involved in reactive oxygen species (ROS) production, which  
156 has a vital role acting as a second messenger recruiting immune cells, as well as defensive  
157 against invading bacteria at the site of injury<sup>30, 31</sup>. Core adipocyte markers also included  
158 Orosomucoid 1 (*Orm1*) known to be immunomodulatory, Stearoyl Coa desaturase 1 (*Scd1*)  
159 which is involved in fatty acid biogenesis and Serum amyloid A 3 (*Saa3*), which is responsible  
160 for acute phase response and is induced by pro-inflammatory stimuli<sup>32</sup>.

161 Fibroblast core signature genes included Bone morphogenetic protein 7 (*Bmp7*), which is likely  
162 involved in ECM degradation, Insulin like growth factor binding protein 5 (*Igfbp5*) involved in  
163 ECM production promoting fibrosis<sup>33</sup>, and Nerve growth factor (*Ngf*), known to promote  
164 myofibroblast differentiation<sup>34,35</sup>. This indicated to us that definitive adipogenic and fibrogenic  
165 lineage markers are not lost in explants during culture (as assumed in de-differentiation), nor  
166 are they re-acquired in alternative lineages (as assumed in trans-differentiation).

167 Next, we focused on the individually clustering differentiation trajectories of adipocytes and  
168 fibroblasts in explants. Mature adipocytes (cluster A2) were characterized by high metabolic  
169 activity, and lipid biogenesis i.e. by expressing the Complement factor d (*Cfd*), Adiponectin



170 (*Adipoq*), Perilipin1 (*Plin1*), and Resistin (*Retn*) genes (Supplementary Fig. 1h). Interestingly,  
171 adipocyte cluster A1 was enriched for a gene signature consistent with a migratory phenotype,  
172 embellished with active cytoskeletal remodelling, including increased expression of Was/Wasl  
173 interacting protein family member 1 (*Wipf1*), Tripartite motif containing 44 (*Trim44*), Opticin  
174 (*Optc*), and NLR family apoptosis inhibitory protein 6 (*Naip6*). It was this adipogenic cluster  
175 that appeared transcriptionally closest to fibroblasts (Fig. 1h). Still, migratory adipocytes  
176 (cluster A1) could be consistently distinguished from fibroblast subpopulations based on their  
177 expression of adipogenic markers such as *Cfd* (Supplementary Fig. 1f), an adipokine involved  
178 in cell signalling and insulin secretion, and *Cidec* (Supplementary Fig. 1g), a gene encoding  
179 cell death activator CIDE-3 and involved in lipid droplet enlargement. Together, these data  
180 indicated that mature adipocytes might undergo rearrangement and active remodelling of  
181 cytoskeletal actin filaments in explants, reminiscent of a migratory mesenchymal cell, while  
182 still retaining the definitive adipogenic-lineage markers and not acquiring the definitive  
183 fibrogenic-cell markers.

184 Analysis of cell states of En1-lineage positive cells identified enrichment for several different  
185 biological processes (Fig. 1i). Fibroblast cluster F1 was enriched for cell migration associated  
186 genes such as Vav guanine nucleotide exchange factor 2 (*Vav2*), Slingshot protein phosphatase  
187 2 (*Ssh2*), Myosin light chain kinase (*Mylk*), Unc-51 like kinase 4 (*Ulk4*), IQ motif containing  
188 GTPase activating protein 1 (*Iqgap1*), and was transcriptionally the closest fibroblast cluster to  
189 the migratory adipocyte cluster. We identified a state consistent with fibrogenic gene expression  
190 (cluster F2), including Collagen type 1 alpha 1 chain (*Colla1*), Collagen type 3 alpha 1 chain  
191 (*Col3a1*), Fibronectin (*Fn1*), Periostin (*Postn*), Decorin (*Dcn*), Microfibril associated protein 5  
192 (*Mfap5*). Cluster F3 demonstrated a genotypic profile central to endoplasmic reticulum (ER)  
193 stress processes with expression of Mesencephalic astrocyte derived neurotrophic factor  
194 (*Manf*), Cysteine rich with EGF like domains 2 (*Creld2*), Heat shock protein 90 beta family

195 member 1 (*Hsp90b1*). Cluster F4 however, was enriched for ECM remodelling genes and  
196 processes, expressing Matrix metalloproteinases 9 and 13 (*Mmp9*, *Mmp13*), Cathepsin h (*Ctsh*),  
197 Tenascin C (*Tnc*), Lumican (*Lum*), Argininosuccinate synthase 1 (*Ass1*).

198 The pathway analysis of the top DEGs highlighted anti-microbial (anti-bacterial, anti-fungi,  
199 anti-virus) pathways in Adipoq-lineage positive cells in wounds; and highlighted fibrosis,  
200 wound healing, and ECM deposition pathways in En1-lineage positive wound fibroblasts  
201 (Supplementary Fig. 1j). The genes with high expression level in each pathway were plotted as  
202 a heat map. Those anti-microbial genes were drastically upregulated in day 1 explants and the  
203 expression returned to low levels in day 4 explants (Fig. 1k).

204 In conclusion, our data provide tantalizing evidence that fibroblasts and adipocytes refrain from  
205 cross-converting between lineages or de-differentiating in whole-skin explant models, and  
206 remain genetically bound to their original fibroblast or adipocyte identity.

207

### 208 **Terminally differentiated adipocytes mobilize and reposition during injury**

209 To study the behaviour of mature, terminally differentiated adipocytes and fibroblasts in  
210 response to injury, we employed whole-skin explants, allowing visualization and tracking of  
211 resident cells, in unprecedented detail over five days in culture, thereby overcoming restrictions  
212 associated with short imaging durations *in vivo*<sup>36</sup>. *Ex vivo* models, such as this, allow delineation  
213 of the phenotypic and behavioural responses of stromal cells after tissue damage. Briefly,  
214 whole-skin explants were isolated from the back-skin of both lineage reporter mouse strains  
215 and grown in a specialized incubation chamber that maintains constant O<sub>2</sub>/CO<sub>2</sub>, humidity and  
216 temperature. We also modified the incubation chamber with specialized silicone rings, to allow  
217 multi-photon microscopy objectives to record GFP<sup>+</sup> adipocytes and fibroblasts within the  
218 explants, in high resolution, without compromising environmental conditions. Using this

219 system, explants remained viable and underwent contraction, scar formation and re-  
220 epithelialization<sup>36</sup>.

221 With this set-up we obtained time-lapse videos, directly after explant culture, of clusters of  
222 mature and round adipocyte bundles, in both the subcutaneous fascia and in the papillary dermis  
223 where the bundles wrapped around individual hair follicles (Fig. 2a, Supplementary Movie 1).  
224 Adipocyte-lineage cells remained stationary initially, with the first signs of morphologic change  
225 visible at around twenty minutes, including the appearance of small filaments or protrusions  
226 extending from the cell membrane (Fig. 2b, c). At twenty-four hours, explants had adipocyte-  
227 lineage clusters that continued the morphologic transformation, with multiple round adipocytes  
228 acquiring oval and spindle-shaped morphologies (n=110 cells, n=3 explants). Two days after  
229 wounding, 36% of all adipocytes in papillary and fascia deposits gained filopodial extensions  
230 (Fig. 2b) that elongated to >100 $\mu$ m (length of individual cell). Supplementary Movies 2 and 3  
231 illustrate two stages of this morphologic change. Supplementary Movie 2 (and Fig. 2c) shows  
232 oval adipocyte-lineage cells extending small membrane filaments with membrane ruffling,  
233 indicative of active cytoskeletal reorganization seen in motile cells. Supplementary Movie 3  
234 shows a back-and-forth change of round-to-elongated morphology during movement. Explants  
235 on day 2 and day 3 illustrate further filopodia-like extensions, with cells acquiring sleek and  
236 slender cell bodies, resembling motile cells. Morphologically transformed adipocyte-lineage  
237 cells were interspersed with individual adipocytes adopting a fibroblast-like bipolar  
238 morphology, stretching to about 50-200  $\mu$ m, whereas rounded adipocytes were much smaller,  
239 between 10-30  $\mu$ m. As suggested by our transcriptomics data, adipocytes acquired mobility,  
240 moving away from their original fat deposit towards the formative scar region. For example, a  
241 single illustrative cell repositioned 380  $\mu$ m away from its original location (Supplementary  
242 Movie 4). Furthermore, elongated adipocytes originated from multiple niches, including fat  
243 deposits within the papillary dermis surrounding hair follicles and from within the subcutaneous

244 fascia. On day 4, motile adipocytes, had reached the centre of the scar region but still retained  
245 their elongated morphology (Fig. 2a). Supplementary Movie 5 (and Fig. 2c) shows an adipocyte  
246 acquiring a bipolar elongated morphology with extending filopodia (11.11 hrs), with a gradually  
247 protruding cell body (14.23 hrs).

248 A succession of snap-shot images of whole-skin explants indicated that adipocyte-lineage cells  
249 constantly revert back-and-forth between stationary and migratory states, with accompanying  
250 dynamic remodelling of cellular morphology between rounded and elongated/spindle-shapes  
251 (Fig.2b, Supplementary Movie 3). Those migrating adipocyte-lineage cells that had relocated  
252 at day 5 moved into the centre of the explants where they reverted to their original, lipid-filled,  
253 round morphology (Fig. 2a, Supplementary Movie 6, Supplementary Fig. 2). Quantification of  
254 morphologies of adipocyte-lineage cells revealed a gradual decrease of rounded cells from day  
255 0 to day 2 and an increase of oval, spindle shaped and elongated morphologies. A reversal of  
256 this phenotype was seen back to a strictly rounded morphology between days 3 and 5 (Fig. 2b).  
257 All forms of adipocyte-lineage cells including migratory ones retained Plin1 expression (Fig.  
258 2d).

259 Next, we investigated if mature adipocytes migrated and repositioned in tissues, in the same  
260 way as in the *ex vivo* explant model, in *in vivo* splinted wounds on the dorsal backs of Adipoq<sup>Cre</sup>;  
261 R26<sup>mTmG</sup> adult mice. Confocal imaging of wounds at day 7 revealed adipocyte-lineage cells  
262 clearly acquired fibroblast-like morphologies and translocate from their initial location within  
263 dermal white adipose tissue into the wound bed. On day 21, multiple elongated adipocyte-  
264 lineage cells aggregated near the scar region, whereas adjacent non-wounded skin adipocytes  
265 retained the classical round morphology associated with dermal white adipose tissue (Fig. 2f).  
266 These findings confirm that transcriptional changes associated with motility and phenotypic  
267 shifts are functionally relevant, with adipocytes transitionally switching morphology and  
268 actively migrating, while retaining adipocyte-committed identity.

269

270 **Absence of cell fusion events between mature adipocytes and fibroblasts**

271 Having found mature adipocytes switching morphology and migrating both *in vitro* and *in vivo*,  
272 we wanted to formally exclude all possibility of lineage crossover, therefore we examined the  
273 possibility of cell fusion between adipocytes and fibroblasts. Cell fusion includes cytoplasmic  
274 intermixing, a phenomenon that can be observed and quantified using red and green lineage-  
275 specific fluorescence reporters. Cytoplasmic intermixing would be evidenced as co-labelling of  
276 green and red (yellow fluorescence) within migratory adipocytes and fibroblasts. To do this, we  
277 analysed and quantified single cells from Adipoq<sup>Cre</sup>;R26<sup>mTmG</sup> (n=122) and En1<sup>Cre</sup>;R26<sup>mTmG</sup>  
278 lineages (n=135) in both tdTomato<sup>+</sup> and GFP<sup>+</sup> background at various stages (days) of the  
279 explant assay. Lack of co-localization between green and red labels demonstrated that both cell  
280 populations, and wound myofibroblasts, shared no history of cell fusion (Supplementary Fig.  
281 3). Collectively, our findings prove that during skin injury adipocytes and fibroblasts remain  
282 transcriptionally, behaviourally, and functionally distinct cells, with no inter-conversion or cell  
283 fusion between these two stromal lineages.

284

285 **Distinct migratory behaviours in adipocytes and fibroblasts**

286 Live imaging data indicated that migratory adipocytes share morphological features with  
287 fibroblasts despite there being no cross-lineage plasticity or fusion. To visualize and analyse  
288 these distinct motility features, and determine whether adipocytes and fibroblasts share  
289 migratory behaviours, we crossed both adipocyte and fibroblast mouse lines with a nuclear  
290 mCherry reporter (R26<sup>LSL-H2B\_mCherry</sup>), allowing tracking of individual cellular nuclei across  
291 whole skin. Furthermore, this technique allowed us to compare migratory patterns and features  
292 such as velocity, distance travelled, directionality, and collectivity between migrating  
293 fibroblasts and adipocytes. Back-skin explants were harvested from Adipoq<sup>Cre</sup>;R26<sup>LSL-H2B-</sup>

294 *mCherry* and *En1<sup>Cre</sup>;R26<sup>LSL-H2B-mCherry</sup>* double-transgenic mice and cell migration videos recorded  
295 in 3D.

296 Adipocyte-lineage cells initiate their migration from their fat deposits within hours after culture  
297 (Fig. 3a, Supplementary Movie 7). On day 1, manual tracking of cells in the scar region revealed  
298 that 53% of all evaluated adipocytes move away from their original position, yet only 20%  
299 directionally moved towards the formative scar region (defined by a minimal movement of 5  
300  $\mu\text{m}$ ) at day 1 (Fig. 3b, c). Fibroblasts, by comparison, rapidly relocating in explants. At day 1  
301 after culture, around 70% of fibroblasts had moved towards the formative scar region, with only  
302 22% of the fibrogenic cell lineage moving in other directions (Fig. 3a, b and Supplementary  
303 Movie 8).

304 On day 4, both adipocytes and fibroblasts remained motile but with widely different patterns of  
305 migration. Migration of adipocyte-lineage cells was stochastic at a population level, with  
306 individual cells generating migration tracks that were non-coordinated (Fig. 3d, and  
307 Supplementary Movie 9). In contrast, groups of hundreds of fibroblasts migrated collectively,  
308 in a uniform and coordinated manner, towards the formative scar region (Fig. 3d,  
309 Supplementary Movie 10). This indicates that most of the fibrogenic lineage cells respond by  
310 directional cell migrating into wounds, whereas adipocyte-lineage cells appear to respond and  
311 migrate less purposefully after culture.

312 Migration dynamics were further quantified using automated cell tracking in the whole explant.  
313 The average velocity of adipocyte migration differed significantly from fibroblasts, particularly  
314 at day 4. The velocities for individual adipocyte-lineage cells had greater variability throughout  
315 all time points, whereas fibroblast velocities remained consistent (Fig. 3e, f). Furthermore,  
316 movement similarity analysis confirmed that adipocyte-lineage cells move randomly, in  
317 contrast to fibroblasts (Fig. 3g). This suggests that fibroblasts act collectively, whereas  
318 adipocytes behave individually. Indeed, directional analysis of adipocyte-lineage cells and

319 fibroblasts further confirmed the collective migration path of fibroblasts, in contrast to  
320 adipocyte-lineage cells (Fig. 3h). These findings indicate that migratory adipocytes and  
321 fibroblasts respond in a vastly different manner in terms of velocity, directionality, and  
322 collectivity. It further indicates that collective cell migration is a defining characteristic of  
323 migratory fibroblasts, but not adipocytes.

#### 324 **Adipocytes do not contribute to scar formation**

325 Accretion of extracellular connective tissue matrix is another defining characteristic of  
326 fibrogenic cells<sup>37</sup>. We previously demonstrated that the fibroblasts that go on to have the ability  
327 to form scars (by depositing ECM and accumulating dense fibrous tissue) express the *Engrailed*  
328 gene temporarily during embryogenesis<sup>25</sup>. We thus compared, the scar-competent ‘Engrailed  
329 Past Fibroblasts’ (EPFs) with adipocytes, for their ability to express and secrete ECM proteins  
330 in skin explants; mature adipocytes were coloured green with GFP from *Adipoq<sup>Cre</sup>;R26<sup>mTmG</sup>*  
331 mice, and the scar-forming fibroblasts, EPFs, were coloured red with tdTomato.

332 Expression of the myofibroblast marker  $\alpha$ SMA<sup>38, 39</sup> was assessed by immunohistochemical  
333 localization at day 0. Here expression patterns correlated with a perivascular niche environment,  
334 in the absence of established scar tissue in explants. At day 4 parallel fibrils of  $\alpha$ SMA were  
335 evident within the scar region, and the fibroblasts started to retract from the developing fibrotic  
336 tissue. At this time the adipocyte-lineage cells were distant from the scar developing region,  
337 suggesting a less active role in deposition. Furthermore, in day 4 explants the ECM protein  
338 Fibronectin was deposited by GFP<sup>+</sup> tdTomato<sup>+</sup> fibroblasts and not by GFP<sup>+</sup> adipocyte-lineage  
339 cells (Fig. 4a). Migratory adipocytes did not express fibroblast proteins Fibroblast Specific  
340 Protein 1 (FSP1), Transcription Factor 21 (TCF21), or Col3a1 (Supplementary Fig. 4a-e).  
341 Myofibroblast and fibrogenic markers, such as *Ddr2*, *Lrrc17*<sup>33, 34</sup>, and ECM markers *Colla1*  
342 and *Col3a1*, were upregulated across all fibroblast subsets, but not within adipocytes (Fig. 4b).

343 To evaluate directly whether adipocyte-lineage cells produce and deposit ECM proteins, we  
344 performed 3D immuno-labelling of deposited ECM proteins (Fig. 4c). Adipocyte-lineage cells  
345 showed minimal contribution of Fibronectin or Type-I Collagen, irrespective of their  
346 morphology or motility status (Fig. 4d). As a control, baseline matrix production was compared  
347 to that induced by recombinant transforming growth factor beta 1 (TGF $\beta$ 1) stimulation, a  
348 known pro-fibrotic cytokine upregulated during the early stages of the wound healing  
349 response<sup>40</sup>. Fibroblasts deposited significant amounts of Fibronectin and Type-I Collagen,  
350 whereas adipocyte showed minimal contribution in ECM production (Fig. 4d-f). Stimulation  
351 with TGF $\beta$ 1 significantly increased Fibronectin and Type-I Collagen in En1-lineage fibroblasts,  
352 but not in adipocyte-lineage cells (Fig. 4d-f). Interestingly, TGF $\beta$ 1 altered cellular contour to  
353 the same fibroblast-like morphology seen in migratory adipocyte-lineage cells *in vivo*  
354 (Supplementary Fig. 4f). Despite their morphologic conversion then, we have seen that  
355 adipocyte-lineage cells are not fibrogenic, and they do not contribute to the ECM, which is  
356 exclusively deposited by fibroblasts.

357 We then went on to investigate mature adipocytes in wounds *in vivo*. Full-thickness excisional  
358 wounds were generated on the backskin of adult Adipoq<sup>Cre</sup>;R26<sup>mTmG</sup> and En1<sup>Cre</sup>;R26<sup>mTmG</sup> mice,  
359 in which the Adipoq-lineage adipocytes and En1-lineage fibroblasts express GFP, respectively.  
360 At day 10 and day 21, wounds were harvested and GFP<sup>+</sup> cells were sorted by FACS. The  
361 transcriptomic profiles of the sorted wound adipocyte-lineage cells and fibroblasts were  
362 analysed by mRNA-sequencing, with three independent biological repeats for each cell type at  
363 each time point. Pearson correlation analysis revealed that adipocytes from day 10 and day 21  
364 wounds were clustered together with adipocytes from adjacent uninjured skin; whereas  
365 fibroblasts from day 10, day 21 wounds and healthy skin were clustered together. The  
366 transcriptome of the adipocyte cluster was clearly distinct from the fibroblast cluster across all  
367 wound time points (Fig. 5a). Gene ontology (GO) enrichment of differentially expressed genes



368 (DEG) in adipocytes and fibroblasts in day 10 wounds indicated that wound fibroblasts and  
369 adipocytes performed distinct biological processes. Wound fibroblasts were enriched for cell-  
370 matrix adhesion, matrix deposition and regulation. By contrast, wound adipocytes in day 10  
371 wounds were enriched for sensory perception, immune regulation, and anti-microbial responses  
372 (Fig. 5b). Comparison across time points showed that the transcriptome of adipocytes from day  
373 21 wounds was closer to adipocytes from the adjacent healthy skin; whereas adipocytes from  
374 day 10 wounds upregulated gene features consistent with a migratory mesenchymal cell, which  
375 are also highly expressed in fibroblast groups; however, the expression levels of those genes  
376 were much lower than En1-lineage fibroblasts (Supplementary Fig. 5a). Still, DEG analysis  
377 within adipocytes at different time points showed they retained biological processes of anti-  
378 microbial responses, inflammation, and immune regulation (Supplementary Fig. 5b).

379 Immunofluorescence staining of wound sections showed that the migratory adipocyte-lineage  
380 cells were at higher number in day 7 wounds compared to day 21 scars (Fig. 5c). Those  
381 migratory adipocyte-lineage cells were negative for fibroblastic markers  $\alpha$ SMA (Fig. 5d) and  
382 vimentin (Fig. 5e), and proliferation marker Ki67 (Supplementary Fig. 5c), and therefore  
383 separated from fibrogenic cells. To evaluate the relevance of these observations further *in vivo*,  
384 we transplanted  $2.5 \times 10^5$  individual cells of each lineage into full-thickness dorsal wounds of  
385 immuno-deficient Rag2<sup>-/-</sup> mice. Wounds were harvested 7 days post-transplantation. ECM  
386 within the transplanted regions and adjacent non-transplanted areas were quantified as merged  
387 immunofluorescence intensities of type-I collagen and fibronectin (Fig. 5f). Transplanted  
388 fibrogenic lineage cells generated ectopic scar ECM architectures, whereas transplanted  
389 purified adipocyte-lineage cells had negligible effects on scar formation and connective tissue  
390 architecture (Fig. 5f, g).

391 Gene ontology analyses of the adipocyte lineage from both skin explants (Fig. 1j, k) and from  
392 *in vivo* wounds (Fig. 5a, b; Supplementary Fig. 5a, b) indicated they retained anti-microbial

393 responses, immune regulation, and sensory perception, while acquiring a mesenchymal  
394 migratory phenotype. To explore the physiological role of adipocytes in wounds, we performed  
395 immunostaining of mouse cathelicidin-related antimicrobial peptide (CRAMP), an ortholog of  
396 human cathelicidin (the active form is known as LL-37), on day 7 wound section from  
397 *Adipoq<sup>Cre</sup>;R26<sup>mTmG</sup>* mice. 60% of migratory adipocytes in day 7 wounds showed clear  
398 expression of CRAMP, while the expression markedly reduced in adipocytes in day 21 wounds  
399 (Fig. 5h). This data confirms that migratory adipocytes retain anti-microbial peptide functions  
400 in wounds.

## 401 **Discussion**

402 In this paper we demonstrate irreversible cell fate of mature adipocytes during skin injury,  
403 despite their remarkable morphological changes and migratory behaviours. Wound adipocytes  
404 do not convert their cellular identity into fibrogenic cells, as had been previously assumed<sup>9, 10</sup>.  
405 Morphological modulation of wound adipocytes in injured tissues were observed, but there was  
406 no evidence for adipogenic origins of fibrosing cells during injury or evidence of conversion or  
407 cell fusion from adipocytes to fibroblasts by assessment of transcriptomic, behavioural, or  
408 functional criteria.

409 Our findings that differentiated adipocytes remain committed to their lineages during the  
410 healing process, has direct implications to our understanding of homeostasis and repair of  
411 stromal tissues; impacting both basic and clinical paradigms for wound repair, regeneration,  
412 and various cell transplantation strategies for regenerative medicine. Clinically, today's  
413 standard of care for skin grafts and scaffold constructs provide closure of a wound area, but  
414 leave patients with disfiguring and debilitating scars. Current pre-clinical and clinical studies  
415 employ tissue equivalents composed of epidermal and stromal fibroblast populations embedded  
416 in various matrices. The incorporation of a dermal component into skin equivalents provides  
417 mechanical stability and supports a functional repair tissue by prevention of stricture and scar

418 formation. Clinically approved grafts, such as Apligraf®, have already received Food and Drug  
419 Administration (FDA) approval for usage in venous leg ulcers and diabetic foot ulcers. Clear  
420 delineation of stromal subsets, and understanding of their tissue specific roles and  
421 responsiveness to the environmental milieu, is crucial in the development of novel skin  
422 substitutes that enable superior ‘scarless’ regenerative outcomes in the treatment of severe skin  
423 defects, burns, accidents, congenital diseases, tumours, or chronic wounds.

424 Fat grafting, or lipofilling, is another clinical example where lineage conversions from  
425 adipocytes to fibroblasts have been proposed to enhance tissue repair processes not only by  
426 providing tissue volume, but also by reducing scar formation and fibrosis, thereby improving  
427 the functionality of the repair tissue<sup>41</sup>. Convincing clinical evidence for the effectiveness of fat  
428 grafting remains elusive. Data from our study highlights that transplanted mature adipocytes  
429 will not morphos into stromal fibroblasts, contributing to repair tissue; rather this remains the  
430 feat of the resident stromal fibroblasts. However, key reparative signals and a supportive milieu  
431 provided by the adipocytes may promote the function and response of the injured stroma. This  
432 remains an area warranting further investigation and clinical refinement as our knowledge  
433 deepens.

434 Previous studies from Horsley’s group suggested a conversion of wound adipocytes to  
435 myofibroblasts by using lineage tracing coupled with scRNA-seq<sup>9, 10</sup>. However, the cell  
436 numbers of tracked GFP expressing adipocytes in wounds included in the analysis was  
437 extremely low, and in the background noise of large numbers of fibroblasts and contaminated  
438 leukocytes and endothelial cells<sup>9</sup>. Conversion was reported based on scRNAseq data from 13  
439 wound adipocytes, whereas our analysis was conducted on a much larger population (200 -  
440 2000 wound adipocytes per sample). Nonetheless, even if the conversion happened in such few  
441 cells, it remains unclear whether they play physiologic roles in scar formation, where the  
442 predominant numbers of myofibroblasts originate from En1<sup>+</sup> fibroblast lineages. In our mRNA-  
443 seq analysis of in vivo wound fibroblasts and adipocytes, we used bulk RNA-seq with FACS

444 enriched En1-lineage positive fibroblasts and Adipoq-lineage positive adipocytes, ranging from  
445 200 to 2000 cells per sample, which largely increased the cell numbers of input adipocytes, and  
446 therefore remarkably reduced the noise. There are a couple of limitations to this study. The  
447 scRNA-seq data is derived from skin explants, which lack immune cells, blood supply and  
448 innervation, all of which could influence the transcriptomics data and therefore we have  
449 confirmed functional separation of fibroblasts and adipocytes in vivo in wounded animals.  
450 Another limitation relates to the preparation procedure of purifying adipocytes that is  
451 considered to be technically challenging and therefore relatively low numbers of adipocytes are  
452 analysed, as compared to fibroblasts. Nevertheless, we believe the sequencing analyses  
453 presented in this study are closer to the genuine physiologic roles of wound adipocytes.  
454 The scRNA-seq analysis of adipocyte in the whole-skin explant model, and the mRNA-seq data  
455 of adipocytes in excisional wounds have suggested that the migratory mature adipocytes are  
456 involved in anti-microbial responses, immune regulation, and sensory perception. The  
457 adipocytes in day 7 wounds express high level of cathelicidin-related antimicrobial peptide,  
458 confirming their anti-microbial functions in vivo. In line with these findings, skin adipocytes  
459 have been shown to execute anti-microbial functions during injury repair or skin infection, by  
460 releasing anti-microbial peptide cathelicidin<sup>42, 43</sup>. Such behaviour is believed to be regulated by  
461 toll-like receptors and retinoic acid<sup>44</sup>. Furthermore, the antimicrobial function of wound  
462 adipocytes is evolutionary conserved. Fat body cells, the equivalent of vertebrate adipocytes in  
463 *Drosophila* have been demonstrated by live imaging that they participate in wound healing, by  
464 actively migrating to wounds and physically sealing wounds. The fat body cells also help to  
465 fight against the infection by locally releasing antimicrobial peptides such as Attacin<sup>45</sup>. The  
466 other predicted physiological functions of wound adipocytes such as immune regulation and  
467 sensory perception require further investigation.  
468 This study delineates multi-modality in lineage-restricted adipocytes in their response to tissue  
469 injury. Understanding the limitations of lineage interplay between stromal cells provides key

470 knowledge to tissue repair responses central to multiple organ systems, as well as supporting  
471 translational knowledge for the development of novel tissue engineering and stromal cell-based  
472 therapeutics for impaired healing and fibrotic disorders.

473

474 **Methods**

475 **Transgenic & reporter mouse lines**

476 This study complies with all relevant ethical regulations. All animal experiments were reviewed  
477 and approved by the Government of Upper Bavaria and registered under the projects under  
478 projects ROB-55.2-2532.Vet\_02-16-61, ROB-55.2-2532.Vet\_02-19-23, and ROB-55.2-  
479 2532.Vet\_02-21-153, and conducted under strict governmental and international guidelines.  
480 C57BL/6J wild type mice were purchased from Charles River (strain code 632). En1<sup>Cre</sup> (JAX  
481 stock No. 007916), ROSA26LSL-H2B-mCherry (R26<sup>LSL-H2BmCherry</sup>) (JAX stock No. 023139),  
482 Rag2<sup>-/-</sup> mice and ROSA26mTmG (R26<sup>mTmG</sup>) reporter mice were from Stanford University<sup>25</sup>.  
483 Adipoq<sup>Cre</sup> (Jax stock No.028020) mice were from Helmholtz Center. En1<sup>Cre</sup> or Adipoq<sup>Cre</sup>  
484 transgenic mice were crossed with R26<sup>mTmG</sup> or R26<sup>LSL-H2BmCherry</sup> reporter mice for use in the  
485 described experiments. Animals were housed at the Helmholtz Center animal facility rooms  
486 that were maintained at constant temperature and humidity with a 12-h light cycle. Animals  
487 were given food and water ad libitum. No sex selection was performed in this study.

488 **Mouse genotyping**

489 Cre<sup>+</sup> animals from double-transgenic reporter mice were classified based on appropriate  
490 fluorescence present in the dorsal back of the mice. A fluorescence microscope was used for  
491 identification of Cre<sup>+</sup> neonatal mice. For adult mice, genotyping was performed to detect a 200  
492 base pair Cre band (fragment). Filter tips were used to prevent cross contamination. Genomic  
493 DNA was extracted normally from ear clip tissue. Quick Extract (QE) DNA extraction solution  
494 (Biozym, 101094) was used. Extracted Genomic DNA solution 1 µl, was added to each PCR  
495 reaction mix containing 24 µl. The PCR reaction mixture was prepared using Taq PCR core kit  
496 (Qiagen, 201205) containing Coral buffer (1X concentration final), dNTPs (10mM each), Taq  
497 polymerase enzyme (0.625 units per reaction), 0.5 µM of each forward primer (FP) 5' ATT  
498 GCT GTC ACT TGG TCG TGG C-3' and reverse primer (RP) 5' GGA AAA TGC TTC TGT  
499 CCG TTT GC-3'. PCR cycling temperature was set to 10 minutes at 94 °C for initial

500 denaturation. Followed by, amplification of 30 cycles: 30 seconds denaturation at 94 °C, 30  
501 seconds, annealing at 56 °C, 30 seconds, elongation at 72 °C. The final elongation at 72 °C was  
502 for 8 minutes, and an infinite temperature of 10 ° C was maintained. Negative controls with no  
503 template and positive controls were included. The Eppendorf master cycler instrument was  
504 used, and samples were analyzed by agarose gel electrophoresis

### 505 ***Ex vivo* explant culture**

506 The skin-fascia explant assay was performed **by following our established protocol**<sup>36,46</sup>. Briefly,  
507 back-skin was collected from new-born (postnatal day 0-1) two-colour membrane reporter  
508  $En1^{Cre};R26^{mTmG}$  or  $Adipoq^{Cre};R26^{mTmG}$  reporter or  $En1^{Cre};R26^{LSL-H2B-mCherry}$  mice or  
509  $Adipoq^{Cre};R26^{LSL-H2B-mCherry}$  nuclear reporter mice, and washed twice with DMEM/F-12  
510 (Thermo Fisher Scientific, 11320074) medium to remove contaminating blood, and then  
511 washed once with Hank's Balanced Salt Solution (HBSS, Thermo Fisher Scientific 14175095).  
512 Dorsal back skin was cut out and explants were made using a disposable Ø 2 mm biopsy punch  
513 (Stiefel, 270130) down to below the panniculus carnosus muscle, and cultured in 2 ml of  
514 DMEM/F-12 medium containing 10% FBS, 1x GlutaMAX (Thermo Fisher Scientific,  
515 35050038), 1x Penicillin/streptomycin (Thermo Fisher Scientific, 15140122), and 1x MEM  
516 non-essential amino acids (Thermo Fisher Scientific, 11140035) in 6 well plates, in a  
517 humidified 37°C, 5% CO<sub>2</sub> incubator. Fresh medium was supplied every other day and the skin  
518 tissues were harvested at the indicated time points (day 1 to day 5 after culture), with the fresh  
519 tissues serving as day 0 control. Post harvesting on designated days, explants were fixed in 2%,  
520 paraformaldehyde (PFA), overnight at 4°C for whole mount imaging and immuno-labelling, or  
521 directly used for live imaging by multiphoton microscopy or mSCRB-seq experiments.

### 522 **Sorting of adipocytes and fibroblasts**

523 Transgenic mouse lines ( $En1^{Cre};R26^{mTmG}$  or  $Adipoq^{Cre};R26^{mTmG}$ ) at P0 or P1 stage were used  
524 for sorting. Multiple skin explants for each day was pooled to maximize yield. Tissue was  
525 minced and digested using 0.5mg/ml Collagenase A (Sigma Aldrich, 10103586001) and 25

526 U/ml of DNase 1 (Sigma, 10104159001) for 1hr at 37°C with shaking. Cells were washed with  
527 complete media and filtered through cell strainers. Centrifugation was carried out for 5 min at  
528 200g and the cell pellet was resuspended in 1 ml of FACS buffer containing 2% FBS in PBS.  
529 Adipocyte and fibroblast sorting were performed based on GFP<sup>+</sup> fluorescence. En1<sup>Cre</sup>  
530 fibroblasts were incubated with the following antibodies for lineage-negative gating. 1 µg of  
531 APC-conjugated anti-mouse CD45 (BioLegend, 103112, 1:200), EpCAM (CD326)  
532 (BioLegend, 118214, 1:200), PECAM1(CD31) (BioLegend, 102410, 1:200), Ter119  
533 (BioLegend, 116212, 1:200), Tie2 (CD202b) (BioLegend, 124008, 1:200) and eFluor660-  
534 conjugated anti- LYVE1 (eBioscience, 50-0443-82, 1:200) in FACS buffer (2% [v/v] FBS in  
535 phosphate buffered saline [PBS]), on ice for 30 min. The antibody-conjugated cell pellet was  
536 washed in 5ml FACS buffer then re-suspended in 1 ml of FACS buffer (PBS +2% FBS). The  
537 cells were sorted using the a FACS Aria III sorter with a 120 µm nozzle. Fibroblasts were sorted  
538 based on the following gating scheme: Lin-TomatoRed<sup>-</sup>GFP<sup>+</sup> from En1<sup>Cre</sup>;R26<sup>mTmG</sup>.  
539 Adipocytes were sorted based on the following gating scheme: TomatoRed<sup>-</sup>GFP<sup>+</sup> from  
540 Adipoq<sup>Cre</sup>;R26<sup>mTmG</sup>.

#### 541 **Cell sorting for mcSCRB-seq**

542 Dorsal back skin was taken from En1<sup>Cre</sup>;R26<sup>mTmG</sup> or Adipoq<sup>Cre</sup>;R26<sup>mTmG</sup>, postnatal day 0 or day  
543 1 mice and washed three times with HBSS. The tissue was minced and incubated with 5ml of  
544 digestion mix for preparation of single cell suspension. mcSRCB-seq was performed with 1000  
545 adipocytes or fibroblasts sorted from day 1 and day 4 explants. The indexing parameter in Aria  
546 III was used and cells were sorted directly into 96-well DNA LoBind plates (Eppendorf). Each  
547 well was aliquoted with 5 µl lysis buffer prior to sorting. Lysis buffer consisted of Guanidine  
548 Hydrochloride (5M concentration; Sigma Aldrich), β-Mercaptoethanol (1%, Sigma Aldrich),  
549 and Phusion High Fidelity (HF) buffer (1:500 dilution, New England Biolabs: M0531L).  
550 Immediately post sorting, plates were spun down, placed on dry ice, and later stored at -80° C.

#### 551 **cDNA synthesis step of mcSCRB-seq (pre amplification step)**



552 A full step by step protocol for mcSCRB-seq is deposited in the protocols.io repository<sup>27</sup>.  
553 Before the preparation of libraries, SPRI beads were used to clean up each well. Beads were  
554 resuspended in 4 µl double distilled water along with a reverse transcription master mix (5 µl)  
555 containing Maxima H-RT enzyme (20U, Thermo Fisher), Maxima H buffer 2x (Thermo  
556 Fisher), dNTPs at concentration 2 mM each (Thermo Fisher), template switching oligo (from  
557 IDT) 4 µM and Poly ethylene glycol (PEG) 8000 15% (Sigma-Aldrich). After addition of 1µl  
558 of 2µM barcoded oligo-dT primer (E3V6NEXT, Integrated DNA technologies), cDNA was  
559 prepared according to the mcSCRBseq protocol. Template-switching and cDNA synthesis was  
560 performed at 42 ° C for 90 minutes. Barcoded cDNA was later pooled in 2 ml DNA LoBind  
561 tubes followed by clean-up using SPRI bead buffer. Purified cDNA was eluted in 17 µl and  
562 residual primers digested with enzyme Exonuclease I (from Thermo Fisher) at 37 ° C for 20  
563 min. After heat-inactivation at 80 ° C for 10 min, 30 µl PCR master mix containing Terra direct  
564 polymerase, 1.25 Units (Clontech), Terra direct buffer 1.66 X, and SINGV6 primer (IDT) 0.33  
565 µM, was added. PCR was cycling was performed as follows: 98 ° C, 3 min for initial  
566 denaturation, 19 cycles of 15 seconds at 98 ° C, 65 ° C for 30 seconds and at 68 ° C for 4  
567 minutes. Lastly, final elongation was performed at 72 ° C for 10 minutes.

#### 568 **scRNA-seq library preparation**

569 All samples were purified with SPRI beads (ratio 1: 0.8) after pre-amplification. Final elution  
570 was in 10 µL of nuclease-free water (Invitrogen). Later cDNA was quantified using the Quant-  
571 iT PicoGreen double stranded DNA Assay Kit (Thermo Fisher). A High Sensitivity DNA chip  
572 (Agilent Bioanalyzer), was used to verify size distributions. Samples that passed the quality and  
573 quantity control parameter, were used for constructing Nextera XT libraries from 0.8 ng of pre-  
574 amplified cDNA. Later, 3 'end sequences were enriched with a custom made P5 primer  
575 (P5NEXTPT5, IDT), during PCR of the libraries. Following this, Libraries were pooled and  
576 selected based on their size using 2% E-Gel Agarose EX Gels (Life Technologies); a size range

577 from 300bp to 800 bp was cut out and extracted using the MinElute kit (Qiagen). All Procedures  
578 were in accordance with the manufacturer's recommendations.

### 579 **Sequencing of scRNA-seq libraries**

580 An Illumina HiSeq 1500 instrument was used to sequence libraries. Paired-end sequencing of  
581 libraries was performed on high output flow cells. To generate molecular and cellular barcodes,  
582 16 bases were sequenced with the 1st read, 50 bps sequenced in the 2nd read into the cDNA  
583 fragment, and 8 bases were read to obtain the i7 barcode.

### 584 **Full-thickness excisional wound model**

585 Adult (8-16 weeks old) Adipoq<sup>Cre</sup>;R26<sup>mTmG</sup> or En1<sup>cre</sup>;R26<sup>mTmG</sup> mice were anesthetized with  
586 MMF (medetomidine at 500 µg/kg, midazolam at 5mg/kg and fentanyl at 50 µg/kg body  
587 weight). Dorsal back hair was shaved with a hair clipper, and further removed with depilatory  
588 cream. Two full-thickness excisional wounds were created with a 5 mm diameter biopsy punch  
589 (Stiefel). Mice were supplied with analgesic. Wounds were harvested at days 7, 10, or 21 post-  
590 wounding depending on the subsequent analyses.

### 591 **Bulk RNA-sequencing of adipocytes and fibroblasts from in vivo wounds**

592 Full-thickness excisional wounds were made on the back of Adipoq<sup>Cre</sup>;R26<sup>mTmG</sup> mice and  
593 En1<sup>Cre</sup>;R26<sup>mTmG</sup> mice. The digested samples were filtered through 100 µm cell strainers to  
594 allow collection of adipocytes with bigger size, and centrifuged at 300 g for 5 minutes, and  
595 floating adipocytes were isolated using a pipette. Adipocytes and fibroblasts were FACS sorted  
596 from day 10 and day 21 wounds of respective transgenic lines as GFP<sup>+</sup> cells. 200 – 2000 FACS  
597 sorted cells were lysed and cDNA synthesis and the subsequent expansion with 8 PCR cycles  
598 were performed using the Smart-Seq® v4 Ultra® Low Input RNA Kit for Sequencing (Takara  
599 #634889), according to manufacturer's instructions. The amplified cDNA was purified with  
600 NucleoMag NGS Clean-up and Size Select beads (Takara 7449705). The library preparation  
601 and sequencing were performed by Biomarker Technologies (BMKGene) GmbH (Münster,  
602 Germany) with Illumina Novaseq 6000. Standardized RNAseq pipelines written in Nextflow,

603 nf-core/rnaseq were adapted for trimming, alignment to mm10 by STAR and counts calling by  
604 salmon as default setting<sup>47</sup>. The raw counts were used for a differential gene expression analysis  
605 (DEG) using DESeq2 (version 1.34.0 with R version 4.1.2)<sup>48</sup>. Normalized counts were scaled  
606 for Pearson's correlation matrices and plotting feature genes expression in heat map. Gene  
607 ontology (GO) enrichment of DEGs was done using clusterProfiler (version 4.2.2) and viewed  
608 by ggplot2 (Version 3.3.6)<sup>49</sup>.

#### 609 **Primary data processing of RNA-seq data**

610 Processing of all raw FASTQ data was done using zUMIs pipeline along with STAR to obtain  
611 expression profiles for barcoded UMI data<sup>28, 29</sup>. Mapping was done to the reference genome  
612 (mm10 / 09) concatenated with the ERCC and GFP reference. Gene annotations were obtained  
613 from Ensembl (GRCm38 / mm10 - GRCh38.84).

#### 614 **Processing of mcSCRB-seq single cell data set**

615 The raw count matrices output by the zUMIs pipeline were analyzed using Scanpy<sup>50</sup> (v.1.6.0).  
616 For barcode filtering, we excluded barcodes with less than 1000 detected genes. We assessed  
617 the number of unique molecular identifiers (UMIs) for each sample using violin plots, and  
618 retained cells with a number of UMIs below 250000. Genes were only considered if they were  
619 expressed in at least 3 cells in the data set.

620 Normalization was performed based on scran's approach<sup>51</sup>, in which size factors are calculated  
621 and used to scale the counts in each cell. Log transformation was used via Scanpy's pp.log1p.  
622 Top variable genes were established with scanpy's pp.highly\_variable\_genes and flavor set to  
623 "cell\_ranger". Highly variable genes were the basis for the principal component analysis (PCA)  
624 and neighborhood graph construction via pp.pca and pp.neighbours (adipocytes: n\_pcs = 15,  
625 n\_neighbors = 5; fibroblasts: (n\_pcs = 20, n\_neighbors = 10). For clustering the louvain  
626 algorithm was employed at resolution 0.5, resulting in 6 clusters within the adipocyte and  
627 fibroblast populations, respectively. For both subsets the UMAPs and diffusion maps were  
628 generated using Scanpy's functions tl.umap and tl.diffmap.

629 As we anticipate a small fraction of contamination with adipocyte cells in the fibroblast labelled  
630 population, we cleared away such adipocyte cells. For that we assessed the similarity to  
631 adipocytes for each cell in the fibroblast subset with scanpy's `tl.score_genes` function, using an  
632 adipocyte reference signature (adipocyte cell type from Mouse Cell Atlas, link:  
633 <http://bis.zju.edu.cn/MCA/gallery.html?tissue=Neonatal-Skin,cluster3>). Unsupervised louvain  
634 clustering at resolution 1 revealed one cluster with particularly high scoring cells, which was  
635 then removed from the analysis.

636 For the comparison of both lineages, the two refined subsets were re-combined into one object  
637 and the list of variable genes set to the union of the list established on the two subsets. The PCA  
638 was re-calculated and the neighbourhood graph established for the concatenated object (`n_pcs`  
639 `= 15`, `n_neighbors = 20`). Cell type marker genes for the 12 subclusters were established with  
640 `tl.rank_genes_groups` and `method = "wilcoxon"`.

#### 641 **Differential Gene Expression across the two lineages**

642 We performed differential expression analysis with `diffxpy` (v.0.7.4). In a first analysis we  
643 compared the differences between adipocyte and fibroblast lineage using the Wald test. To  
644 circumvent the problem that certain genes are highly upregulated in only one of the 6  
645 subclusters per lineage, we constrained the model to each subcluster by adding `constraint_loc`  
646 `= [subcluster: lineage]` to the model. Genes are labelled as differentially expressed if their  
647 Benjamini-Hochberg corrected p-value was less than 0.5, have a `log2foldchange` of greater 1  
648 and are expressed in at least 10% of cells in the relevant lineage. This resulted in a list of 88  
649 genes for adipocytes and 198 genes for fibroblast.

650 Gene Set Enrichment Analysis was performed using these differentially regulated genes as  
651 input for the python package `GOATOOLS`<sup>52</sup>.

#### 652 **Whole mount 3D imaging by multi-photon microscopy**

653 Post fixation, explants were thoroughly washed in PBS 3X times, 1 hour each, followed by,  
654 embedding in NuSieve GTG agarose (2%, Lonza, cat.no. 859081) in a 35mm dish (Falcon,

655 cat.no. 351008). Imaging was performed under a Leica SP8 Multiphoton microscope (Leica,  
656 Germany). Tiles were merged with a LAS X (v4.8, Leica) with smooth overlap blending, and  
657 data was finally visualized with Imaris image analysis software (v9.1.0 and v9.2, Bitplane, UK)  
658 using contrast and brightness adjustments.

### 659 **Live 3D multi-photon microscopy**

660 Live samples were embedded as above, and live imaging was performed using multi-photon  
661 microscopy. Imaging medium included DMEM/F-12. Time-lapse imaging was performed over  
662 15 hours under the multi photon microscope. A modified incubation system, with heating and  
663 gas control (ibidi 10915 & 11922), was used to guarantee physiologic and stable conditions  
664 during imaging. Temperature control was set to 37 °C with 5% CO<sub>2</sub>-supplemented air. 3D data  
665 was processed with Imaris 9.1.0 (Bitplane, UK) and ImageJ (1.52i). Contrast and brightness  
666 were adjusted for better visibility.

### 667 **Manual cell tracking**

668 Manual cell tracking was performed on explants from nuclear reporter lines (En1<sup>Cre</sup>; R26<sup>LSL-</sup>  
669 H2B-mCherry or Adipoq<sup>Cre</sup>;R26<sup>LSL-H2B-mCherry</sup>). ImageJ software with “Manual Tracking” plugin  
670 (version 2.1.1) was used. In brief, an area of 700µm X 700µm in the scar region of the explant  
671 was cropped from 3D-Time lapse datasets. Nuclear spots were identified after subjecting to  
672 maximum-intensity projection. Migration of individual cells was tracked over time.  
673 Trajectories and individual track information with coordinates were exported as TIFF and excel  
674 file respectively. Graphical visualization and analysis of these trajectories were performed using  
675 “R”. Color-ramps were generated for each track as a function of time (Blue; first time point;  
676 Red; last time point). Cell movement patterns were quantified based on whether a cell moved  
677 away (towards to epidermis) or towards the scar region (center of the explant).

### 678 **Automated cell tracking**

679 Automated cell tracking was performed using 3D-Time lapse datasets of whole explants made  
680 from nuclear reporter lines using the Imaris software package (v9.2.1, Bitplane, UK). Live

681 videos were generated with a 15 min interval from explant stages of day 1 and day 4. Tracks  
682 were generated from 3D data using mCherry fluorescence and an intensity-based spot detection  
683 tool. Tracks were visualized in time-coded color representation, ranging from purple to red. For  
684 snapshot images, full tracks representing the last 10 time points were shown for better visibility  
685 and to prevent overcrowding. Dragon tail representation was used in live videos to better  
686 visualize directed collective and non-directed migration patterns.

### 687 **Quantification of cell migration**

688 Employing the tracked cell trajectories, the displacement in 3D for every cell between  
689 consecutive time frames was calculated. To compare experiments, mean cell displacements  
690 were added up and plotted over time. To analyse the movement similarity of neighbouring cells,  
691 the neighbourhood was determined via Delaunay triangulation. Neighbours were defined as  
692 cells that are direct neighbours in the resulting neighbourhood graph. Next, the 3D movement  
693 vectors for a cell and its neighbours for consecutive time points were calculated. The 3D  
694 movement similarity for cell '*u*' and neighbour '*v*' can be assessed by calculating the  
695 intermediate angle between the respective movement vectors:

$$696 \alpha_{u,v} = \cos^{-1} \left( \frac{u_x v_x + u_y v_y + u_z v_z}{\sqrt{u_x^2 + u_y^2 + u_z^2} \sqrt{v_x^2 + v_y^2 + v_z^2}} \right)$$

697 Finally, all angles were averaged to produce one movement similarity score. For display  
698 reasons the angles were inverted and the movement similarity ranges from 90° (random  
699 movement) to 180° (coordinated movement).  
700

### 701 **Whole mount and conventional immunostaining**

702 Whole-mount samples were pre-incubated in Dulbecco's Phosphate-Buffered Saline (DPBS,  
703 Thermo Fisher Scientific 14190169) containing 0.2% gelatin (Sigma G1393), 0.5% Triton-  
704 X100 (Sigma X100) and 0.01% Thimerosal (Sigma T8784) (PBS-GT), for 24h at room  
705 temperature. They were then incubated with primary antibodies. Primary antibody incubation  
706 was carried out at room temperature for 72 hours, followed by washing with PBSGT, 3X times,

707 1 hour each. Fluorophore-conjugated secondary antibodies were purchased from Thermo Fisher  
708 Scientific. The samples were incubated, rotating, with the labelled antibodies in PBSGT  
709 (1:1000) for 24h at room temperature. Samples were then washed with PBSGT 3X times, 1  
710 hour each and stored in fresh PBSGT at 4°C in the dark until imaging. The following **primary**  
711 antibodies were used: Collagen I (1:200 Rockland, cat.no. 600-401-103-0.1), Collagen III  
712 (1:200, Abcam ab7778), Fibronectin 1 (1:250, Abcam ab23750),  $\alpha$ -SMA (1:200, Abcam  
713 ab5694), Perilipin1 (1:200, Abcam, ab3526), CRAMP (1:200, Novus Biologicals, NB100-  
714 98689), FSP1 (1:200, Abcam, ab58597), PDGFR $\alpha$  (1:200, R&D Systems AF1062), Ki67  
715 (1:200, Abcam, ab15580), TCF21 (1:250, Abcam, ab32981), Vimentin (1:200, Abcam,  
716 ab8978). **AlexaFluor488-, AlexaFluor568-, or AlexaFluor647-conjugated secondary antibodies**  
717 **against suitable species were used for fluorescence labelling, for example: AF488-conjugated**  
718 **goat anti-rabbit IgG (Life Technologies, A11008, 1:500), AF568-conjugated donkey anti-rabbit**  
719 **IgG (Life Technologies, A10042, 1:500), AF647-conjugated donkey anti-rabbit IgG (Life**  
720 **Technologies, A31573, 1:500). The images were taken with a Thunder Imaging Systems**  
721 **(Leica) acquired by Leica Application Suite v4.8, or an AxioImager (Carl Zeiss) acquired by**  
722 **Zen v3.0 blue edition.**

### 723 **Lipid tox staining**

724 All procedures followed were in accordance with manufacturer's instructions. HCS Lipid TOX  
725 Deep Red (Thermo Scientific, H34477) was used at 1:200 dilution on PFA fixed whole mount  
726 explants and incubated at 37° C for 2 h. Whole mount imaging used a Multiphoton microscope.

### 727 **Extracellular matrix deposition assay**

728 In vitro culture of FACS-sorted cells were obtained from transgenic mouse lines (En1<sup>Cre</sup>;  
729 R26<sup>mTmG</sup> or Adipoq<sup>Cre</sup>;R26<sup>mTmG</sup>) at the P0 or P1 stage. Explants from Cre<sup>+</sup> mice were collected  
730 on day 1 and day 4. Tissue was minced and digested using 0.5mg/ml Collagenase A and 25u/ml  
731 of DNase 1 for 1hr at 37°C with shaking. Cells were washed with complete media and filtered  
732 through cell strainers. En1<sup>Cre+</sup> samples were incubated with the following antibodies for lineage-

733 negative gating: APC- anti-mCD31, mCD45, EpCam (CD326), PECAM-1, mTie2(CD202b),  
734 mTer119, anti-mLyve-1 on ice for thirty minutes. The antibody-conjugated cell pellet was then  
735 washed with, 5 ml FACS buffer and re-suspended in 1 ml of FACS buffer (PBS +2% FBS).  
736 The cells were sorted by a FACS Aria III sorter with a 120 µm nozzle. EPFs were sorted based  
737 on Lin<sup>-</sup>TomatoRed<sup>+</sup>GFP<sup>+</sup> fluorescence. For Adipoq<sup>Cre</sup> positive samples, digestion procedures  
738 were similar to those mentioned above but excluded lineage markers. En1<sup>+</sup> fibroblasts and  
739 Adipocytes were later plated in 384 well glass bottom plates coated with 1% Porcine Gelatin.  
740 3000 cells were plated per well and cultured in complete medium with or without 5ng/ml  
741 recombinant TGFβ1 (rTGFβ1). Adipocytes were cultured in complete medium with or without  
742 5ng/ml rTGFβ1 and 5ng/ml bFGF (basal FGF). Both cultures were maintained in 37°C  
743 incubator for 72 hours and media was replenished once.

#### 744 **Decellularization and extracellular matrix immunostaining**

745 Adipocytes and fibroblasts in 384-well plates were cultured up to 3 days. Confluent fibroblasts  
746 or adipocytes were de-cellularized **using an established protocol**<sup>53, 54</sup>. **Briefly**, confluent culture  
747 dishes were incubated at 4°C for 45 mins with very gentle stirring, sequentially, first in DDW  
748 (double distilled water) with Triton X 100 (0.1%) at 4°C, then in freshly prepared 2% sodium  
749 deoxycholate. This was followed by two 30-minute incubations at room temperature, first in  
750 DDW containing 1 M NaCl and second in DDW containing pancreatic DNase (30 µg/ml, source  
751 porcine), MgSO<sub>4</sub> (1.3 mM) and CaCl<sub>2</sub> (2 mM). Plates were later rinsed very gently with distilled  
752 water, and 4% PFA was used to fix the deposited extracellular matrix for 15 mins at RT. After  
753 washing twice gently with PBS, permeabilization was performed in PBS containing BSA (1%)  
754 and Triton X (0.1%). Blocking was carried out for 1hr at RT in PBS containing 1% BSA and  
755 10% serum of the species in which secondary antibody was raised. Next followed a primary  
756 antibody incubation at 4°C overnight, gentle rinsing with PBS and later secondary antibody was  
757 applied for 1hr at RT. Finally, nuclei were stained with DAPI for 10mins at RT. Plates were  
758 washed 3X times with 1X PBS and stored in PBS, and images were taken with a confocal



759 microscope (LSM 710, Zeiss). Percent fluorescence was measure after converting the images  
760 to binary format in Image J and calculating the area of the fluorescence signal.

### 761 **Cell transplantation**

762 FACS sorted cells were first thoroughly and gently washed with PBS. Cells were later  
763 resuspended in PBS at  $5 \times 10^5$  cells per ml. An equal volume of ice-cold Matrigel was mixed  
764 with the sell suspension (Phenol red free, Corning, 356231). Cell suspensions in Matrigel were  
765 made to a final concentration of  $2.5 \times 10^5$  cells per ml and stored in an ice bucket until  
766 intradermal injections. Rag2<sup>-/-</sup> mice, at age 10–12 weeks, received adipocyte lineage and  
767 fibroblast lineage cell - Matrigel transplants. 5 mm diameter excisional wounds (full-thickness,  
768 2 wounds) were made on the dorsal back skin of mice, as described above. Two 50  $\mu$ l injections  
769 of adipocyte lineage and fibroblast lineage cell-Matrigel suspensions were made near the wound  
770 site. Two similar intradermal injections of 50  $\mu$ l PBS alone were made for control wounds.  
771 Cell-Matrigel suspensions were left for 10 minutes, followed by placing silicone splints around  
772 the wound. Gentle press was applied around the wound as mentioned above in the splinted  
773 wound method. Whole skin including scar tissue was harvested 7 days post wounding. Lastly,  
774 harvested tissue was fixed at 4 ° C, overnight using 2% PFA. After 3 PBS washes, the tissues  
775 were prepared for histological analysis.

### 776 **Statistics and Reproducibility**

777 GraphPad Prism 8 was used for all statistical analyses except for sequencing data. Unless  
778 otherwise indicated, mean  $\pm$  SD values are reported in the graphs. The exact statistical analyses  
779 used to quantify data, the exact values of n, and the exact p values are stated in the respective  
780 figure legends. For simplicity, p values below 0.0001 were stated as equal to 0.0001. All  
781 experiments were performed at least three times independently with similar results.

782 No statistical method was used to predetermine sample size. Required experimental sample  
783 sizes were estimated based on previous established protocols in the field. The sample sizes were  
784 adequate as the differences between experimental groups were reproducible. No data were

785 excluded from the analyses. The experiments were not randomized. The Investigators were not  
786 blinded to allocation during experiments and outcome assessment.

787

#### 788 **Data availability**

789 The generated scRNA-seq data has been deposited in the Gene Expression Omnibus under the  
790 accession number GSE175650  
791 [<https://www.ncbi.nlm.nih.gov/geo/query/acc.cgi?acc=GSE175650>]. The generated mRNA-  
792 seq data has been deposited in the Gene Expression Omnibus under the accession number  
793 GSE215912 [<https://www.ncbi.nlm.nih.gov/geo/query/acc.cgi?acc=GSE122159>]. The raw  
794 sequence data has been deposited in the Sequence Read Archive (SRA) with the BioProject ID  
795 PRJNA889718 [<https://www.ncbi.nlm.nih.gov/bioproject/PRJNA889718/>]. Source data for  
796 Figure 2, 4, 5 has been provided in the Supplementary Table 3.

797

#### 798 **Code availability**

799 scRNA-seq data analysis was performed with scanpy (v1.6.0) and diffxpy (v0.7.4). Gene set  
800 enrichment analysis was performed with goatools (v0.18). Custom R and Python code to  
801 reproduce the analyses and figures based on scRNA-seq data generated in this manuscript has  
802 been deposited in GitHub [[https://github.com/schillerlab/2021\\_Stromal\\_Fate\\_Restriction](https://github.com/schillerlab/2021_Stromal_Fate_Restriction)].

803

804

805 **References**

- 806 1. Spickard, E.A., Joshi, P.M. & Rothman, J.H. The multipotency-to-commitment transition in  
807 Caenorhabditis elegans-implications for reprogramming from cells to organs. *FEBS Lett* **592**,  
808 838-851 (2018).
- 809 2. Merrell, A.J. & Stanger, B.Z. Adult cell plasticity in vivo: de-differentiation and  
810 transdifferentiation are back in style. *Nat Rev Mol Cell Biol* **17**, 413-425 (2016).
- 811 3. Desai, V.D., Hsia, H.C. & Schwarzbauer, J.E. Reversible modulation of myofibroblast  
812 differentiation in adipose-derived mesenchymal stem cells. *PLoS One* **9**, e86865 (2014).
- 813 4. Giordano, A. *et al.* Mammary alveolar epithelial cells convert to brown adipocytes in post-  
814 lactating mice. *J Cell Physiol* **232**, 2923-2928 (2017).
- 815 5. Guerrero-Juarez, C.F. *et al.* Single-cell analysis reveals fibroblast heterogeneity and myeloid-  
816 derived adipocyte progenitors in murine skin wounds. *Nat Commun* **10**, 650 (2019).
- 817 6. Marangoni, R.G. *et al.* Myofibroblasts in murine cutaneous fibrosis originate from  
818 adiponectin-positive intradermal progenitors. *Arthritis Rheumatol* **67**, 1062-1073 (2015).
- 819 7. Plikus, M.V. *et al.* Regeneration of fat cells from myofibroblasts during wound healing.  
820 *Science* **355**, 748-752 (2017).
- 821 8. Schmidt, B.A. & Horsley, V. Intradermal adipocytes mediate fibroblast recruitment during  
822 skin wound healing. *Development* **140**, 1517-1527 (2013).
- 823 9. Shook, B.A. *et al.* Dermal Adipocyte Lipolysis and Myofibroblast Conversion Are Required  
824 for Efficient Skin Repair. *Cell Stem Cell* **26**, 880-895 e886 (2020).
- 825 10. Shook, B.A. *et al.* Myofibroblast proliferation and heterogeneity are supported by  
826 macrophages during skin repair. *Science* **362**, eaar2971 (2018).
- 827 11. Zhang, Z. *et al.* Dermal adipose tissue has high plasticity and undergoes reversible  
828 dedifferentiation in mice. *J Clin Invest* **129**, 5327-5342 (2019).
- 829 12. Ban, C.R. & Twigg, S.M. Fibrosis in diabetes complications: pathogenic mechanisms and  
830 circulating and urinary markers. *Vasc Health Risk Manag* **4**, 575-596 (2008).
- 831 13. Adigun, R., Goyal, A., Bansal, P. & Hariz, A. Systemic Sclerosis, in *StatPearls Treasure*  
832 *Island (FL)*; 2020).
- 833 14. Buras, E.D. *et al.* Fibro-Adipogenic Remodeling of the Diaphragm in Obesity-Associated  
834 Respiratory Dysfunction. *Diabetes* **68**, 45-56 (2019).
- 835 15. Contreras, O. *et al.* Cross-talk between TGF-beta and PDGFRalpha signaling pathways  
836 regulates the fate of stromal fibro-adipogenic progenitors. *J Cell Sci* **132** (2019).
- 837 16. Mahmoudi, S. *et al.* Heterogeneity in old fibroblasts is linked to variability in reprogramming  
838 and wound healing. *Nature* **574**, 553-558 (2019).
- 839 17. Tchkonina, T. *et al.* Fat tissue, aging, and cellular senescence. *Aging Cell* **9**, 667-684 (2010).
- 840 18. Jopling, C., Boue, S. & Izpisua Belmonte, J.C. Dedifferentiation, transdifferentiation and  
841 reprogramming: three routes to regeneration. *Nat Rev Mol Cell Biol* **12**, 79-89 (2011).
- 842 19. Johansson, C.B. *et al.* Extensive fusion of haematopoietic cells with Purkinje neurons in  
843 response to chronic inflammation. *Nat Cell Biol* **10**, 575-583 (2008).
- 844 20. Blasi, A. *et al.* Dermal fibroblasts display similar phenotypic and differentiation capacity to  
845 fat-derived mesenchymal stem cells, but differ in anti-inflammatory and angiogenic potential.  
846 *Vasc Cell* **3**, 5 (2011).
- 847 21. Denu, R.A. *et al.* Fibroblasts and Mesenchymal Stromal/Stem Cells Are Phenotypically  
848 Indistinguishable. *Acta Haematol* **136**, 85-97 (2016).
- 849 22. Wagers, A.J. & Weissman, I.L. Plasticity of adult stem cells. *Cell* **116**, 639-648 (2004).
- 850 23. Correa-Gallegos, D. *et al.* Patch repair of deep wounds by mobilized fascia. *Nature* **576**, 287-  
851 292 (2019).
- 852 24. Jiang, D. *et al.* Two succeeding fibroblastic lineages drive dermal development and the  
853 transition from regeneration to scarring. *Nat Cell Biol* **20**, 422-431 (2018).
- 854 25. Rinkevich, Y. *et al.* Skin fibrosis. Identification and isolation of a dermal lineage with intrinsic  
855 fibrogenic potential. *Science* **348**, aaa2151 (2015).
- 856 26. Straub, L.G. & Scherer, P.E. Metabolic Messengers: Adiponectin. *Nat Metab* **1**, 334-339  
857 (2019).

- 858 27. Bagnoli, J.W. *et al.* Sensitive and powerful single-cell RNA sequencing using mcSCRB-seq.  
859 *Nat Commun* **9**, 2937 (2018).
- 860 28. Dobin, A. *et al.* STAR: ultrafast universal RNA-seq aligner. *Bioinformatics* **29**, 15-21 (2013).
- 861 29. Parekh, S., Ziegenhain, C., Vieth, B., Enard, W. & Hellmann, I. zUMIs - A fast and flexible  
862 pipeline to process RNA sequencing data with UMIs. *Gigascience* **7** (2018).
- 863 30. auf dem Keller, U., Kumin, A., Braun, S. & Werner, S. Reactive oxygen species and their  
864 detoxification in healing skin wounds. *J Invest Dermatol Symp Proc* **11**, 106-111 (2006).
- 865 31. Townsend, L.K., Weber, A.J., Barbeau, P.A., Holloway, G.P. & Wright, D.C. Reactive  
866 oxygen species-dependent regulation of pyruvate dehydrogenase kinase-4 in white adipose  
867 tissue. *Am J Physiol Cell Physiol* **318**, C137-C149 (2020).
- 868 32. Fan, Y., Zhang, G., Vong, C.T. & Ye, R.D. Serum amyloid A3 confers protection against  
869 acute lung injury in *Pseudomonas aeruginosa*-infected mice. *Am J Physiol Lung Cell Mol*  
870 *Physiol* **318**, L314-L322 (2020).
- 871 33. Nguyen, X.X., Muhammad, L., Nietert, P.J. & Feghali-Bostwick, C. IGF1P-5 Promotes  
872 Fibrosis via Increasing Its Own Expression and That of Other Pro-fibrotic Mediators. *Front*  
873 *Endocrinol (Lausanne)* **9**, 601 (2018).
- 874 34. Liu, Z. *et al.* p75 neurotrophin receptor regulates NGF-induced myofibroblast differentiation  
875 and collagen synthesis through MRTF-A. *Exp Cell Res* **383**, 111504 (2019).
- 876 35. Palazzo, E. *et al.* Role of neurotrophins on dermal fibroblast survival and differentiation. *J*  
877 *Cell Physiol* **227**, 1017-1025 (2012).
- 878 36. Jiang, D. *et al.* Injury triggers fascia fibroblast collective cell migration to drive scar formation  
879 through N-cadherin. *Nat Commun* **11**, 5653 (2020).
- 880 37. Xue, M. & Jackson, C.J. Extracellular Matrix Reorganization During Wound Healing and Its  
881 Impact on Abnormal Scarring. *Adv Wound Care (New Rochelle)* **4**, 119-136 (2015).
- 882 38. Gabbiani, G., Ryan, G.B. & Majne, G. Presence of modified fibroblasts in granulation tissue  
883 and their possible role in wound contraction. *Experientia* **27**, 549-550 (1971).
- 884 39. Nagamoto, T., Eguchi, G. & Beebe, D.C. Alpha-smooth muscle actin expression in cultured  
885 lens epithelial cells. *Invest Ophthalmol Vis Sci* **41**, 1122-1129 (2000).
- 886 40. Blobel, G.C., Schiemann, W.P. & Lodish, H.F. Role of transforming growth factor beta in  
887 human disease. *N Engl J Med* **342**, 1350-1358 (2000).
- 888 41. Krastev, T.K., Schop, S.J., Hommes, J., Piatkowski, A. & van der Hulst, R. Autologous fat  
889 transfer to treat fibrosis and scar-related conditions: A systematic review and meta-analysis. *J*  
890 *Plast Reconstr Aesthet Surg* **73**, 2033-2048 (2020).
- 891 42. O'Neill, A.M. *et al.* Antimicrobial production by perifollicular dermal preadipocytes is  
892 essential to the pathophysiology of acne. *Sci Transl Med* **14**, eabh1478 (2022).
- 893 43. Zhang, L.J. *et al.* Innate immunity. Dermal adipocytes protect against invasive *Staphylococcus*  
894 *aureus* skin infection. *Science* **347**, 67-71 (2015).
- 895 44. Hopfinger, A., Karrasch, T., Schaffler, A. & Schmid, A. Regulation of CAMP (cathelicidin  
896 antimicrobial peptide) expression in adipocytes by TLR 2 and 4. *Innate Immun* **27**, 184-191  
897 (2021).
- 898 45. Franz, A., Wood, W. & Martin, P. Fat Body Cells Are Motile and Actively Migrate to  
899 Wounds to Drive Repair and Prevent Infection. *Dev Cell* **44**, 460-470 e463 (2018).
- 900 46. Wan, L. *et al.* Connexin43 gap junction drives fascia mobilization and repair of deep skin  
901 wounds. *Matrix Biol* **97**, 58-71 (2021).
- 902 47. Ewels, P.A. *et al.* The nf-core framework for community-curated bioinformatics pipelines. *Nat*  
903 *Biotechnol* **38**, 276-278 (2020).
- 904 48. Love, M.I., Huber, W. & Anders, S. Moderated estimation of fold change and dispersion for  
905 RNA-seq data with DESeq2. *Genome Biol* **15**, 550 (2014).
- 906 49. Wu, T. *et al.* clusterProfiler 4.0: A universal enrichment tool for interpreting omics data.  
907 *Innovation (Camb)* **2**, 100141 (2021).
- 908 50. Wolf, F.A., Angerer, P. & Theis, F.J. SCANPY: large-scale single-cell gene expression data  
909 analysis. *Genome Biol* **19**, 15 (2018).
- 910 51. Lun, A.T., McCarthy, D.J. & Marioni, J.C. A step-by-step workflow for low-level analysis of  
911 single-cell RNA-seq data with Bioconductor. *F1000Res* **5**, 2122 (2016).

912 52. Klopfenstein, D.V. *et al.* GOATOOLS: A Python library for Gene Ontology analyses. *Sci Rep*  
913 **8**, 10872 (2018).  
914 53. Bonenfant, N.R. *et al.* The effects of storage and sterilization on de-cellularized and re-  
915 cellularized whole lung. *Biomaterials* **34**, 3231-3245 (2013).  
916 54. van der Velden, J.L. *et al.* TGF-beta1-induced deposition of provisional extracellular matrix  
917 by tracheal basal cells promotes epithelial-to-mesenchymal transition in a c-Jun NH2-terminal  
918 kinase-1-dependent manner. *Am J Physiol Lung Cell Mol Physiol* **314**, L984-L997 (2018).  
919

920

921 **Acknowledgements**

922 We thank S. Ussar, Institute of Obesity and Diabetes (IDO), Helmholtz Zentrum München for  
923 Adipoq<sup>cre</sup> mice; S. Dietzel and the Core Facility Bioimaging at the Biomedical Centre of the  
924 Ludwig-Maximilians-Universität München for access and support with the multi-photon  
925 system; L. Richter, Core Facility Flow Cytometry (CF FlowCyt) at the Biomedical Center  
926 (BMC), Ludwig-Maximilians-Universität for access and support with the FACS; T.  
927 Walzthoeni, Genomics Core Facility, Helmholtz Zentrum München for sharing nf-core/rnaseq  
928 configuration in high performance computing at Helmholtz Munich. **The Figure 1a, 4c and**  
929 **Supplementary Figure 1a were created with BioRender with a valid license.** Y.R. is supported  
930 by the Human Frontier Science Program Career Development Award (CDA00017/2016), the  
931 German Research Foundation (RI 2787/1-1 AOBJ: 628819), the Fritz–Thyssen–Stiftung (2016-  
932 01277), the Else-Kröner-Fresenius-Stiftung (2016\_A21) and the European Research Council  
933 Consolidator Grant (ERC-CoG 819933). **H.B.S. is support by the German Center for Lung**  
934 **Research (DZL) and the Helmholtz Association.** V.L. and C.M. are supported by the European  
935 Union’s Horizon 2020 research and innovation program from the European Research Council  
936 (ERC-866411).

937

938 **Author contributions**

939 Conceived and designed the analysis: Y.R., D.J., H.B.S.; Collect the data: S.K.G., R.D., A.M.S.,  
940 P.R., J.W.B., Y.L., S.C., D.J.; Contributed data or analysis tools: D.C.-G., L.C.D., H.-G.M.;  
941 Performed the analysis: S.K.G., R.D., A.M.S., M.A., J.Z., P.R., D.C.-G., Y.L., I.A., V.L., C.M.,  
942 W.E., H.-G.M. H.B.S., D.J., Y.R.; Wrote the paper: S.K.G., L.C.D., H.B.S., D.J., Y.R.

943

944 **Competing interests**

945 The authors declare no competing interests.

946

947 **Figure Legends**

948 **Figure 1. Adipocyte and fibroblast lineages retain their identities in skin explant model.**

949 **a**, Schematic workflow of *ex vivo* whole-skin explant assay and molecular crowding single cell  
950 RNA barcoding and sequencing (mcSCRBseq). The skin explants from neonatal  
951 Adipoq<sup>Cre</sup>;R26<sup>mTmG</sup> or En1<sup>Cre</sup>;R26<sup>mTmG</sup> skin were cultured in 96-well plate with fascia side face  
952 up. The GFP<sup>+</sup> cells were FACS sorted from explants that were collected 1 day or 4 days after  
953 culture for single cell sequencing. F, fascia; D, dermis; E, epidermis. **b**, Dimension-reduced  
954 single cell transcriptomic data is visualized through Uniform Manifold Approximation and  
955 Projection (UMAP), coloured by Louvain cluster and **c**, time point of extraction. **d**, Similarities  
956 of marker gene signatures for the 12 cell states (6 states per lineage) along with relative  
957 frequency of each cell state per time point. Colour indicates Pearson correlation coefficients for  
958 each pairwise comparison across transcriptional cell states in adipocyte and fibroblast lineages.  
959 **e**, The heatmap shows relative expression of the indicated genes across cell states and lineages.  
960 **f**, Gene set enrichment results in an adipocyte core signature gene list (88 genes). **g**, Gene set  
961 enrichment results in a fibroblast core signature gene list (198 genes). **h**, Diffusion maps show  
962 adipocyte cell states and the gene expression levels of the indicated genes. **i**, Diffusion maps  
963 show fibroblast cell states and gene expression levels of the indicated genes. **j**, Pathway focused  
964 gene expression analysis of adipocytes and fibroblasts at day 1 and day 4. **k**, Expression of  
965 feature genes of listed pathway in adipocytes and fibroblasts at day 1 and day 4. Z score of  
966 individual gene was normalization read counts across samples.

967

968 **Figure 2. Spatio-temporal characterization of migratory adipocytes.**

969 **a**, Morphological changes of adiponectin-lineage positive cells (GFP) in skin explants from  
970 Adipoq<sup>Cre</sup>;R26<sup>mTmG</sup> neonates in culture from Day 0 to Day 5 at low (upper panel, scale bar 200  
971  $\mu\text{m}$ ) and high (lower panel, scale bar 50  $\mu\text{m}$ ) magnification. **b**, Quantification of adipocyte  
972 morphologies throughout 5-day explant assay, n = 3 explants per timepoint, **mean  $\pm$  SD**. **c**,

973 Morphology dynamics of adipocytes. Snapshots of single representative cells from Day 0 to  
974 Day 5 showing transition from characteristic mature round to migratory states of adipocytes.  
975 Time format-hour.min. Scale bar: 20 microns. **d**, Three migratory morphologies of adipocytes  
976 are positive for Perilipin1 by immuno-labelling. Scale bar: Classic round 20  $\mu\text{m}$ , Oval spiky: 10  
977  $\mu\text{m}$  and Elongated fibroblast-like morphologies: upper panel 20  $\mu\text{m}$ , lower panel 30  $\mu\text{m}$ . **This**  
978 **experiment was repeated three times independently with similar results.** **e**, Quantification of  
979 Perilipin1-positive and -negative cells in explants, **n = 3 biological repeats, mean  $\pm$  SD.** **f**,  
980 Adipocytes superficially resemble fibroblasts after wounding in live mice: Control back skin of  
981 Adipoq<sup>Cre</sup>;R26<sup>mTmG</sup> mice, GFP<sup>+</sup> adipocytes are round, located around hair follicles. Following  
982 the wound healing experiment at day 7, Adipoq-lineage (GFP) cells seen at the wound periphery  
983 have a fibroblast-like elongated morphology. At day 21 after injury, activated adipocytes still  
984 have a fibroblastic shape as the skin tissue is undergoing remodelling. Arrowheads indicate  
985 round adipocytes, and arrows indicate elongated, activated fibroblast-like cells. Scale bars: 50  
986  $\mu\text{m}$ . **This experiment was repeated three times independently with similar results.**

987

### 988 **Figure 3. Distinct adipocytes and fibroblast migrations.**

989 3D whole mount time-lapse imaging snapshots of single-cell tracks skin explants generated  
990 from Adipoq<sup>cre</sup> or En1<sup>Cre</sup> crossed to R26<sup>LSL-H2B-mCherry</sup> reporter mice. **a**, Snapshots of adipocyte-  
991 and fibroblast-migration tracks on day 1. **b**, Adipocyte and fibroblast tracks on day 4, generated  
992 by automated cell tracking using Imaris version 9.2. (Bitplane). **c**, Manual tracks of adipocytes  
993 and fibroblasts in the scar region of explants at day 1 and day 4; the plot shows the difference  
994 in migration distance and type of movement in the scar region of both adipocytes and  
995 fibroblasts. N=2 videos per time point. Scar regions were cropped (700 $\mu\text{m}$  X 700 $\mu\text{m}$ ) from  
996 whole explant and cells manually tracked. Blue indicates starting time and red is the end-point.  
997 **d**, 3 main types of movement quantified using manually annotated single cell tracks present in  
998 **c**, **n = 3 biological repeats, mean  $\pm$  SD.** **e**, Velocity of migratory adipocytes and fibroblasts is



999 calculated using time-lapse videos and automated single cell tracks. Velocity variation and  
1000 amplitude difference from time point 4 -9 hours across all samples are shown in higher  
1001 magnification (lower panel). The red crosses (+) indicate the mean velocities of the indicated  
1002 time points. **f**, Spline graph of day 4 showing differences of mean velocity between adipocytes  
1003 and fibroblasts. **g**, Neighbour similarity analysis of day 4 explants using automated single-cell  
1004 tracks generated from 3D time lapse videos. The colour bar represents the movement angles 0°  
1005 (red, coordinated movement) to 90° (blue, random movement). Fibroblast migrations are  
1006 coordinated and collective, whereas adipocyte migrations are random and individual. **h**,  
1007 Directed and non-directed movement of fibroblasts and adipocytes respectively at day 4. Scale  
1008 bars:100 µm.

1009

1010 **Figure 4. Adipocytes are non fibrogenic in *ex vivo* models.**

1011 **a**, Immunostainings of Adipoq<sup>Cre</sup>;R26<sup>mTmG</sup> explants at day 0 and day 4. Adiponectin-lineage  
1012 cells in green, fibroblasts in red, and marker gene αSMA (top) and Fibronectin 1 (bottom)  
1013 expression in magenta. Merged channel image of the whole explant (left), magnified area of  
1014 individual channels (right). **Scale bars: 100 µm in low magnification images, 20 µm in high**  
1015 **magnification images. This experiment was repeated three times independently with similar**  
1016 **results.** **b**, Feature plots generated from combined analysis of mcSCRSeq showing adipocyte,  
1017 myofibroblast, and extracellular matrix-specific enrichment in cell type-specific clusters. **c-f**,  
1018 Adipocyte-lineage cells deposit marginal matrix proteins than fibroblasts under scarring  
1019 conditions. **c**, Schematic of *in vitro* matrix deposition assay and quantification using Image J.  
1020 **d**, FACS-sorted adipocytes, and fibroblasts were cultured *in vitro*, with and without rTGFβ1  
1021 stimulation for 72hrs, followed by decellularization and immunolabelling of deposited matrix  
1022 Collagen 1 and Fibronectin 1. **Scale bars: 50 µm.** **e,f**, Quantification of percent fluorescence of  
1023 deposited matrix showing higher percentage of deposited matrix when compared to adipocytes,

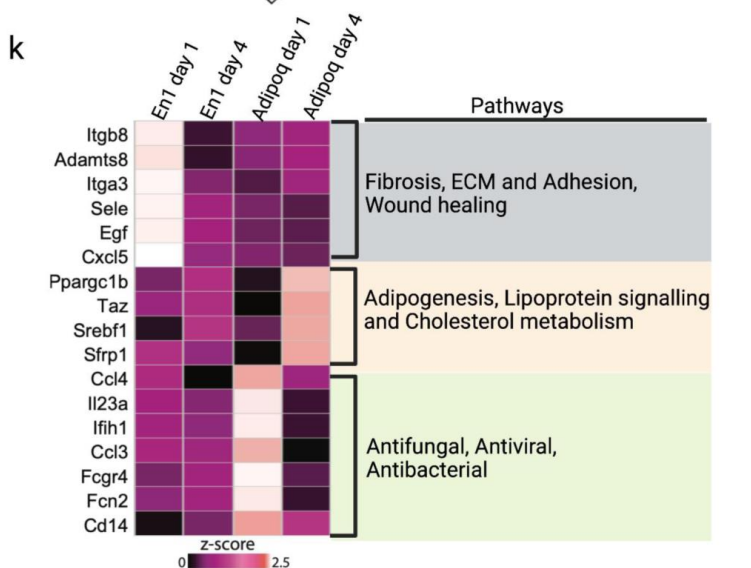
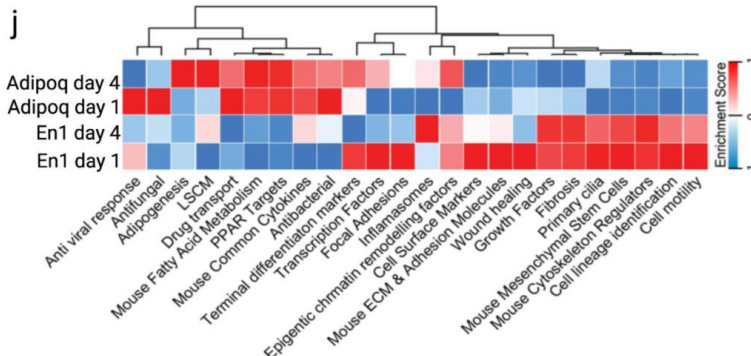
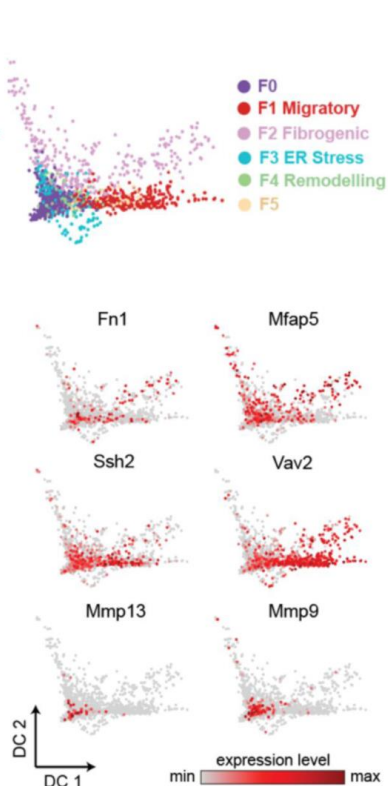
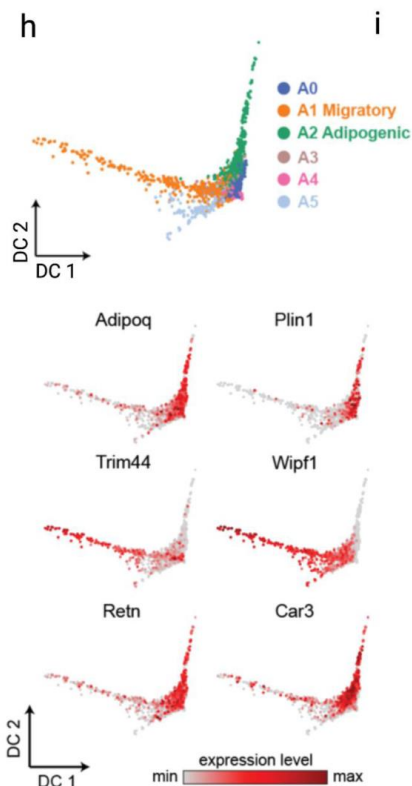
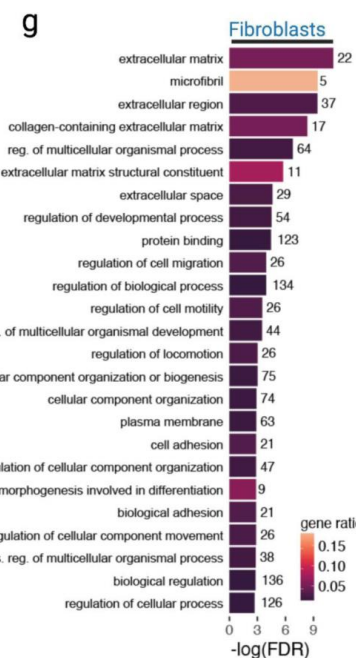
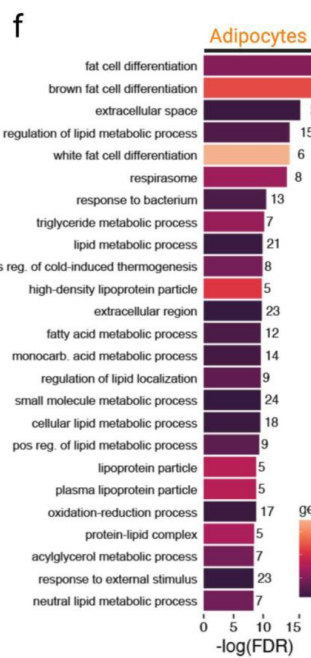
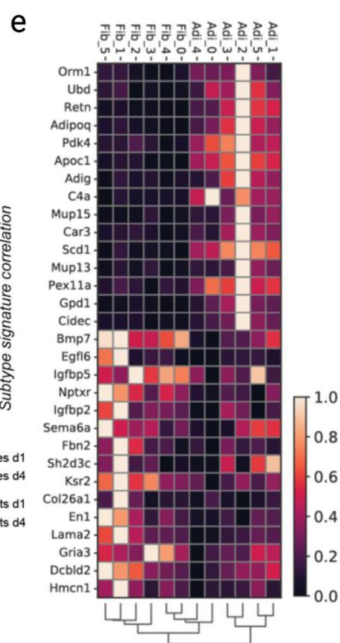
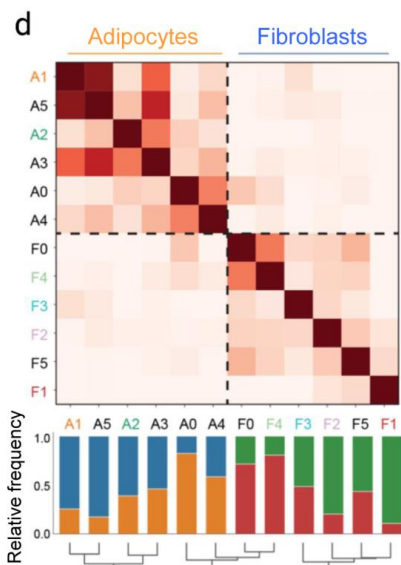
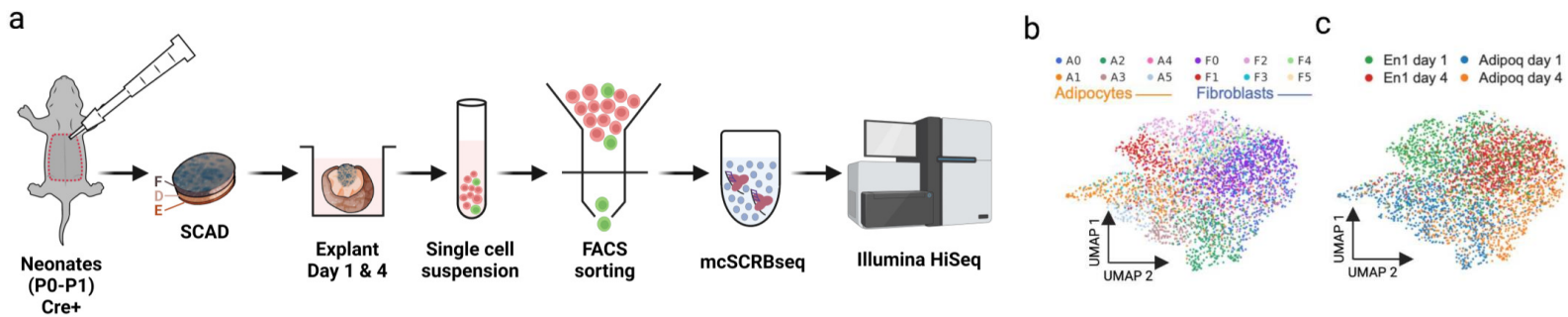
1024 n = 3 biological replicates and 4 images of each replicate, **Mean ± SD**, Two-way ANOVA with  
1025 95% CI.

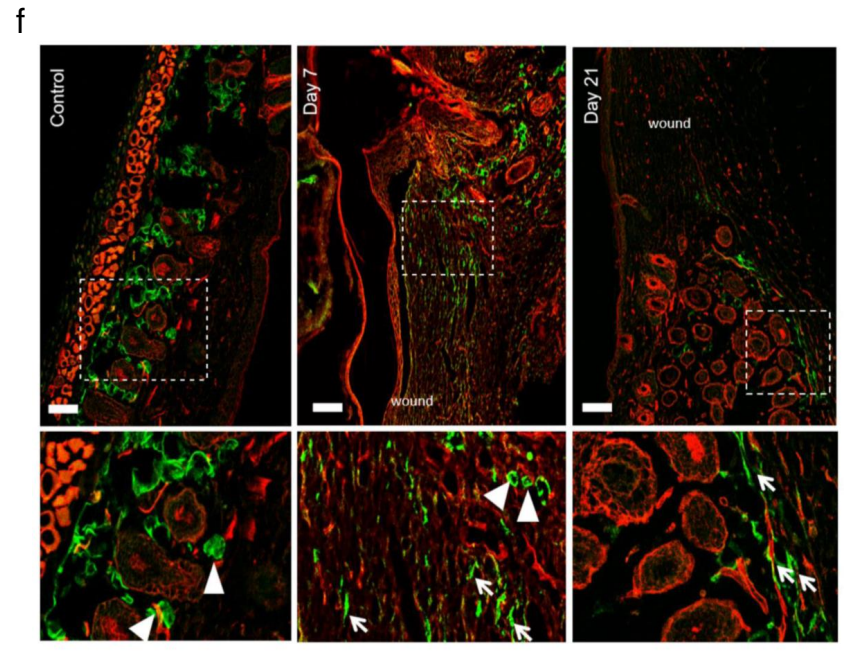
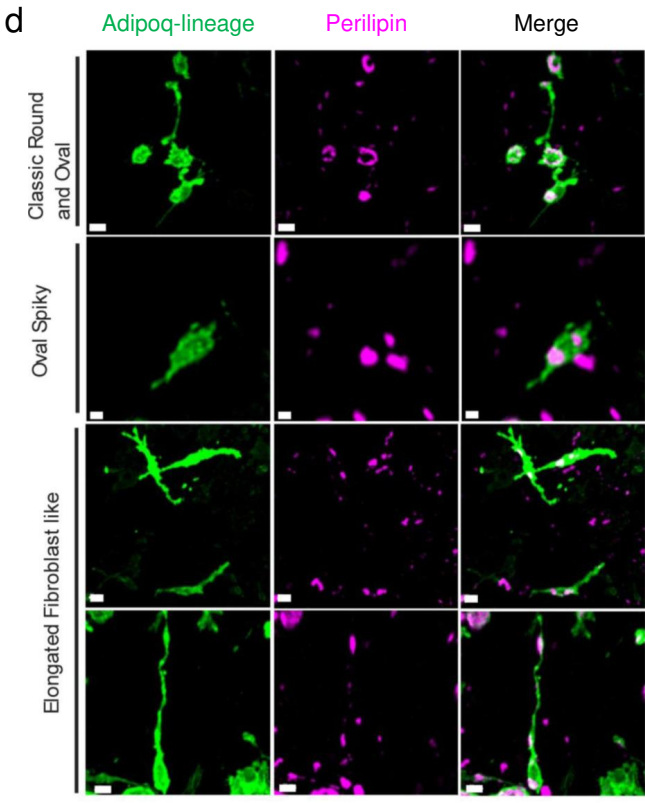
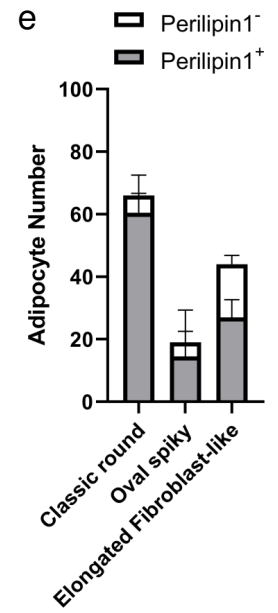
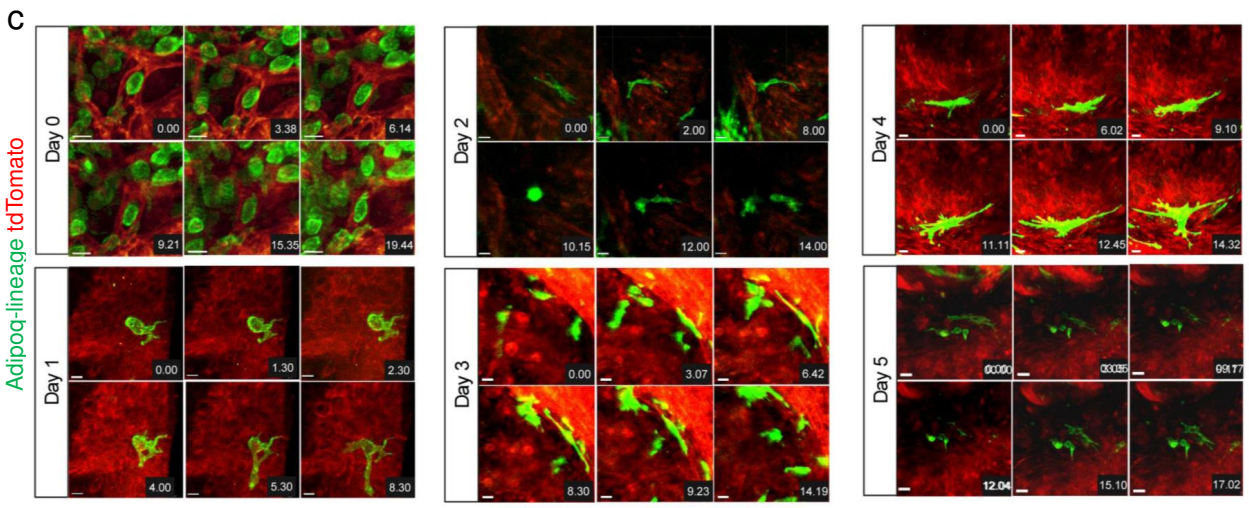
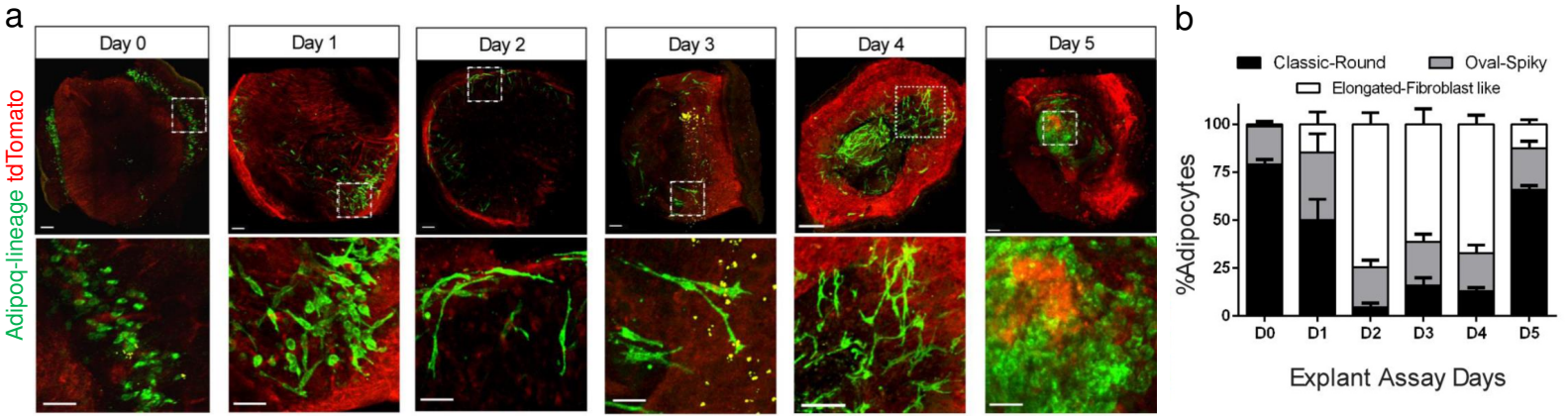
1026

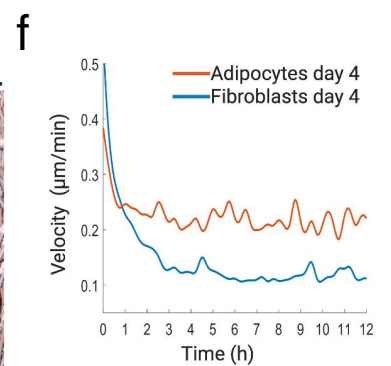
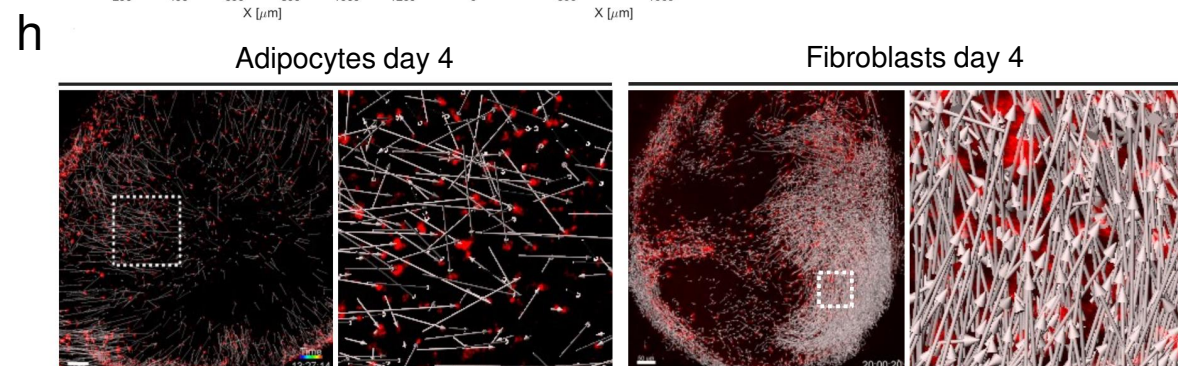
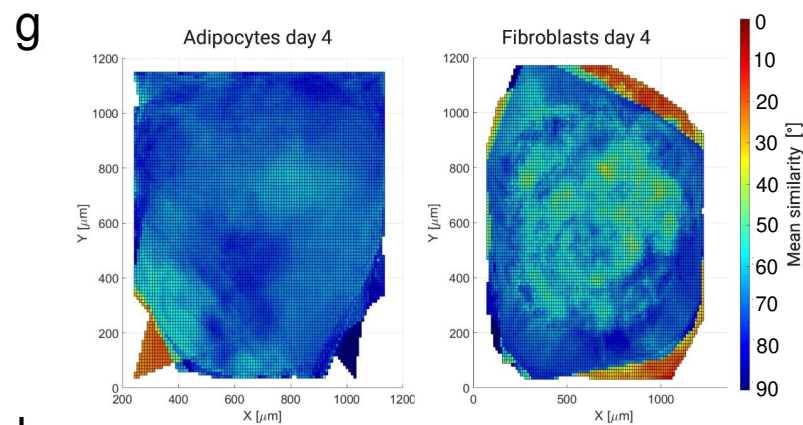
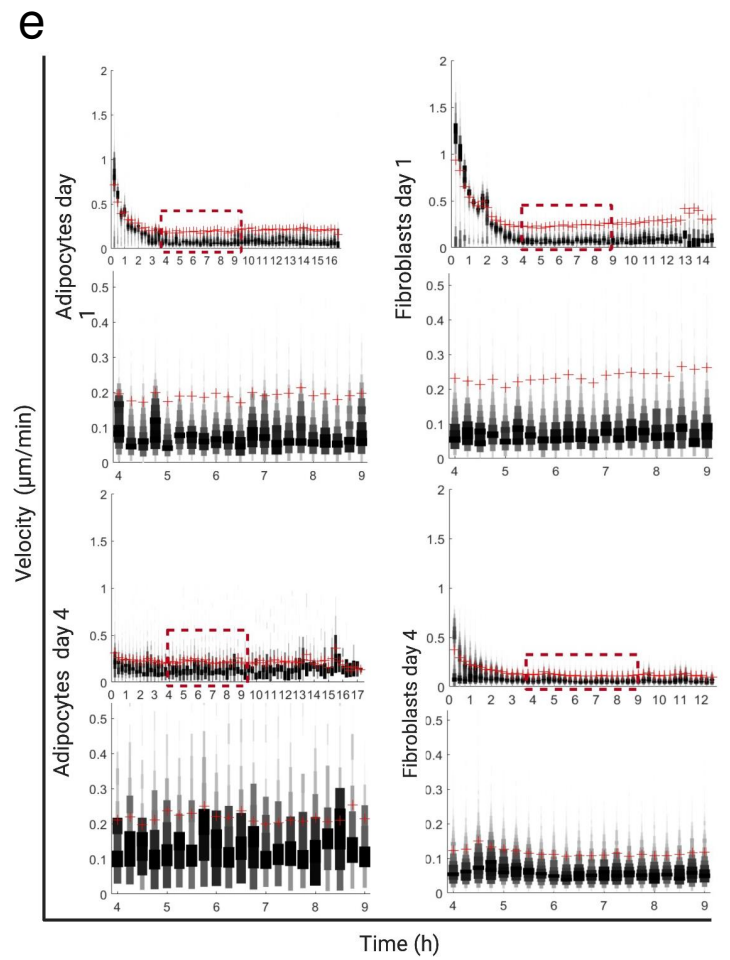
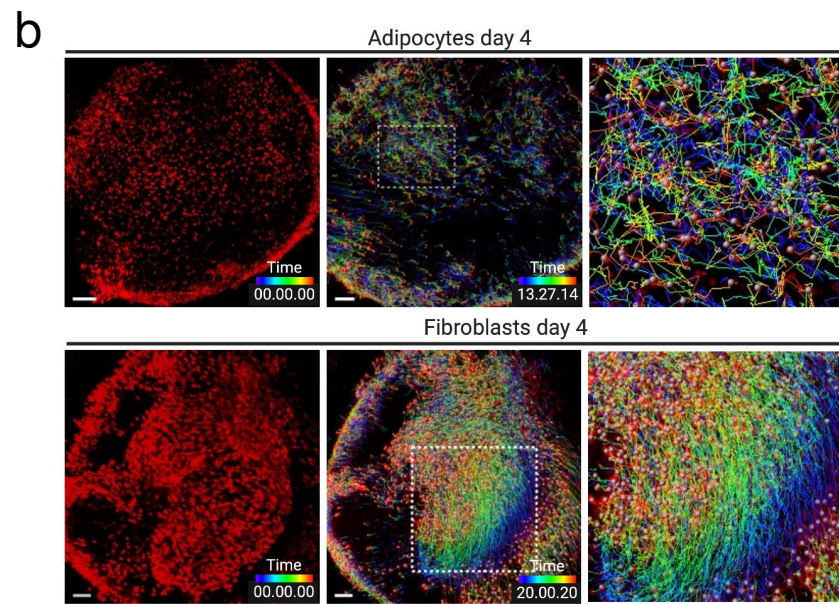
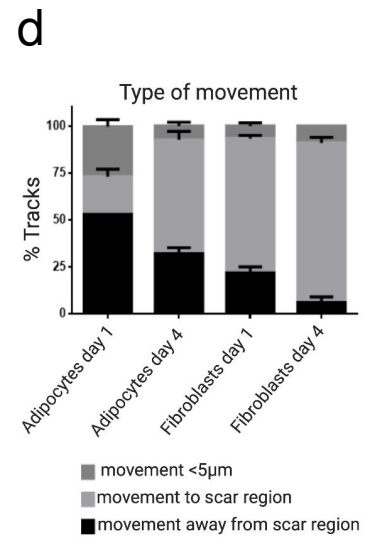
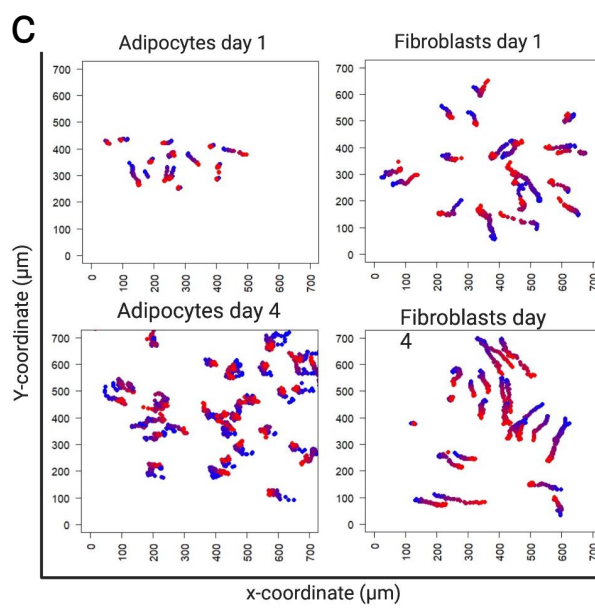
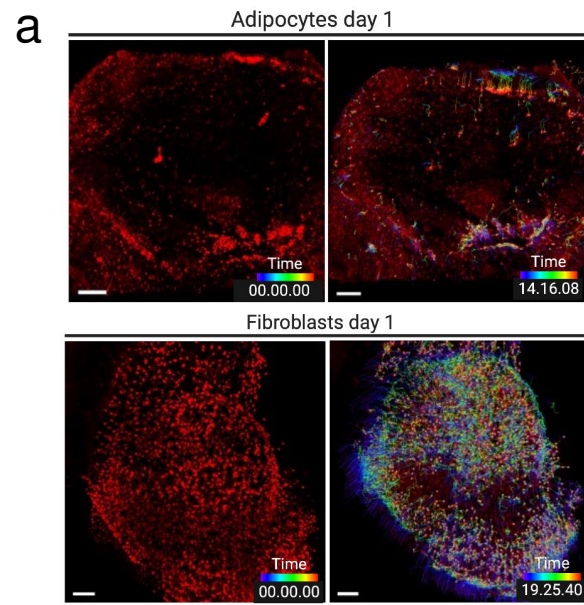
1027 **Fig. 5. Adipocytes are non fibrogenic in wounds.**

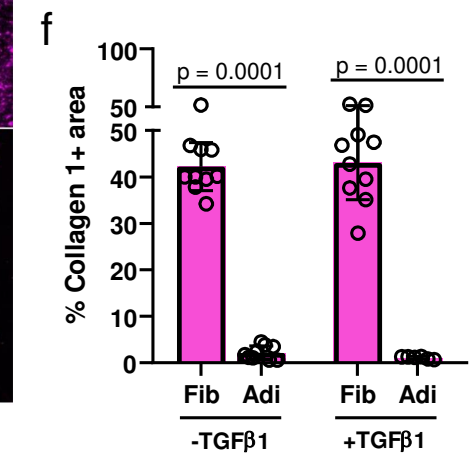
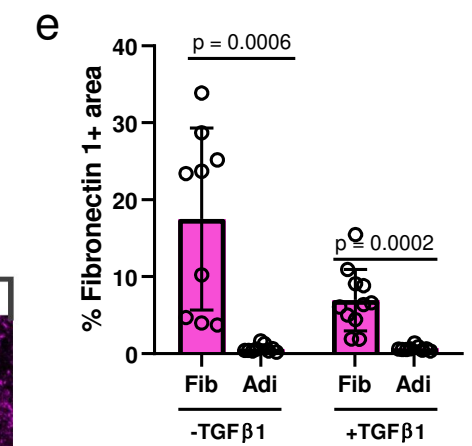
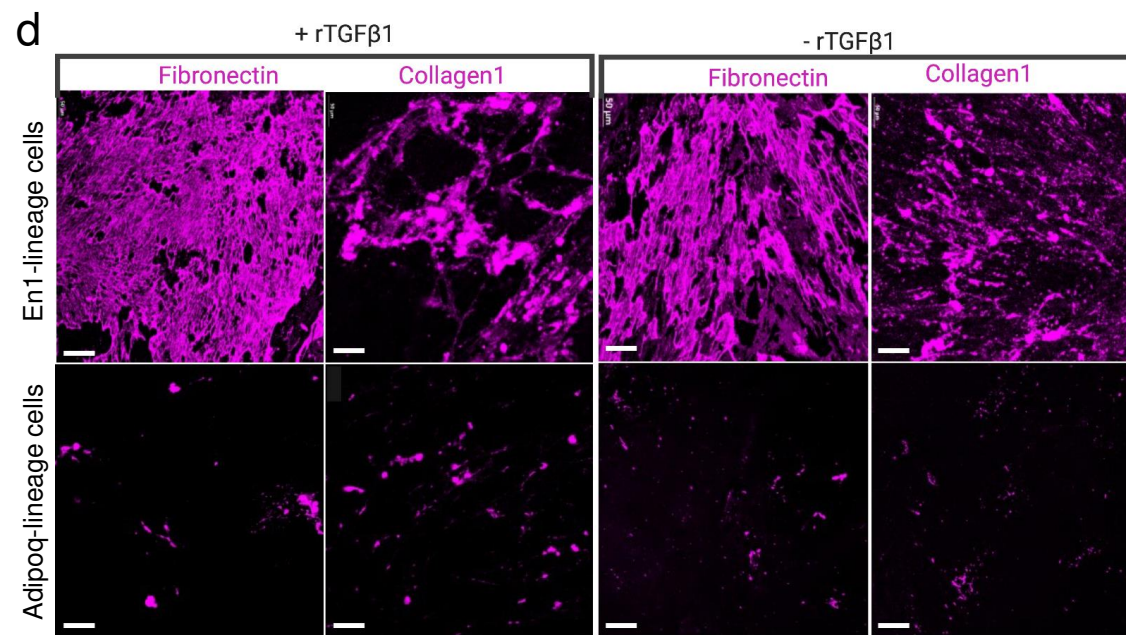
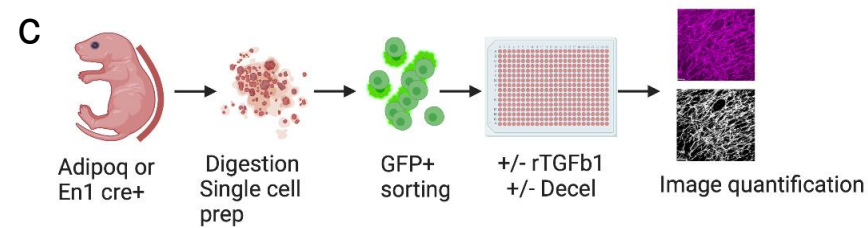
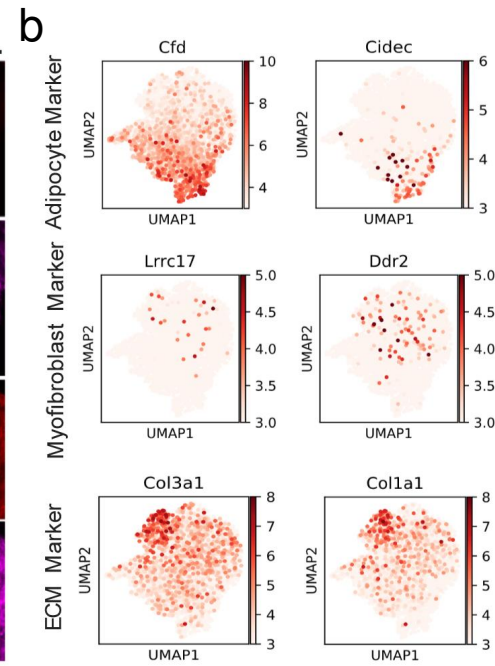
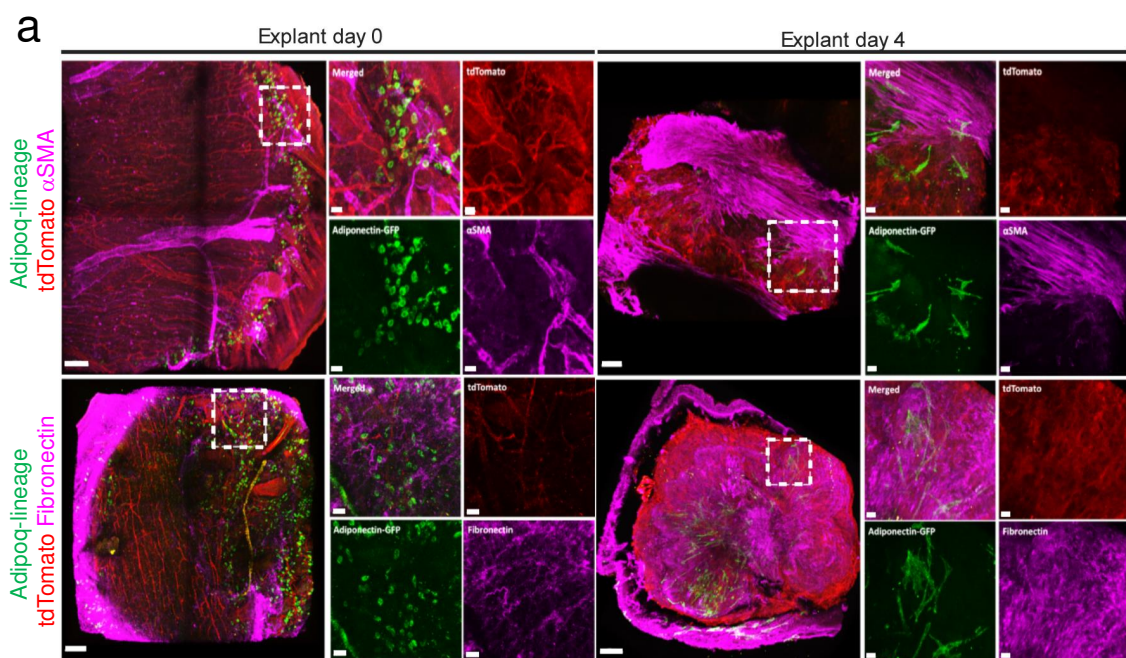
1028 mRNA-seq was performed with FACS sorted adipocytes and fibroblasts from day 7 and 21  
1029 wounds and adjacent skin of Adipoq<sup>Cre</sup>;R26<sup>mTmG</sup> and En1<sup>Cre</sup>;R26<sup>mTmG</sup> mice, respectively. Each  
1030 cell type at each time point includes three independent biological replicates. **a.** Pearson  
1031 correlation analysis of all 18 samples. Colour in each cells represented Pearson correlation  
1032 coefficients for every pairwise comparison. **b.** GO term enrichment based on DEGs of  
1033 adipocytes and fibroblasts from day 10 wounds. Filled colour represented number of genes  
1034 enriched relative to all DEGs. Cryosections of day 7 and day 21 wounds from  
1035 Adipoq<sup>Cre</sup>;R26<sup>mTmG</sup> mice were subjected for immunofluorescence staining. **c.** Representative  
1036 images and quantification of Perilipin (magenta) in GFP positive cells. Data are numbers of  
1037 GFP<sup>+</sup>Perilipin<sup>+</sup> cells per high magnification field, **n = 6 independent samples**, mean ± SD,  
1038 unpaired two-tailed t-test. **d.** Representative images and quantification of αSMA (magenta) in  
1039 GFP positive cells. The migratory elongated and rounded adipocytes are negative for αSMA.  
1040 At day 7 there is widespread αSMA staining in the centre of the wound, whereas only  
1041 physiological αSMA is found in the hair follicle dermal sheath at day 21. **Data are percentage**  
1042 **of αSMA<sup>+</sup>GFP<sup>+</sup> cells and αSMA<sup>-</sup>GFP<sup>+</sup> cells in total GFP<sup>+</sup> cells, n = 6 independent samples,**  
1043 **mean ± SD.** **e.** Representative images and quantification of vimentin (magenta) in GFP positive  
1044 cells. Data are percentage of Vimentin<sup>+</sup>GFP<sup>+</sup> cells and Vimentin<sup>-</sup>GFP<sup>+</sup> cells in total GFP<sup>+</sup> cells,  
1045 **n = 6 independent samples**, mean ± SD. **f.** Transplantation of FACS-sorted adipocytes or  
1046 fibroblasts from P1 new born mice into adult Rag2<sup>-/-</sup> immunodeficient mouse back skin into an  
1047 excisional wound model. Immunolabelling with anti-Collagen1 or anti-Fibronectin 1 and  
1048 quantification of associated extracellular matrix in the transplanted regions. **g.** Quantification

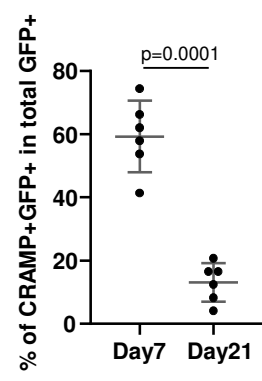
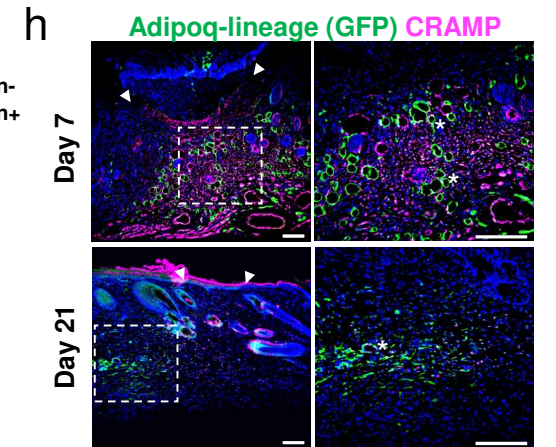
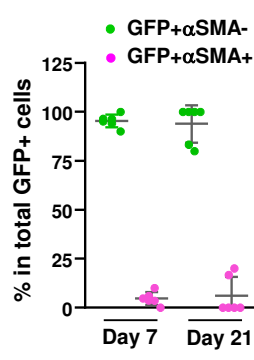
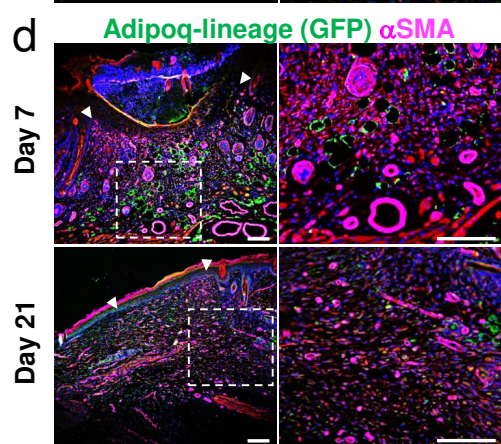
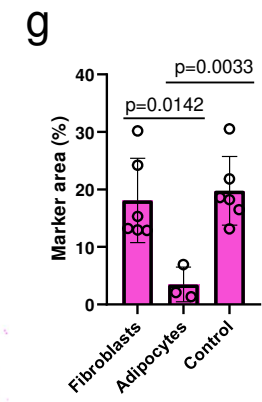
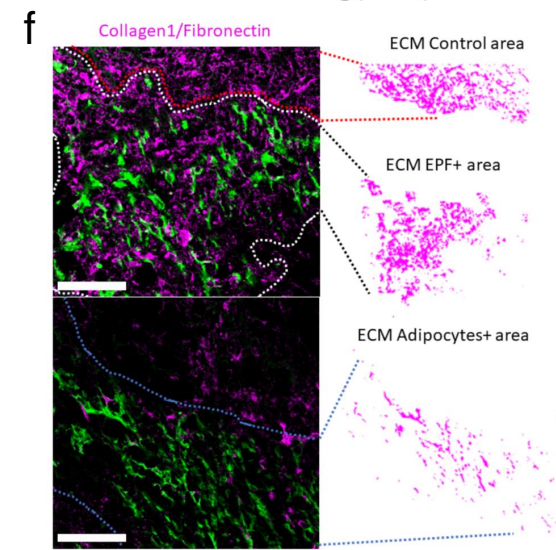
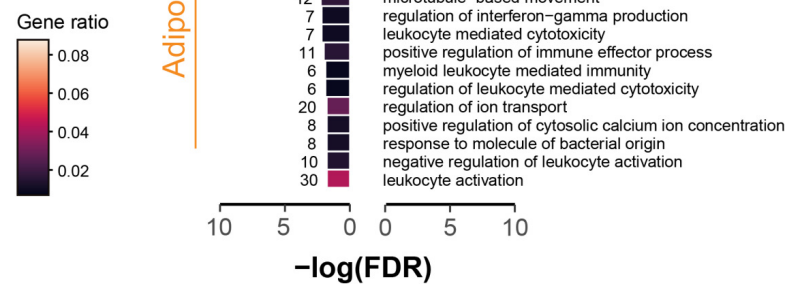
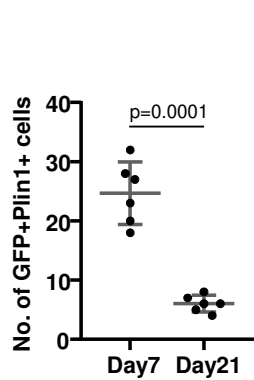
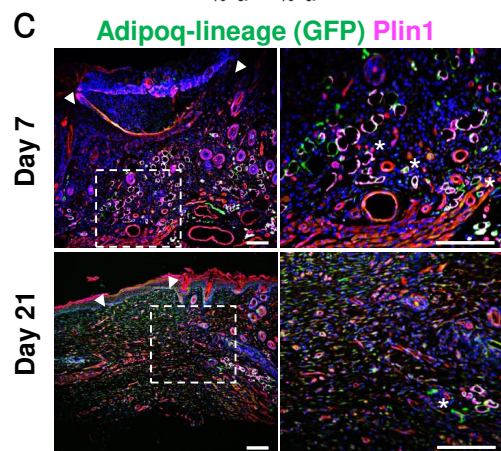
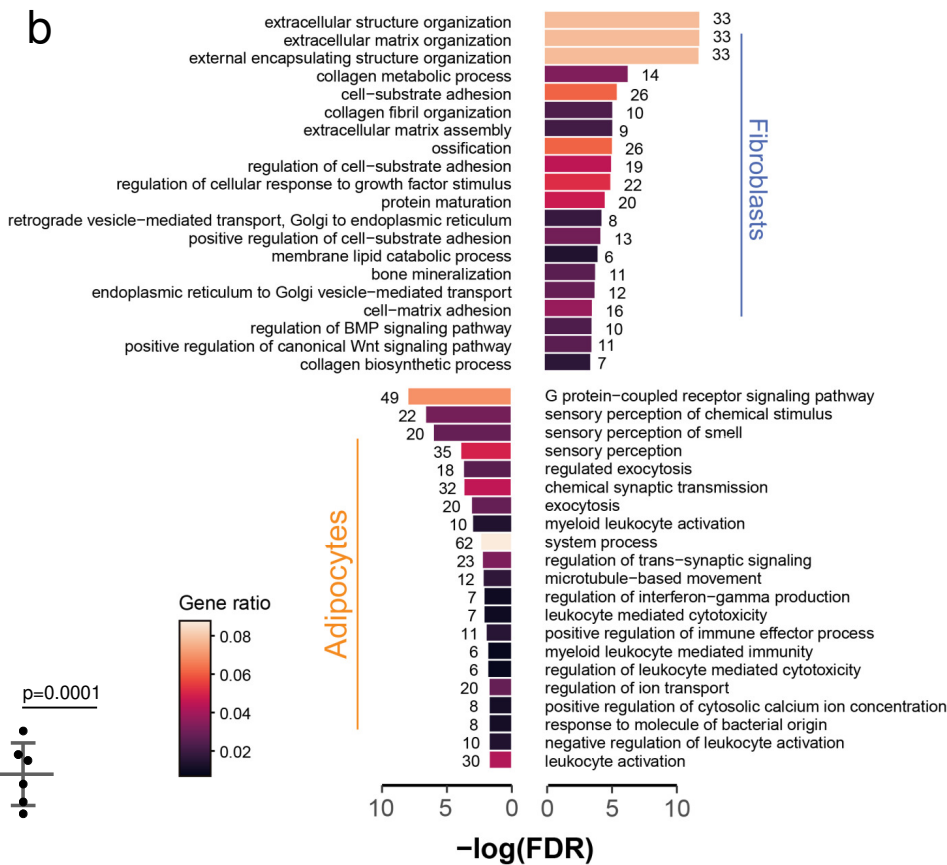
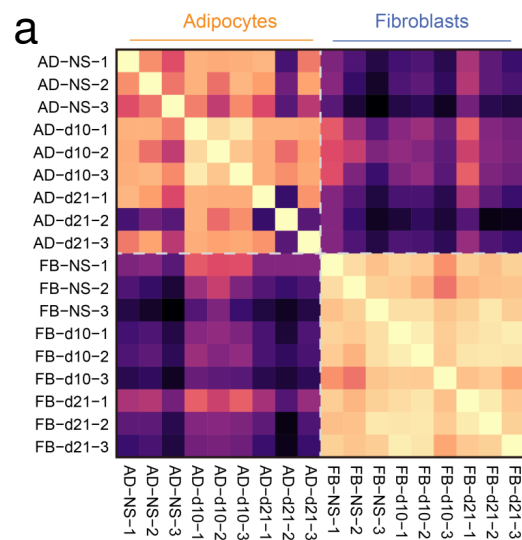
1049 of adipocyte- and fibroblast-associated ECM in the transplanted regions. **n = 3 independent**  
1050 **adipocyte samples, n = 6 independent fibroblast or control samples, mean ± SD, unpaired two-**  
1051 **tailed t-test. h**, Representative images and quantification of cathelicidin-related antimicrobial  
1052 peptide (CRAMP) in GFP positive cells. Data are percentage of CRAMP<sup>+</sup>GFP<sup>+</sup> cells in total  
1053 GFP<sup>+</sup> cells, **n = 6 independent samples**, mean ± SD, unpaired two-tailed t-test. Arrow heads  
1054 indicate the wound borders, the stars indicate the examples of double positive staining. Scale  
1055 bars: **c-f, h = 100 μm**.  
1056













---

## References

1. Chambers, E.S. and M. Vukmanovic-Stejic, *Skin barrier immunity and ageing*. Immunology, 2020. **160**(2): p. 116-125.
2. Gould, J., *Superpowered skin*. Nature, 2018. **563**(7732): p. S84-S85.
3. Bragazzi, N.L., et al., *Fasting and Its Impact on Skin Anatomy, Physiology, and Physiopathology: A Comprehensive Review of the Literature*. Nutrients, 2019. **11**(2).
4. Correa-Gallegos, D. and Y. Rinkevich, *Cutting into wound repair*. FEBS J, 2022. **289**(17): p. 5034-5048.
5. Wong, R., et al., *The dynamic anatomy and patterning of skin*. Exp Dermatol, 2016. **25**(2): p. 92-8.
6. Nguyen, K.D., et al., *Alternatively activated macrophages produce catecholamines to sustain adaptive thermogenesis*. Nature, 2011. **480**(7375): p. 104-8.
7. Boateng, J.S., et al., *Wound healing dressings and drug delivery systems: a review*. J Pharm Sci, 2008. **97**(8): p. 2892-923.
8. Dai, C., S. Shih, and A. Khachemoune, *Skin substitutes for acute and chronic wound healing: an updated review*. J Dermatolog Treat, 2020. **31**(6): p. 639-648.
9. Kimura, S. and T. Tsuji, *Mechanical and Immunological Regulation in Wound Healing and Skin Reconstruction*. Int J Mol Sci, 2021. **22**(11).
10. Godo, S. and H. Shimokawa, *Endothelial Functions*. Arterioscler Thromb Vasc Biol, 2017. **37**(9): p. e108-e114.
11. Berk, B.C., et al., *Vasoconstriction: a new activity for platelet-derived growth factor*. Science, 1986. **232**(4746): p. 87-90.
12. Roe, M.W., et al., *Platelet-derived growth factor and angiotensin II cause increases in cytosolic free calcium by different mechanisms in vascular smooth muscle cells*. J Cell Physiol, 1989. **139**(1): p. 100-8.
13. Pierce, G.F., et al., *Role of platelet-derived growth factor in wound healing*. J Cell Biochem, 1991. **45**(4): p. 319-26.
14. Strecker-McGraw, M.K., T.R. Jones, and D.G. Baer, *Soft tissue wounds and principles of healing*. Emerg Med Clin North Am, 2007. **25**(1): p. 1-22.
15. Teller, P. and T.K. White, *The physiology of wound healing: injury through maturation*. Surg Clin North Am, 2009. **89**(3): p. 599-610.
16. Furie, B. and B.C. Furie, *Mechanisms of thrombus formation*. N Engl J Med, 2008. **359**(9): p. 938-49.
17. Pradhan, S., et al., *The heterotrimeric G protein Gbeta(1) interacts with the catalytic subunit of protein phosphatase 1 and modulates G protein-coupled receptor signaling in platelets*. J Biol Chem, 2017. **292**(32): p. 13133-13142.
18. Pool, J.G., *Normal hemostatic mechanisms: a review*. Am J Med Technol, 1977. **43**(8): p. 776-80.
19. Nguyen, A.V. and A.M. Soulika, *The Dynamics of the Skin's Immune System*. Int J Mol Sci, 2019. **20**(8).
20. Gurtner, G.C., et al., *Wound repair and regeneration*. Nature, 2008. **453**(7193): p. 314-21.
21. Zhu, S., et al., *The emerging roles of neutrophil extracellular traps in wound healing*. Cell Death Dis, 2021. **12**(11): p. 984.
22. Wong, S.L., et al., *Diabetes primes neutrophils to undergo NETosis, which impairs wound healing*. Nat Med, 2015. **21**(7): p. 815-9.
23. Wilgus, T.A., S. Roy, and J.C. McDaniel, *Neutrophils and Wound Repair: Positive Actions and Negative Reactions*. Adv Wound Care (New Rochelle), 2013. **2**(7): p. 379-388.
24. Faurischou, M. and N. Borregaard, *Neutrophil granules and secretory vesicles in inflammation*. Microbes Infect, 2003. **5**(14): p. 1317-27.

- 
25. He, L. and A.G. Marneros, *Macrophages are essential for the early wound healing response and the formation of a fibrovascular scar*. Am J Pathol, 2013. **182**(6): p. 2407-17.
  26. Lucas, T., et al., *Differential roles of macrophages in diverse phases of skin repair*. J Immunol, 2010. **184**(7): p. 3964-77.
  27. Hassanshahi, A., et al., *Macrophage-Mediated Inflammation in Skin Wound Healing*. Cells, 2022. **11**(19).
  28. Martin, P., *Wound healing--aiming for perfect skin regeneration*. Science, 1997. **276**(5309): p. 75-81.
  29. Lau, K., et al., *Exploring the role of stem cells in cutaneous wound healing*. Exp Dermatol, 2009. **18**(11): p. 921-33.
  30. Roh, C. and S. Lyle, *Cutaneous stem cells and wound healing*. Pediatr Res, 2006. **59**(4 Pt 2): p. 100R-3R.
  31. Werner, S. and R. Grose, *Regulation of wound healing by growth factors and cytokines*. Physiol Rev, 2003. **83**(3): p. 835-70.
  32. Bluff, J.E., et al., *Bone marrow-derived endothelial progenitor cells do not contribute significantly to new vessels during incisional wound healing*. Exp Hematol, 2007. **35**(3): p. 500-6.
  33. Sorg, H., C. Krueger, and B. Vollmar, *Intravital insights in skin wound healing using the mouse dorsal skin fold chamber*. J Anat, 2007. **211**(6): p. 810-8.
  34. Talbott, H.E., et al., *Wound healing, fibroblast heterogeneity, and fibrosis*. Cell Stem Cell, 2022. **29**(8): p. 1161-1180.
  35. Lovvorn, H.N., 3rd, et al., *Relative distribution and crosslinking of collagen distinguish fetal from adult sheep wound repair*. J Pediatr Surg, 1999. **34**(1): p. 218-23.
  36. Neville, J.A., et al., *Increase in procedures performed at dermatology office visits from 1995 to 2001*. Dermatol Surg, 2005. **31**(2): p. 160-2.
  37. Frykberg, R.G. and J. Banks, *Challenges in the Treatment of Chronic Wounds*. Adv Wound Care (New Rochelle), 2015. **4**(9): p. 560-582.
  38. Theocharidis, G., et al., *Single cell transcriptomic landscape of diabetic foot ulcers*. Nat Commun, 2022. **13**(1): p. 181.
  39. Grennan, D., *Diabetic Foot Ulcers*. JAMA, 2019. **321**(1): p. 114.
  40. Tessari, P., et al., *Nitric oxide synthesis is reduced in subjects with type 2 diabetes and nephropathy*. Diabetes, 2010. **59**(9): p. 2152-9.
  41. Zhang, Y., et al., *Platelet Microparticles Mediate Glomerular Endothelial Injury in Early Diabetic Nephropathy*. J Am Soc Nephrol, 2018. **29**(11): p. 2671-2695.
  42. Phillipson, M. and P. Kubes, *The Healing Power of Neutrophils*. Trends Immunol, 2019. **40**(7): p. 635-647.
  43. Josefs, T., et al., *Neutrophil extracellular traps promote macrophage inflammation and impair atherosclerosis resolution in diabetic mice*. JCI Insight, 2020. **5**(7).
  44. Wynn, T.A. and K.M. Vannella, *Macrophages in Tissue Repair, Regeneration, and Fibrosis*. Immunity, 2016. **44**(3): p. 450-462.
  45. Boniakowski, A.E., et al., *Macrophage-Mediated Inflammation in Normal and Diabetic Wound Healing*. J Immunol, 2017. **199**(1): p. 17-24.
  46. Krzyszczuk, P., et al., *The Role of Macrophages in Acute and Chronic Wound Healing and Interventions to Promote Pro-wound Healing Phenotypes*. Front Physiol, 2018. **9**: p. 419.
  47. Vannella, K.M. and T.A. Wynn, *Mechanisms of Organ Injury and Repair by Macrophages*. Annu Rev Physiol, 2017. **79**: p. 593-617.
  48. Huang, S.M., et al., *High glucose environment induces M1 macrophage polarization that impairs keratinocyte migration via TNF-alpha: An important mechanism to delay the diabetic wound healing*. J Dermatol Sci, 2019. **96**(3): p. 159-167.
  49. Zhang, X., et al., *NLRP3 Inflammasome Expression and Signaling in Human Diabetic Wounds and in High Glucose Induced Macrophages*. J Diabetes Res, 2017. **2017**: p. 5281358.
  50. Yu, T., et al., *Insulin promotes macrophage phenotype transition through PI3K/Akt and PPAR-gamma signaling during diabetic wound healing*. J Cell Physiol, 2019. **234**(4): p. 4217-4231.

- 
51. Louiselle, A.E., et al., *Macrophage polarization and diabetic wound healing*. Transl Res, 2021. **236**: p. 109-116.
  52. Lerman, O.Z., et al., *Cellular dysfunction in the diabetic fibroblast: impairment in migration, vascular endothelial growth factor production, and response to hypoxia*. Am J Pathol, 2003. **162**(1): p. 303-12.
  53. Desta, T., et al., *Altered fibroblast proliferation and apoptosis in diabetic gingival wounds*. J Dent Res, 2010. **89**(6): p. 609-14.
  54. Wan, R., et al., *Diabetic wound healing: The impact of diabetes on myofibroblast activity and its potential therapeutic treatments*. Wound Repair Regen, 2021. **29**(4): p. 573-581.
  55. Deng, C.C., et al., *Single-cell RNA-seq reveals fibroblast heterogeneity and increased mesenchymal fibroblasts in human fibrotic skin diseases*. Nat Commun, 2021. **12**(1): p. 3709.
  56. Jin, Q., et al., *Macrophages in keloid are potent at promoting the differentiation and function of regulatory T cells*. Exp Cell Res, 2018. **362**(2): p. 472-476.
  57. Hesketh, M., et al., *Macrophage Phenotypes Regulate Scar Formation and Chronic Wound Healing*. Int J Mol Sci, 2017. **18**(7).
  58. Glim, J.E., et al., *Platelet derived growth factor-CC secreted by M2 macrophages induces alpha-smooth muscle actin expression by dermal and gingival fibroblasts*. Immunobiology, 2013. **218**(6): p. 924-9.
  59. van den Broek, L.J., et al., *Suppressed inflammatory gene expression during human hypertrophic scar compared to normotrophic scar formation*. Exp Dermatol, 2015. **24**(8): p. 623-9.
  60. Chen, L., et al., *The clinical dynamic changes of macrophage phenotype and function in different stages of human wound healing and hypertrophic scar formation*. Int Wound J, 2019. **16**(2): p. 360-369.
  61. Zhu, Z., et al., *The natural behavior of mononuclear phagocytes in HTS formation*. Wound Repair Regen, 2016. **24**(1): p. 14-25.
  62. Wynn, T.A., *Fibrotic disease and the T(H)1/T(H)2 paradigm*. Nat Rev Immunol, 2004. **4**(8): p. 583-94.
  63. Trace, A.P., et al., *Keloids and Hypertrophic Scars: A Spectrum of Clinical Challenges*. Am J Clin Dermatol, 2016. **17**(3): p. 201-23.
  64. Hesse, M., et al., *The pathogenesis of schistosomiasis is controlled by cooperating IL-10-producing innate effector and regulatory T cells*. J Immunol, 2004. **172**(5): p. 3157-66.
  65. Chen, Y., et al., *Connection between T regulatory cell enrichment and collagen deposition in keloid*. Exp Cell Res, 2019. **383**(2): p. 111549.
  66. Wang, J., et al., *Increased TGF-beta-producing CD4+ T lymphocytes in postburn patients and their potential interaction with dermal fibroblasts in hypertrophic scarring*. Wound Repair Regen, 2007. **15**(4): p. 530-9.
  67. Chipev, C.C., et al., *Myofibroblast phenotype and apoptosis in keloid and palmar fibroblasts in vitro*. Cell Death Differ, 2000. **7**(2): p. 166-76.
  68. Luo, S., et al., *Abnormal balance between proliferation and apoptotic cell death in fibroblasts derived from keloid lesions*. Plast Reconstr Surg, 2001. **107**(1): p. 87-96.
  69. Tucci-Viegas, V.M., et al., *Keloid explant culture: a model for keloid fibroblasts isolation and cultivation based on the biological differences of its specific regions*. Int Wound J, 2010. **7**(5): p. 339-48.
  70. Yu, D., et al., *Wnt/beta-Catenin Signaling Exacerbates Keloid Cell Proliferation by Regulating Telomerase*. Cell Physiol Biochem, 2016. **39**(5): p. 2001-2013.
  71. Jumper, N., et al., *A Role for Neuregulin-1 in Promoting Keloid Fibroblast Migration via ErbB2-mediated Signaling*. Acta Derm Venereol, 2017. **97**(6): p. 675-684.
  72. Plikus, M.V., et al., *Regeneration of fat cells from myofibroblasts during wound healing*. Science, 2017. **355**(6326): p. 748-752.
  73. Qu, M., et al., *Pathological niche environment transforms dermal stem cells to keloid stem cells: a hypothesis of keloid formation and development*. Med Hypotheses, 2013. **81**(5): p. 807-12.
  74. Correa-Gallegos, D., et al., *Patch repair of deep wounds by mobilized fascia*. Nature, 2019. **576**(7786): p. 287-292.

- 
75. Jiang, D. and Y. Rinkevich, *Furnishing Wound Repair by the Subcutaneous Fascia*. Int J Mol Sci, 2021. **22**(16).
  76. Stecco, C., et al., *The fascia: the forgotten structure*. Ital J Anat Embryol, 2011. **116**(3): p. 127-38.
  77. Spalkit, S., et al., *Dermatomyositis: Patterns of MRI findings in muscles, fascia and skin of pelvis and thigh*. Eur J Radiol, 2021. **141**: p. 109812.
  78. Rinkevich, Y., et al., *Skin fibrosis. Identification and isolation of a dermal lineage with intrinsic fibrogenic potential*. Science, 2015. **348**(6232): p. aaa2151.
  79. Jiang, D., et al., *Two succeeding fibroblastic lineages drive dermal development and the transition from regeneration to scarring*. Nat Cell Biol, 2018. **20**(4): p. 422-431.
  80. Mascharak, S., et al., *Preventing Engrailed-1 activation in fibroblasts yields wound regeneration without scarring*. Science, 2021. **372**(6540).
  81. Kourtidis, A., S.P. Ngok, and P.Z. Anastasiadis, *p120 catenin: an essential regulator of cadherin stability, adhesion-induced signaling, and cancer progression*. Prog Mol Biol Transl Sci, 2013. **116**: p. 409-32.
  82. Jiang, D., et al., *Injury triggers fascia fibroblast collective cell migration to drive scar formation through N-cadherin*. Nat Commun, 2020. **11**(1): p. 5653.
  83. Wan, L., et al., *Connexin43 gap junction drives fascia mobilization and repair of deep skin wounds*. Matrix Biol, 2021. **97**: p. 58-71.
  84. Zhang, Z., et al., *Dermal adipose tissue has high plasticity and undergoes reversible dedifferentiation in mice*. J Clin Invest, 2019. **129**(12): p. 5327-5342.
  85. Schmidt, B.A. and V. Horsley, *Intradermal adipocytes mediate fibroblast recruitment during skin wound healing*. Development, 2013. **140**(7): p. 1517-27.
  86. Spencer, M., et al., *Adipose tissue extracellular matrix and vascular abnormalities in obesity and insulin resistance*. J Clin Endocrinol Metab, 2011. **96**(12): p. E1990-8.
  87. Shook, B.A., et al., *Dermal Adipocyte Lipolysis and Myofibroblast Conversion Are Required for Efficient Skin Repair*. Cell Stem Cell, 2020. **26**(6): p. 880-895 e6.

---

## Acknowledgements

This thesis would not have been possible without the support of many people, to whom I would like to express my gratefulness.

I would first like to appreciate my mentor and the director of Institute of Regenerative Biology and Medicine (IRBM), Dr. Yuval Rinkevich, for his guidance throughout my Ph.D. career. His dedication and enthusiasm for research have inspired my confidence in my project, and he has also worked diligently to guide me in my experimental approach and critical thinking, providing me with more ideas and possibilities for the project. I would also like to thank my supervisor, the director of the Department of Medicine V, Prof. Dr. Jürgen Behr for his constructive advice at different stages of the project which was highly rewarding. Further, I would like to thank my external expert Prof. Dr. rer. nat. Markus Rehberg, group leader of the Institute of Lung Health and Immunity (LHI), for his help in research methodology and guidance on my project.

Many appreciations to Dr. rer. nat. Florian Wirsdörfer, head of the junior research group 'Immuno-modulation', for providing us with the precious CD39-KO mice, which were of enormous help in the further proving of my project. I would also like to thank the animal carer takers of Unit 34, especially Boris Schön and Marco Hendrich, for assisting me in transporting and managing the mice.

I would like to express my sincere gratitude to the teachers and professors of HELENA, the Comprehensive Pneumology Center (CPC) research school, and the affiliated institutions of the Helmholtz Zentrum München. Meanwhile, I would also like to give my sincere thanks to China Scholarship Council (CSC) for funding my Ph.D. career and provide me an opportunity being able to fulfill my dream of research.

My gratefulness to Dr. Dongsheng Jiang for his thorough guidance and huge help in the project. His profound insight into the field of skin wound repair has helped me to further develop my work. His expertise, knowledge, and willingness to help have been invaluable to me throughout the entire process. I would like to thank Yue Lin for her continuous help during the experimental period. She was one of the best partners I had during my Ph.D. Her help has enabled me to achieve many results in my research.

I thank to the entire past and present members of Rinkevich lab for their professional support, Jiakuan Zhao, Dr. Donovan Correa-Gallegos, Haifeng Ye, Ruiji Guo, Xiangyu Zhang, Wei Han, Shaoping Hu, Aydan Sardogan, Andy Qarri, Dr. Young Hwa Kim, Dr. Mahesh Gouda, Dr. Tankut Guney, Dr. Adrian Fisher, Dr. Martin Mück Häusl, Dr. Shruthi Kalgudde Gopal, Dr. Safouane Kadri, Dr. Pushkar Ramesh, Dr. Vijayanand Rajendran, Dr. Ryo Ichijo, Dr. Ravinder Kandi, Jiazheng Lai, George Vogelaar, Christoph Deisenhofer, Bikram Dasgupta, thank you all for your help and support over the years. Special thanks to Natalja S. Ring, the lab manager, whose care beyond the lab was very gracious to me.

Lastly, I would like to give my most heartfelt and overwhelming thanks to my parents and my husband, you brightened me up when I hit rock bottom and gave me strength in every anxiety and depression. You are my strongest support, allowing me to take every step forward without fear of danger. You are the ones who have shaped me and made me more confident to accomplish the different stages of my life.

I dedicate my thesis to them.